Numerical Studies of Star and Disk Formation

by

Aleksandra Kuznetsova

A dissertation submitted in partial fulfillment
of the requirements for the degree of
Doctor of Philosophy
(Astronomy and Astrophysics)
in The University of Michigan
2020

Doctoral Committee:

Professor Lee William Hartmann, Chair
Professor Fred C. Adams
Professor Nuria Pilar Calvet
Associate Professor Fabian Heitsch, University of North Carolina - Chapel Hill
Professor Michael Meyer

Aleksandra Kuznetsova

kuza@umich.edu

ORCID iD: 0000-0002-6946-6787

© Aleksandra Kuznetsova 2020

For my friends — who have also been my teachers.

ACKNOWLEDGEMENTS

So long and thanks for all the fish.

– Douglas Adams, ”The Hitchhiker’s Guide to the Galaxy”

This dissertation would not have been possible without many factors, too many to list exhaustively and accurately, in fact. I will attempt an incomplete list here, but the general gist is that absolutely nothing even halfway good can be done in isolation, no (wo)man is an island, etc. The truth of the matter is that I have benefited enormously from the guidance, support, advice, and general kindness of those around me and thus I am very lucky to have so many people that need to be thanked.

I’d like to thank my advisor, Lee Hartmann, for his scientific guidance and for giving me the opportunities to really make something that I can be incredibly proud of. Lee possesses an incredible ability to look at data and ferret out what thing to ask of it in an elegant no nonsense sort of way; I’ve been fortunate to be taught to ask scientific questions so shrewdly. Most of all, I’m thankful that Lee took me seriously from the start, respected my knowledge, and pushed me with the verve of someone who expected a lot from me. I spent a lot of time being incredibly unsure of myself and occasionally being quite obtuse, so I’m thankful that there was someone there to ignore it for the nonsense it was.

This work has been molded and supported by the efforts of my co-authors and my thesis committee: Javier Ballesteros-Paredes, Fabian Heitsch, Andreas Burkert, Manuel Zamora-Aviles, Shangjia Zhang, Michael Meyer, Nuria Calvet, and Fred Adams. It wouldn’t have been the same without their contributions and support.

I am, of course, indebted to all the talented people who have worked in stars and planets in this department. It is really quite extraordinary to get to spend an hour a week talking about star and planet formation and in turn learning how brilliant my colleagues are.

I'd like to thank everyone who has taken the time to offer informal mentorship, even if it's just in the lounge while getting espresso [1]. A big thanks to Emily Rauscher and Keren Sharon for taking their time to pull graduate students out of a funk and just being real with us when we need it. Thank you to postdocs whose time here is short (but impactful), its wonderful to be part of a scientific community that ensures I get to bump into them again. Thanks especially to Richard Teague for making space for me and many others.

The graduate students here know how important community is and their relentless support has truly shaped my experience. Getting a PhD is one of the hardest things that I've ever done, and graduate school is just plain difficult. The fact that the grad students here are so clever, hard working, and kind in the face of fairly arduous challenges speaks to their grace and generosity of spirit. And again, I'm simply so very lucky to call many of them my friends. Thanks to Adi for putting up with me as deskmate and officemate for so long, you are amazing and luminous and I will miss getting to bask in your radiance. Thanks to Kevin, Larissa, and Nic for letting me join your gang, it will be heart achingly lonely without you nearby next year. Thanks to Renee and Erin for being unnervingly inspiring badasses, I feel that never again will I meet such intense people. And thanks to the OG Ladies of Aquila, especially to Kamber who looks out for me when I need it most.

It's easy to get tunnel vision when doing science, so I'm thankful for all the ways my life has been enriched outside of it. Thanks to my cohort and teachers in the Museum Studies Program for their wisdom, the chance to stretch my brain in new ways, and the ability to see the world as a little bigger and a little more lovely. Thanks to my family for cheering me on from afar. Thanks especially to my sibling, Lola, for reminding me of the value of bringing a little beauty and

---

[1] and for the free espresso that makes it possible!

kindness into the world. I'm a better person for it.

And finally, Jim Shanahan, who has been there since the start, who patiently watched me say "10 more minutes" on problem sets every 3 hours, who lets me groan dramatically while he makes me a cup of tea, who looked at me like I was crazy when I said I didn't think I was smart enough to do physics, who has rearranged plans to make things work — I hope he already knows how important he is and how grateful I am.

TABLE OF CONTENTS

CHAPTER

LIST OF FIGURES

Figure

LIST OF TABLES

Table

LIST OF APPENDICES

Appendix

ABSTRACT

Protoplanetary disks are ubiquitous and play a significant role in the early stages of star and planet formation; stars grow their mass from disks and conditions within the disk determine available routes for planet formation. A testable theory of star and planet formation requires predictions of the range and relative distribution of disk properties. The goals of this thesis are to identify and understand the dominant physical processes that dictate star cluster and protostellar disk properties and behavior using a series of numerical experiments. I motivated the rapid assembly of star forming material by demonstrating the growth of the star cluster initial mass function through gravitational focusing (Chapter 2). Testing a sub-virial (cold) collapse model of star cluster formation, I showed that many large scale morphological and kinematic features of known nearby clusters can be reproduced (Chapter 3). Furthermore, I investigated the presence of kinematic substructure in clusters formed by cold collapse and found that stellar groups are likely to preserve evidence of early mass segregation through velocity coherent substructures seen in observed radial velocities (Chapter 4). Adding a sink-patch numerical construction to track the environs of star forming particles in the simulation, I modeled the formation of protostellar cores from the progenitor molecular cloud. In Chapter 5, I used the sink-patch construction to demonstrate the importance of the star formation environment when determining protostellar accretion rates and modeling the growth of the upper mass power law of the stellar initial mass function. In addition, I characterized how protostellar cores accrete angular momentum without (Chapter 6) and with (Chapter 7) the presence of magnetic fields. Together, this work has led to a statistical characterization of protostellar core properties and their accretion behaviors and set the stage for modeling disk formation with a set of physically motivated initial conditions that take into account the star forming environment.

CHAPTER 1

Introduction

The study of star formation bridges the conditions of the Galactic interstellar medium (ISM) with the origins of stellar and planetary systems, like our own Solar System. As such, it spans an immense range of physical scales; molecular clouds, the birth sites of stars, are 4-5 orders of magnitude larger than most planetary systems and nearly 8 orders of magnitude larger than the size of a Sun-like star. Numerical simulations have emerged as a powerful tool for testing star formation theory, allowing us to speculate as to what observations have yet to reveal. Understanding the conditions that lead to the origins of planetary systems requires a complete model of star formation starting with the physics of Galactic stars and gas down to synthesizing the statistics of exoplanetary systems. However, we do not have the computational resources for this venture in one single simulation nor should we bend to the inclination to reproduce the Universe on CPU [1].

In this body of work, I motivate and present a model of star formation that seeks to connect the dynamics of the star forming environment to the eventual attributes of (proto) planetary systems. I use a number of computational techniques, with both particle and grid based methods, in order to stage numerical experiments. These experiments do not include every possible physical process, but instead focus on identifying the most relevant physics for each problem and testing the results against selected observational diagnostics. This work aims to inform models of disk formation and evolution by making predictions as to the range and distribution of initial conditions for protostellar

---

[1] Lest we fall victim to some sort of *Simulation of Babel* situation in the manner of Borges (1998) *Library of Babel*

and protoplanetary systems and shed light on a physically motivated and self-consistent picture of star and disk formation.

1.1 Star Formation Conditions in the Interstellar Medium

Stars make up the bulk of luminous matter in our galaxy, followed by interstellar gas and dust. Stars feed radiative, thermal, and kinetic energy back into the interstellar medium through protostellar jets, stellar winds, and eventually supernovae. Thus, the gas in this interstellar medium exists at many densities and temperatures — the phases regulated by physical processes that heat, cool, and collect material. Additional contributions to gas dynamics come from the large scale magnetic field that threads the Galaxy, which can assist in accumulating and confining gaseous material and aid in the diffusion of cosmic rays. Giant molecular clouds (GMCs) are thought to contain the progenitor material out of which most stars in our Galaxy form; a census of the nearest 2 kpc reveals well over a 100 star clusters still embedded in dusty molecular material (Lada & Lada, 2003).

Observations of molecular clouds and star forming regions at various ages have shaped our current sketch of the star formation process (Figure 1.1). A multi-scale process, star cluster formation depends on the conditions of the progenitor cloud material. The physics of the star forming environment determines the properties of protostellar and stellar systems like the distribution of masses, angular momenta, and magnetization of protostellar cores. These fundamental quantities influence the sizes, orientations, and structures of protoplanetary disks — setting the environments and reservoirs for subsequent planet formation.

1.1.1 Pressure Conditions

Star formation requires achieving high enough densities such that the self gravity of the gas becomes dominant over other forms of pressure support in the interstellar medium. Jeans's original analysis determined the limits of stability of a spherical cloud in an infinite static medium (Jeans, 1902), where the Jeans length, r_J, for a given density, ρ, and temperature, T, gas is the maximum

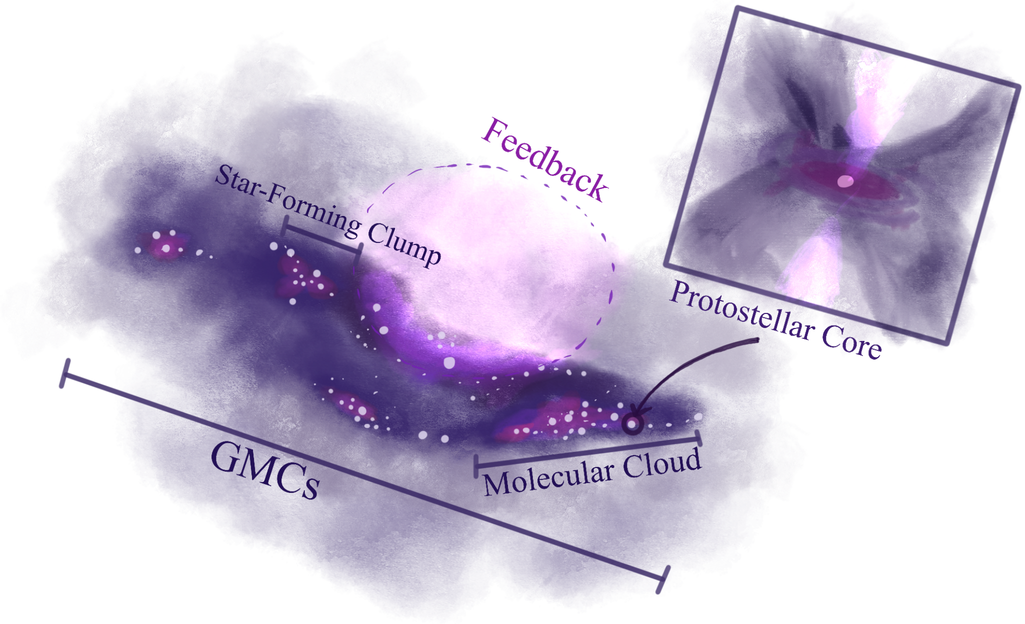

Figure 1.1: A schematic of star cluster formation from the molecular cloud. Molecular clouds are host to star-forming clumps and their constituent protostellar cores, from which protostellar and protoplanetary disks evolve into stellar and planetary systems. As massive stars form, gas is removed from the system, likely by feedback processes such as outflows. Major gas dispersal will allow some stars to become unbound and enter the field while remaining bound stars will constitute an open cluster.

size of a cloud stable against gravitational collapse [2].

$$r_J = c_s(4\pi/3G\rho)^{-1/2} \propto T^{1/2}\rho^{-1/2} \tag{1.1}$$

The corresponding Jeans mass assuming a uniform density cloud is then:

$$M_J = \frac{4\pi}{3}\rho r_J^3 \propto T^{3/2}\rho^{-1/2} \tag{1.2}$$

Pressure conditions across the ISM vary and thermal pressure is not the only source of support against self-gravity. For cold gas with temperatures $T \sim 10$ K and number densities $n \sim 10 - 10^3$ cm^{-3}, thermal pressure will contribute $P_{therm}/k \sim 10^2 - 10^4$ cm^{-3} K . In the ideal magnetohydrodynamic (MHD) limit, magnetic field lines are frozen into the gas, with flow allowed

---

[2] A corollary to this statement is that all scales larger than the Jeans length are unstable to collapse, such that the Jeans mass is the *minimum* mass of an object that forms from an unstable Jeans sized cloud.

along field lines at lower densities and increased magnetic field strength as material is compressed to higher densities. Measurements of magnetic fields in molecular cloud cores have found that magnetic fields strengths can be in the range between $5 - 10^4$ μG, consistent with the density scaling in the ideal MHD flux-freezing limit $B \propto \rho^{2/3}$ (Crutcher, 2012). If we consider the main pressure sources relevant for molecular clouds to be thermal and magnetic [3] , then the total pressure in the ISM as a function of number density, n, and temperature, P_{ISM}, can be represented by the following [4]:

$$P_{ISM} = P_{therm} + P_{mag} \tag{1.3a}$$

$$P_{therm}/k = nT = 10^3 \text{ cm}^{-3} \text{ K } n_{100} \, T_{10} \tag{1.3b}$$

$$P_{mag}/k = B^2/8\pi k = \begin{cases} 7200 \text{ cm}^{-3} \text{ K} & n \leq 300 \text{ cm}^{-3} \\ 7200 \text{ cm}^{-3} \text{ K } {n_{300}}^{2/3} & n > 300 \text{ cm}^{-3} \end{cases} \tag{1.3c}$$

Assuming hydrostatic equilibrium (HSEQ), the pressure due to self gravity, P_{grav}, of a slab of uniform density gas can be written in terms of its surface density Σ (Elmegreen & Elmegreen, 1978):

$$P_{grav} = \pi G \Sigma^2/2 \tag{1.4}$$

Computing the ratio of P_{grav} to P_{ISM}, Figure 1.2 illustrates where in the density - size space of clouds that gravity can dominate over typical ISM pressures calculated from Equation 1.3, the transition between the two regions shown as a bold black line. Molecular clouds, as sample points computed from observational results in Heyer et al. (2009), lie squarely in the self-gravity regime. Typical pre- and proto- stellar material forms near the boundary of this regime, its internal structure and evolution depends on the relative importance of gravitational infall and other sources of energy.

---

[3] cosmic rays, while a source of pressure in the ISM, don't diffuse uniformly in different phases and are not thought to alter this picture significantly (see: Grenier et al., 2015)

[4] For this chapter, I adopt a convention for pressure in units of cm^{-3} K, an energy density divided by k, the Boltzmann constant.

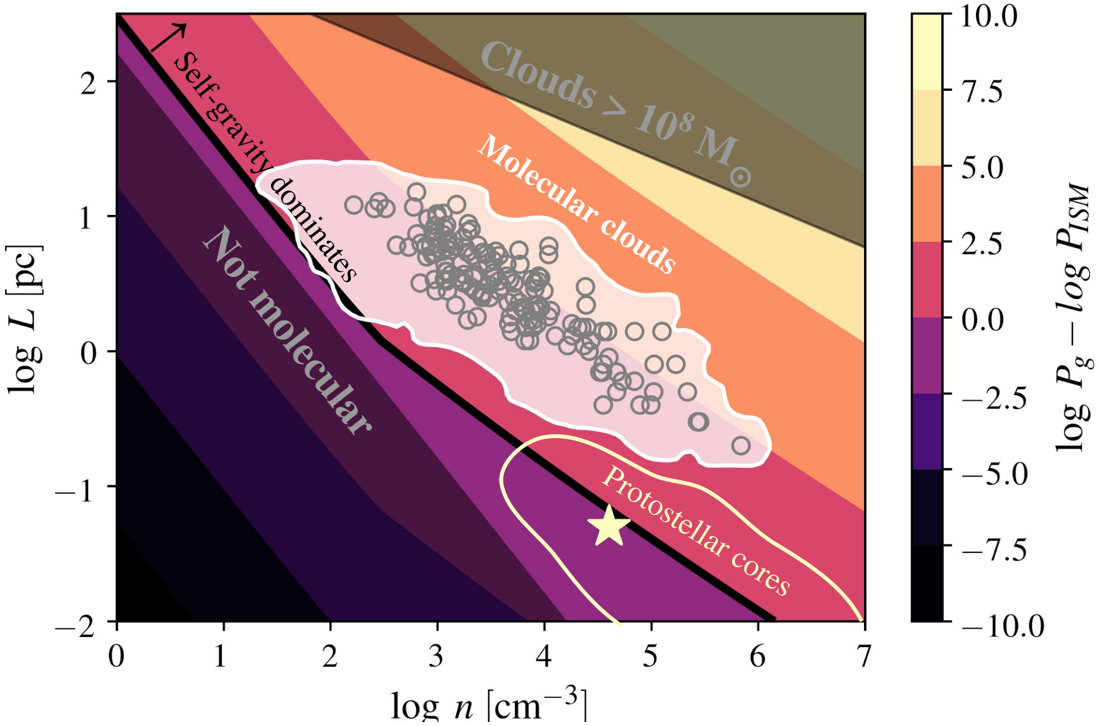

Figure 1.2: The magnitude of pressure difference between gravity and ISM pressures, log P_{grav} − log P_{ISM} as a function of number density, n, and length scale L. The bold black line demarcates the transition region in $n-L$ space from a thermal/magnetic pressure regime into one in which we can expect the self gravity of molecular gas to become important. Measurements of molecular cloud surface densities and sizes from (Heyer et al., 2009) plotted as open circles, with possible errors due to assumptions in geometry and distance uncertainties as the shaded white contour, lie firmly in the self gravity dominated zone. The canonical Bonner-Ebert like protostellar core ($M = 1$ M$_\odot$, $R = 0.05$ pc) is plotted as a star symbol in the protostellar core region, corresponding to typical masses and sizes of protostellar material. Shaded regions indicate regions of $n-L$ space unlikely to host Galactic cloud material — lower left corner corresponds to regions which do not have the necessary surface density for molecular self-shielding (see: Hartmann et al., 2001) and upper right corner would require molecular cloud masses much larger than the largest known GMCs.

Molecular clouds and star forming regions are as a rule highly structured and filamentary (e.g. Blitz, 1993). The pressure calculations for Figure 1.2 make a number of simplifying assumptions regarding cloud density and geometry but can still be used for understanding the average properties and conditions within molecular clouds. It is important to note that for self-gravitating structures, Figure 1.2 is not a static picture. We can readily expect that the molecular clouds shown are not a

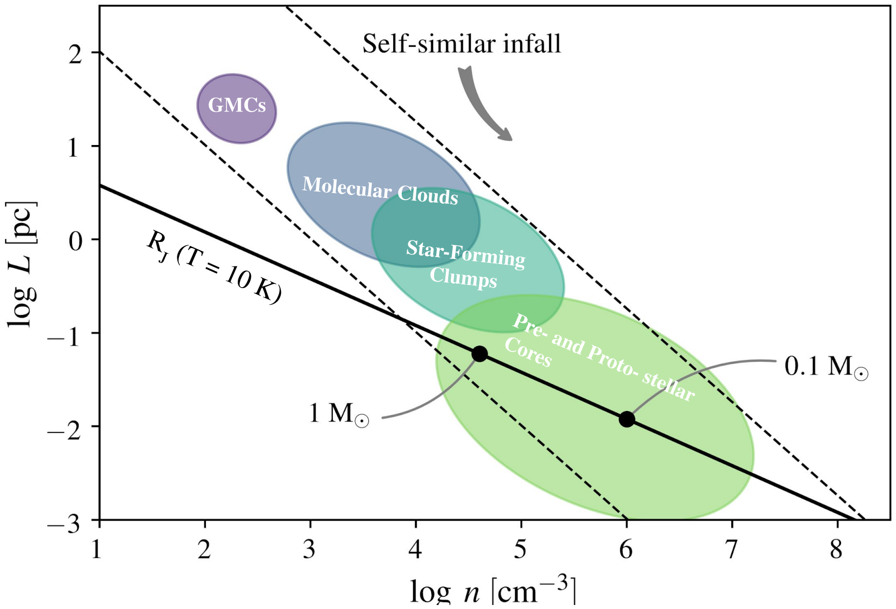

Figure 1.3: Regions where observed dense structures lie in $n - L$ space (based on Table 1 in: Mac Low & Klessen, 2004) from GMC cloud complexes down to pre- and proto- stellar material, a hierarchy in scale and density. Lines of self-similar isothermal collapse are shown as dashed lines, where the Jeans length for each density at a temperature of $T = 10$ K is the solid black line. Points corresponding to minimum Jeans masses of $M_J = 0.1$ M$_\odot$ and 1 M$_\odot$ are annotated.

single population formed at the same time, but may instead be representative of dense structures formed at different scales at various points of dynamical evolution. If we consider the case of a self-similar isothermal collapse, the density of infalling envelope material will vary with scale as $\rho_{in} \propto r^{-3/2}$ (Shu, 1977), such that lines of infall will have a slope of $-2/3$ in $n - L$ space. The Jeans length line for the stability of a spherical cloud will have a slope of $-1/2$ in $n - L$ space, such that its intersection with the lines of constant infall co-located in $n - L$ space with observed protostellar core material (Figure 1.3).

1.1.2 The Dynamics of Molecular Clouds

Based on the pressure balance above, molecular clouds are likely to be gravitationally infalling at multiple scales and densities. The dynamics of molecular clouds are commonly probed by calculating the velocity dispersion, δv, from a combination of measurements — the radial velocity gradient and the linewidth of ^{13}CO and other molecular species across the cloud. Early analyses of molecular cloud kinematics (Goldreich & Kwan, 1974) proposed that the observed supersonic molecular cloud motions were a product of gravitational collapse. However, when Larson (1981) identified a velocity-size relation for molecular clouds $\delta v \propto R^{\beta}$ for $\beta = 0.38$, the scaling was attributed to small scale turbulence due to its similarity to the $v \propto R^{1/3}$ relation expected from incompressible turbulence (Kolmogorov, 1941).

Larson (1981) also identified a density - size relationship, $\rho \propto R^{\alpha}$ where $\alpha = -1.1$, suggesting that all molecular clouds have the same surface density. For self-gravitating material, the time for a pressureless collapse with infall velocity $v_{in} = \sqrt{GM/R}$ is the free-fall time, $t_{ff} = R/v_{in} \propto 1/\sqrt{G\rho}$. If all molecular clouds have the same surface density, then the free-fall time will have a very weak scaling with mass, $t_{ff} \propto M^{1/4}$. Based on the GMCs in the Larson (1981) sample, with $M \sim 10^{6}$ $\mathrm{M}_{\odot}$, $R \sim 50$ pc, the typical free-fall time $t_{ff} \sim 2.5$ Myr of all molecular material in the galaxy $M_{mol} \sim 10^{8} - 10^{9}$ $\mathrm{M}_{\odot}$ would yield galactic star formation rates on the order of $40 - 400$ $\mathrm{M}_{\odot}$ yr^{-1}, rather than the observed 4 $\mathrm{M}_{\odot}$ yr^{-1} (Zuckerman & Evans, 1974). The turbulence interpretation of the velocity-size relation implies that turbulence could provide an additional form of pressure support in molecular clouds in order to resolve the assumed discrepancy.

Later studies of samples at higher sensitivity adjusted the value of the exponent of the velocity-size relation to the widely accepted $\beta = 1/2$ (Solomon et al., 1987), prompting the search for other origins of the velocity-size scaling [5]. On the order of several km s^{-1}, the velocity dispersions in molecular clouds are highly supersonic, likely contributing to MHD shocks in the ISM; this revised mechanism conveniently corresponds to a turbulent scaling for velocity $v \propto R^{1/2}$ (Elmegreen & Scalo, 2004; McKee & Ostriker, 2007, and references therein). Magnetic field measurements from OH masers in molecular clouds yielded similar relations but with an additional dependence on magnetic field strength $\delta v \propto R^{1/2}B^{1/2}$(Mouschovias & Psaltis, 1995).

However, a survey of the regions from Solomon et al. (1987) with different tracers and a larger range of column densities by Heyer et al. (2009), found that velocity dispersion is not only depen-

---

[5] Astronomers, in their hubris, love power laws so I mention only a few scaling predictions here.

dent on size, but also surface density:

$$\delta v \propto \Sigma^{1/2} R^{1/2} \tag{1.5}$$

An explicit dependence on Σ (see also: Ballesteros-Paredes et al., 2011, for a meta-analysis), naturally explains the indirect correlation between velocity, size, and magnetic field strength from Mouschovias & Psaltis (1995) as consequence of flux-freezing and suggests a balance between the kinetic energy in fluctuations $E_K \propto M\delta v^2$ and the gravitational energy $E_{grav} \propto GM^2/R$. While this scaling is consistent with virial equilibrium $2E_K + E_{grav} = 0$ (Heyer et al., 2009), clouds in free-fall $E_K + E_{grav} = 0$ would also have the same scaling relation but offset by a factor of $\sqrt{2}$, within the errors of the original measurement (Ballesteros-Paredes et al., 2011). In fact, the normalization of the relation will always be uncertain, as the coefficient for $E_{grav} = 3/5GM^2/R$ depends on the problematic assumption of a uniform density sphere.

On its own, the relation in Equation 1.5 does not establish the dynamical state of molecular clouds and is only a statement that molecular clouds have supersonic motions that scale with their gravitational potential.

1.2 Evolution of Dense Structures

The two primary interpretations of Equation 1.5 have significant consequences on the assumed physical conditions for star formation. If molecular clouds are in virial equilibrium, then they are long-lived objects that require a source of kinetic energy to support against large scale collapse and create supersonic motions that scale appropriately. Various forms of turbulence are invoked to generate this source of support. Global turbulent support means that most collapse will occur locally on small scales, with turbulence regulating the speed and type of star formation that can occur (see: McKee & Tan, 2003; McKee & Ostriker, 2007, and references therein).

If the supersonic motions are a diagnostic of large scale free-fall, then molecular clouds are transient and star formation proceeds rapidly, driven by gravitational flows and eventually regulated by the depletion of the gas reservoir, likely through both competitive accretion and feedback from newly formed stars (e.g. Bonnell & Bate, 2006; Heitsch & Hartmann, 2008; Vázquez-Semadeni et al., 2019). In §1.2.1-1.2.2, we discuss some of the issues surrounding assumptions of turbulent regulation and introduce an interpretative framework based on gravity-driven dynamics during star formation.

1.2.1 The Role of Turbulence?

Turbulent scaling relations arise from a model that states that kinetic energy injected at some initial scale, $k_L = 2\pi/L$, cascades down to smaller scales at with a constant flux, ε, until it reaches scales small enough, $k_\nu = 2\pi/\ell_\nu$, that viscous forces dissipate that energy thermally [6]. In this formulation, kinetic energy drives turbulent eddies that interact at some rate ω_{int} to transfer energy with constant energy flux:

$$\varepsilon = v_k^4 k^2 / \omega_{int} = \text{constant} \tag{1.6}$$

The energy per unit mass per wavenumber is distributed to scales as a power law of the form $E(k) \propto k^{-n}$, such that $\int E(k)dk = v^2$ and thus, $E(k) \propto v_k^2/k$.

The scaling for velocities and the exponent for the energy spectrum can be derived from dimensional analysis or heuristic arguments; here we frame our discussion in terms of the form of the eddy interaction rate, a function of the physical mechanism proposed to drive the turbulence (Elmegreen & Scalo, 2004). For the classic model of hydrodynamic incompressible turbulence (Kolmogorov, 1941), interactions are assumed to be isotropic and scale invariant $\omega_{int} = kv$ such that $v \propto k^{-1/3}$ and $E(k) \propto k^{-5/3}$. In MHD turbulence, eddies are influenced by the magnetic fields so that we can expect the rate of interactions might depend not on the eddy velocities, but on the rate of their propagation in a magnetic medium, the Alfvén velocity, $v_A = B/\sqrt{4\pi\rho}$. In the presence of strong magnetic fields and relatively weak turbulence, eddies are likely to move along

---

[6] or in the words of luminary and space poet, David Bowie, in *Changes*: " ... the ripples change their size but never leave the stream of warm impermanence"

field lines, their interactions no longer isotropic, but favoring modes parallel to the field at the scale of the field $k_{\|} =$ constant yielding a constant ω_{int} such that $v \propto k^{-1/2}$ and $E(k) \propto k^{-2}$ (Ng & Bhattacharjee, 1997), matching the scaling of the adjusted Larson law.

The biggest question surrounding turbulence in the ISM is not whether or not it exists — the ISM is highly structured and numerical simulations have shown that turbulence can readily create density inhomogeneities (Mac Low & Klessen, 2004). In fact, large scale colliding flows of atomic gas are capable of both forming dense molecular material and injecting turbulent energy resulting in self-gravitating dense structured clouds (Heitsch et al., 2006). What remains unclear is if there exists a physical mechanism or mechanisms of turbulent energy injection that generates support against the self-gravity of molecular clouds. Supersonic motions due to gravitational infall could even lead to the development of gravitational turbulence, but its not clear that these motions would necessarily hinder star formation rather than further aid in the concentration of dense material (Ballesteros-Paredes et al., 2011).

Without constant energy injection, supersonic turbulence will decay faster than the free-fall time for the cloud as shocks dissipate kinetic energy (Stone et al., 1998; Mac Low, 1999). Thus, additional continued driving is necessary if turbulence is meant to support molecular clouds against large scale collapse. The exact nature of turbulent pressure support is unclear. We can estimate it as a kinetic energy density $P_{turb} = \rho v^2$, where $v \propto R^{1/2}$, so as to attempt to determine under what conditions assumed turbulent support can create stability in molecular clouds. Figure 1.4 shows that in order to shift the boundary for self-gravity past the region in which molecular clouds reside in Figure 1.2, turbulence would have to be driven continuously on all scales within the cloud, requiring a considerable amount of constant energy input.

Supernovae and stellar winds drive flows that inject energy and momentum into the ISM, where supernovae are thought to be the dominant contributors (Elmegreen & Scalo, 2004; Mac Low & Klessen, 2004; Walch & Naab, 2015). However, there is no definitive evidence that these sources alone can produce the amount and scale of driving necessary to keep molecular clouds in virial equilibrium. Recent numerical studies have found that supernovae likely aid in the collection of

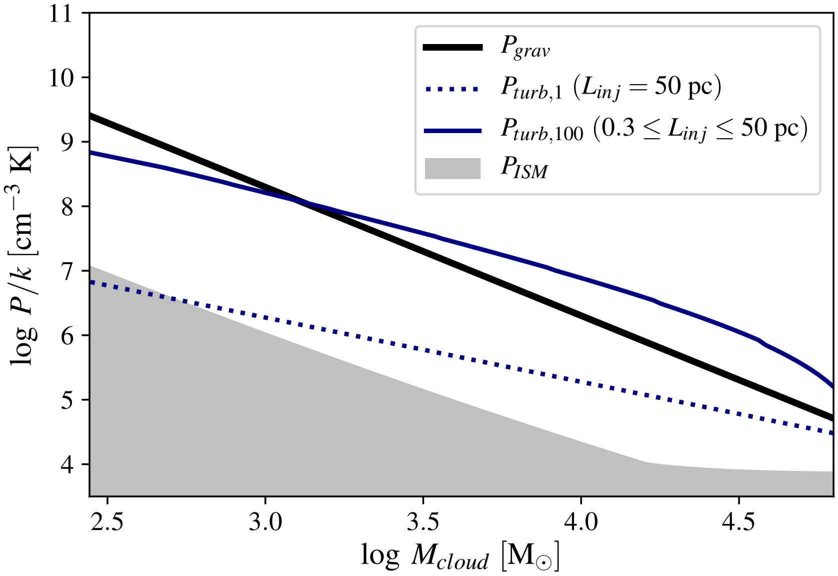

Figure 1.4: Pressures and masses from a slice of $n-L$ space in Figure 1.2, sampled along the line of best fit to the Heyer et al. (2009) data. Energy injection $E(k) \propto k^{-2}dk$ at one scale $L_{inj} = 50$ pc (dotted line) is not enough to overcome self-gravity for the sampled $n-L$ points. It takes 100 injected cascades at scales between $0.3-50$ pc to produce the curve for $P_{turb,100}$ (bold navy line).

dense star forming material by driving colliding flows, but at their current rates they are unable to drive turbulence for the timescales necessary to stave off large scale gravitational infall (Seifried et al., 2018). Internal to star forming regions, supernovae, stellar winds, and protostellar jets are more likely to disrupt clouds and halt further star formation rather than generate support to extend star formation timescales (Seifried et al., 2018; Dale et al., 2012; Banerjee et al., 2007).

1.2.2 Gravitational Focusing

Without additional interpretation of the origin of supersonic cloud motions, it is important to note that both gravity and turbulence are multi-scale processes. Traditional stability analyses with and without magnetic fields (Jeans, 1902; Mestel & Spitzer Jr, 1956) assume uniform density distributions, quasi-equilibrium conditions, and predict limits on the scales of stability. These can inform us about the average conditions for star formation, but can not capture non-linear or multi-scale behavior. With numerical simulations, it has become possible to investigate the effects of physical processes across a larger dynamic range and conceptualize star formation as an inherently hierarchical process (Vázquez-Semadeni et al., 2019).

Given the structured nature of the ISM, gravity is likely to act hierarchically in terms of both scale and density. Higher mass density regions will have shorter free-fall times, larger infall velocities, and their potential can act over longer distances. Bondi-Hoyle-Lyttleton (BHL) accretion describes the solution for flow onto a mass, M, where within the radius, $R_{BHL} = GM/v^2$, the flow is supersonic and infalling onto the mass. The rate of accretion for a mass in medium of density ρ_0 with sound speed $c_{s,0}$ traveling at a relative speed v_0 is:

$$\frac{dM_{BHL}}{dt} = \frac{4\pi G^2 M^2 \rho_0}{(c_{s,0}^2 + v_0^2)^{3/2}} \tag{1.7}$$

(see review in: Edgar, 2004).

As such, density heterogeneity of ISM structures can lead to gravitational focusing: a non-linear relationship between the mass of an object and the rate at which it can accrue more mass like $\dot{M} = \alpha M^2$, where α parameterizes the effect of the environment. The asymptotic limit of this behavior on a random set of initial masses is a power law distribution of the form $dN/dM = M^{-2}$ (Zinnecker, 1982). During star cluster formation, given a finite accretion reservoir, it can also lead to a competitive accretion scenario in which higher mass objects deplete local gas reservoirs, limiting the masses of other objects and locally throttling star formation (e.g. Bonnell & Bate, 2006).

1.2.3 Embedded Clusters as Astrophysical Laboratories

The questions of how dense structures are seeded, how they evolve and how their distributions and properties map onto observed stellar distributions are a vital component of star formation theory. Young embedded clusters, regions with a high density of protostars and stars found within their progenitor cloud, offer a unique opportunity to probe multi-scale processes and draw parallels between the physical conditions of star-forming gas and the nascent stellar populations within.

On large scales, filamentary structure and magnetic fields appear to be correlated (Planck Collaboration et al., 2016), where magnetic field plane-of-sky orientations are found to be perpendicular to most dense filaments and parallel to lower density striations. This suggests that magnetic fields may play a role in seeding structure at large scales, where flow along field lines leads to the accumulation of material in sheets and filamentary streams. The connection on protostellar scales is unclear; surveys probing the correlation of core angular momentum direction through outflow direction, large scale magnetic fields, and filament orientation find conflicting results with regard to the mutual orientation of disks and magnetic fields (Stephens et al., 2017; Kong et al., 2019).

Constraining the physics that dominates cluster wide star formation also requires an understanding of what processes are responsible for setting the mass distribution of stars, the stellar initial mass function (IMF). Within our galaxy, the form of the IMF, $d\log N/d\log M$, has been measured to be a power law of slope -1.35 for $M > 1$ $\mathrm{M}_{\odot}$ and a fairly wide log normal form with a characteristic peak around 0.2 $\mathrm{M}_{\odot}$ before a turnover at lower masses for $M < 1$ $\mathrm{M}_{\odot}$ (for a review see: Chabrier, 2003). At the low mass end, it is possible that dense structures, perhaps seeded by supersonic turbulence, fragment out when Jeans unstable. That mapping is not unreasonable, given that in Figure 1.3, a Jeans mass of 0.2 $\mathrm{M}_{\odot}$ on the Jeans length line is fairly centrally located in the protostellar core region. However, a mechanism to explain the turnover toward lower masses is necessary and requires changes to thermal physics in those regimes (e.g. Jappsen et al., 2005).

Given how depopulated the region for densities and temperatures necessary for Jeans masses > 1 $\mathrm{M}_{\odot}$ is in Figure 1.3, the upper-mass power law of the IMF tells us that additional physical processes are required to explain high mass star formation. Turbulence at some spectrum of fluctuations is thought to be able to produce a power law distribution (see: Elmegreen & Efremov, 1997; Padoan & Nordlund, 2002). However, gravitational focusing suggests that additional gravitational accretion should be able to grow power laws at high masses, given some initial distribution of overdensities (see also: Bonnell et al., 2001a; Bonnell & Bate, 2006; Ballesteros-Paredes et al., 2015).

Probing the kinematics and spatial distributions of embedded clusters is another way to constrain the dynamics of the star forming environment. Within embedded clusters, stellar populations often have ages less than the crossing time for the region (Hartmann et al., 2001) and thus are more likely to have been to have retained signatures of their initial conditions barring intense dynamical processing. Multi-fiber high resolution spectrographs and the launch of *Gaia* have allowed for efficient kinematic surveying of young star forming regions. Many regions show the presence of velocity gradients (Tobin et al., 2009) and velocity coherent substructure in the stars (Da Rio et al., 2017) and the gas (Hacar et al., 2017), alike. Explaining these features is important for constraining the past, current, and future dynamical states of molecular clouds and clusters.

The features listed above are not a complete accounting of observations in young clusters, but present a sample of observations that are valuable tools for testing star formation theory. Numerical modeling should seek to explain the observational features of star clusters and make predictions of new observational diagnostics.

1.3 Core and Disk Formation

At the point where structures in star forming clouds reach densities on the order of $n = 10^4 - 10^6$ cm^{-3} and sizes on the order of $0.01 - 0.1$ pc, they are referred to as pre- and protostellar cores with observed lifetimes of $10^5 - 10^6$ yrs (Jessop & Ward-Thompson, 2000). Non-homologous collapse of dense protostellar core material is thought to characterize the protostellar phase (Larson, 1969); this free-fall collapse will drag interstellar dust along, ensconcing a newly formed protostar in a blanket of infalling gas and dust — protostars were first robustly identified by IRAS on account of the excess infrared emission of stellar light absorbed and re-radiated by warm circumstellar dust (Beichman et al., 1986).

Conservation of angular momentum, $L = mv \times r =$ constant, for a closed system means that velocities increase linearly with smaller radii, $v_{rot} \propto R^{-1}$, whereas free-fall velocities scale as $v_{ff} \propto R^{-1/2}$. Thus, protostellar core material with fractional rotational support at $r = 0.05$ pc can be Keplerian at a few 100 AU. The presence of rotationally supported disks around protostars is a natural consequence of gravitational infall during star formation.

Analytic formulations model the formation of disks from cores as a rotating collapse of uniformly rotating material from progressively larger scales (Terebey et al., 1984). The material follows ballistic trajectories, landing at some centrifugal radius. The disk radius grows outward with time as the specific angular momentum of incoming material increases (Cassen & Moosman, 1981). The evolutionary stages of the protostellar phase trace the formation of an embedded protostar with a dusty infalling envelope and protostellar disk as it evolves into a dusty protoplanetary disk and are often inferred from the expected shapes of the infrared spectral energy distribution (Adams et al., 1987).

Due to flux freezing, the effects of magnetic fields on the star formation process become more important at protostellar core densities with $B \propto \rho^{2/3}$. Mass to flux ratios, M/Φ, describe the relative importance of gravity to magnetic effects, where the critical $M/\Phi = 0.13\ G^{-1/2}$ (Mouschovias & Spitzer, 1976) is the boundary between the gravitationally dominant (supercritical) and the magnetically dominant (subcritical) regimes. While molecular cloud cores at protostellar densities have median mass to flux ratios that are twice the critical value (Crutcher, 2012), numerical simulations of collapsing cores whose rotation axes are aligned with magnetic fields are unable to form rotationally supported disks, in what has become known as the 'magnetic braking catastrophe' (Mellon & Li, 2008). Proposed solutions to this problem require limiting the effects of the magnetic field either by invoking various non-ideal MHD effects (e.g. Wurster et al., 2019) or by geometrical misalignment between the rotation and magnetic fields axes (Joos et al., 2012), provided most cores are strongly magnetically supercritical (Krumholz et al., 2013).

As such, the magnitude and direction of the angular momenta and magnetic fields of protostellar cores are the most important properties for constraining the range of initial conditions of disk formation.

1.4 Numerical Methods

In this work, a variety of numerical methods are employed to investigate how molecular gas at multiple scales without significant turbulent support sets the conditions for star and disk formation. Numerical methods are used to solve problems without analytic solutions by integrating systems of equations incrementally forward in time, where the speed of integration will depend on the size of the timestep taken by the code.

The primary equations integrated in numerical astrophysics are for the motions of fluid elements: conservation equations for mass, momentum, and energy, commonly known as the Euler equations.

$$\frac{\partial \rho}{\partial t} + \frac{\partial \rho u}{\partial x} = 0 \tag{1.8a}$$

$$\frac{\partial \rho u}{\partial t} + \frac{\partial}{\partial x}\left(\rho u^2 + P\right) = 0 \tag{1.8b}$$

$$\frac{\partial E}{\partial t} + \frac{\partial}{\partial x}\left(u[E + P]\right) = 0 \tag{1.8c}$$

In fluid dynamics, methods are traditionally separated by whether they adopt the frame of the individual fluid packets, Lagrangian methods, or whether they are in a lab frame, monitoring the changes of quantities on a grid, known as Eulerian methods. Although, new hybrid methods exist which adopt a moving mesh framework in which the grid follows fluid packets through space (Springel, 2010). Most widely used public astrophysical codes are incredibly modular, allowing for the addition of extra physics as source and sink functions in Euler's equations or adding Maxwell's equations in order to include magnetohydrodynamic effects. This flexibility in terms of setting both the initial conditions and the potential physics is conducive for staging numerical experiments and exploring parameter spaces of initial conditions, where a numerical experiment functions much like a traditional empirical inquiry. A hypothesis is posed by varying parameters for a series of simulations and the results are tested against selected observational diagnostics.

The most significant advantage of numerical hydrodynamics over pen and paper analyses is the ability to explore multi-scale and non-linear behavior without oversimplifying starting assumptions. As processing power has increased over time, so has the ability to resolve larger and larger dynamic ranges – a boon for star formation studies.

1.4.1 Techniques for Star Formation

Numerical studies are limited by how computationally expensive it is to fully simulate a specific process. In the star formation context, several modeling considerations arise for the purposes of conserving computational resources. The choice of the equation of state, $P(\rho,T)$, for example, can depend on the length and density scales achievable in a simulation. Many times the choice of an isothermal equation of state greatly simplifies Equations 1.8b-1.8c, avoids timestep limitations during integration due to the requirement of resolving heating and cooling timescales, and makes simulation results rescalable.

In molecular cloud simulations, turbulent velocity fluctuations are typically drawn from an analytic power spectrum (Padoan & Nordlund, 2002), rather than directly developing high Reynolds number flows (as in Heitsch et al., 2006). This approach has enabled numericists to test the effects of various analytic formulations for turbulence, but has the disadvantage of assuming the timescales and momentum input of unmodeled and unknown physical processes.

By far, the most important and contentious numerical construction for star formation simulations is the sink particle. As both Lagrangian and Eulerian methods have computational limits on the maximum achievable density contrasts in a fixed resolution simulation, modeling star formation requires a numerical construction in order to represent the high density regions which will become stars. Sink particles are pressureless and interact with the gas through gravity, allowing for easier computation of the behavior of large mass concentrations and serve as convenient stand ins for stars. However, sink particles are, in essence, sub-grid models — their behavior a combination of prescribed assumptions and solutions to the hydrodynamic equations. Sink particle prescriptions determine the conditions for forming sinks, their fixed effective size, and under what conditions flow properties are transferred to the sink. Designing sub-grid models of sink behavior that are appropriate for their regimes is an area of ongoing work.

1.4.2 Particle based Methods

Lagrangian codes integrate conservation equations by modeling matter as sets of discrete particles. Particle codes can be pressureless (N-body) or simulate the effects of gas pressure by softening particle interactions within a smoothing length, called smoothed particle hydrodynamics (SPH) codes. The advantages of particle methods lie in the fact that the resolution elements are in units of mass; this makes it relatively simple to have different density regimes within the simulation box. While sink particles are still necessary, the resolution criterion for star formation only relies on resolving masses lower than the Jeans mass (Bate & Burkert, 1997). Accretion of mass is relatively simple: particles that are infalling toward the sink within a designated accretion radius are accreted by the sink particle, conserving mass and momentum in the interaction (Jappsen et al., 2005).

Certain astrophysical problems are less suitable for SPH codes, particularly for accurate treatment of angular momentum and magnetic fields. The numerical viscosity of SPH codes can be quite high, especially in regions where the number of particles is inadequate or the mass resolution too poor. Numerical viscosity in these cases leads to angular momentum loss and unrealistic amounts of viscous spreading (see appendix in Bate, 2018). In addition, SPH methods that can also solve magnetohydrodynamics equations are relatively new and rare (Price et al., 2018). For these methods, the magnetic field is not guaranteed to preserve $\nabla \cdot B = 0$ and so they must often rely on on-the-fly divergence cleaning techniques in order to preserve solutions to Maxwell's equations.

1.4.3 Grid Codes

Eulerian codes discretize space, computations occur on a grid of cells. Conservation laws lend themselves well to this treatment; codes simply compute a solution to the Riemann problem at every cell (LeVeque, 1992). While mass, momentum, and energy are computed over finite volumes in the cells, grid codes allow for magnetic fields to be integrated over the area of the cell faces. As magnetic flux is computed over area, not volume, this type of scheme, called constrained transport (CT), reflects the innate geometry of solutions to the induction equation, naturally preserves $\nabla \cdot B = 0$, and reduces numerical dissipation of magnetic fields due to discretization (Evans & Hawley, 1988; Gardiner & Stone, 2008).

The limiting factor for grid codes lies in the feasibility of achieving the appropriate resolution. The Courant-Freidrichs-Lewy (CFL) condition $u\Delta t/\Delta x \leq \mathrm{CFL}_{\mathrm{max}}$ places a limitation on the size of the timestep Δt based on the speed of information u and the resolution Δx (LeVeque, 1992). At very high resolutions, simulations will require many more computational cycles to integrate to the same final time. Adaptive mesh refinement (AMR) has been used to increase the dynamic range of simulations by iteratively increasing resolution in high density areas, keeping low density areas of the simulation box on coarser grids. However, as star forming material is very heterogeneous large gradients in refinement can occur, introducing numerical error when computing quantities across refinement interfaces (see appendix in: Bleuler & Teyssier, 2014).

With sink particles, the minimum sizes and masses will be dictated by resolution, based on the Truelove criterion which requires at least 4 cells per local Jeans length (Truelove et al., 1997). The criteria for assigning mass during sink formation and accretion are less straightforward than in the particle case. Most similar to SPH methods of accretion, threshold accretion methods remove any infalling material within an accretion radius above a certain density (Federrath et al., 2010). However, in the Eulerian framework, instantaneous depletion of the grids surrounding sink particles will artificially increase flow toward the new pressure minimum. Thus, sink methods need to utilize a variety of sub-grid modeling algorithms to smooth out mass removal across multiple cells, prescribe mass accretion rates based on nearby cell properties, and ensure overall momentum conservation across a selected volume (see: Bleuler & Teyssier, 2014; Gong & Ostriker, 2013; Krumholz et al., 2004, and references therein).

1.5 Becoming Protoplanetary: Disk Formation from the Top-Down

In this thesis, I motivate and investigate star and star-cluster formation from a self-gravitating globally collapsing molecular cloud. Supposing that hydrodynamic turbulence will be important in early, low-density phases of clouds, where the energetic requirements are easier, and gravity will dominate when clouds become denser and more massive, our model clouds start out with supersonic hydrodynamic turbulence, but don't continue driving it. This enable us to isolate the effects of gravity at various scales and times. The first part of the thesis (Chapters 2-4) concerns the consequences of sub-virial (cold collapse) conditions in molecular cloud material, in terms of collecting cluster forming material, producing archetypal cluster morphologies, and the dynamical evolution of hierarchically formed systems. Each chapter aims to test the cold collapse model by evaluating whether it can produce key observational diagnostics at the relevant scales. The second half (Chapters 5-7) focuses on a series of simulations across a parameter space of resolutions and initial cloud conditions in order to probe how cloud scale properties influence the attributes of protostellar populations that determine the course of disk formation and evolution: core and protostar mass accretion rate, magnetization, and angular momentum.

In Chapter 2, we posit that gravitational focusing can form star clusters that follow the observed $d\log N/d\log M = M^{-1}$ power law for the star cluster initial mass function (scIMF) (Fall et al., 2010). Motivated by earlier work using SPH simulations and standard sink accretion mechanisms that found that groups of accreting sinks follow a BHL-like mass accretion rate, $\dot{M} = \alpha M^2$, offset by local variations in α, and grow power law distributions to the $d\log N/d\log M = M^{-1}$ form (Ballesteros-Paredes et al., 2015), we decided to test the applicability of BHL accretion to the scIMF. We use *ChaNGa* (Jetley et al., 2008), an N-body code, to look at how gravitational focusing would act in a pressureless system without an explicit sink or accretion scheme. Our analysis consisted of a hierarchical Friends-of-Friends (FOF) clustering algorithm in order to identify and measure the masses of clustered groups of particles over the course of the simulation and calculating the growth of mass in these structures over time. We found an $\dot{M} \propto M^2$ scaling that led to the observed scIMF power law, suggesting that at large scales gravity alone can drive flows that efficiently concentrate star forming material.

In Chapter 3, we adopt a model that assumes that molecular clouds are formed rapidly without significant support at cloud scales such that the initial conditions for star cluster formation are sub-virial. Based off of earlier work (Hartmann & Burkert, 2007; Proszkow et al., 2009) that modeled key observational signatures of an Orion-like embedded cluster with significant contributions from gas self-gravity, we also adopted Orion as our test case. Using the SPH code *Gadget2* (Springel, 2005), we found that cold collapse of an elongated molecular cloud was naturally filamentary, producing the canonical hub-spoke morphology (Myers, 2009) with an ONC-like mass segregated cluster embedded in a larger Orion A-like filament. While we identified some potential observational signatures of infall and characterized the importance of the gas potential in determining the dynamical state of an embedded region, we also found that local dynamical processing was very effective in removing kinematic signatures of infall on cluster scales.

In Chapter 4, motivated by observational studies that identified velocity substructure in the stars (Da Rio et al., 2017) and the gas (Hacar et al., 2017) in Orion, we performed a new analysis on our simulations from (Kuznetsova et al., 2015). Adopting a method for identifying and characterizing velocity coherent groups of stars in our simulations, we find that the multi-scale and filamentary nature of gravitational collapse lends itself well to the formation of local subclusters, each with their own dynamical histories.

In Chapter 5, we port our cold collapse model to the MHD grid code *Athena* (Stone et al., 2008) with a new sink implementation (see methods in: Bleuler & Teyssier, 2014; Gong & Ostriker, 2013). The sink method allows for novel tracking of the cells in the sink environs, such that core scale properties can be tracked but continue to be evolved hydrodynamically without being removed from the simulation. Utilizing the patch cells in the analysis enabled us to contextualize sink behavior within the star forming environment and incorporate our understanding of star formation as a hierarchical process, where infall of material happens over scales larger than the Jeans length. This approach allowed us to demonstrate that measuring the BHL relationship at core scales leads to a $\dot{M} = \alpha M^2$ relationship that has very low scatter, compared to the scaling using default sink masses, with implications for the growth of the stellar IMF.

In Chapter 6, we conduct a parameter study with our *Athena* models in order to examine how the cores in our simulations accrete angular momentum, testing the idea that cores inherit angular momentum directly from cloud scales, as assumed by traditional models of disk formation (Terebey et al., 1984). Angular momentum, tracked by the sink-patch implementation, does not get accreted smoothly and uniformly from the surrounding medium. The local stellar density actually has a bigger impact on the angular momentum content of cores than the initial cloud scale rotation with subsequent accretion affecting the direction of the angular momentum axis and preventing monotonic growth of specific angular momentum over time.

Finally, in Chapter 7, we extend our previous studies with *Athena* to the MHD regime and examine the role of magnetic fields at cluster and core scales. We test our cloud scale results against observations: measurements of the magnetization of cloud cores (Crutcher, 2012) and plane of sky magnetic field maps from Planck (Planck Collaboration et al., 2016), and characterize the distribution of magnetic field and angular momentum magnitudes and directions for cores in our simulation. We find that gravitational infall still dominates the dynamics of core formation and accretion and ensures that the heterogeneity in the star formation environment is directly related to the non-isotropic and episodic nature of accretion onto cores. This type of accretion, heterogeneous in space and time, implies a qualitatively different picture of the early stages of protostellar cores and their nascent disks which we discuss in Chapter 8.

CHAPTER 2

Gravitational Focusing and the Star Cluster Initial Mass Function

This chapter appears in the Astrophysical Journal, Volume 836(2), pp 190 (Kuznetsova et al., 2017). This work was co-authored with Lee Hartmann and Andreas Burkert. The paper is reproduced here with minor stylistic revisions.

2.1 Abstract

We discuss the possibility that gravitational focusing, is responsible for the power-law mass function of star clusters $N(\log M) \propto M^{-1}$. This power law can be produced asymptotically when the mass accretion rate of an object depends upon the mass of the accreting body as $\dot{M} \propto M^2$. While Bondi-Hoyle-Littleton accretion formally produces this dependence on mass in a uniform medium, realistic environments are much more complicated. However, numerical simulations in SPH allowing for sink formation yield such an asymptotic power-law mass function. We perform pure N-body simulations to isolate the effects of gravity from those of gas physics and to show that clusters naturally result with the power-law mass distribution. We also consider the physical conditions necessary to produce clusters on appropriate timescales. Our results help support the idea that gravitationally-dominated accretion is the most likely mechanism for producing the cluster mass function.

2.2 Introduction

In recent years significant progress has been made on the form of the stellar cluster IMF (scIMF; Zhang & Fall, 1999; de Grijs et al., 2003; McCrady & Graham, 2007). As summarized by Fall & Chandar (2012), clusters in the Milky Way (Lada & Lada, 2003), Magellanic Clouds, M83, M51, and the Antennae exhibit a similar power-law mass function with $d\log N/d\log M \equiv \Gamma = -0.9 \pm 0.15$. Others suggest a Schechter-type mass function is a better fit, with a truncation at high masses (Gieles et al., 2006; Bastian, 2008); however, all agree on the power-law behavior of $\Gamma \sim -1$ at lower masses.

One explanation for the scIMF has been that it simply reflects the mass distribution of parent giant molecular clouds (e.g., Elmegreen & Efremov, 1997), perhaps with some accounting for feedback by stellar energy input (Fall et al., 2010). However, the observed mass functions of inner Milky Way giant molecular clouds (GMCs) yield $\Gamma \sim -0.5$ (Williams & McKee, 1997); the Antennae also show similarly flat mass functions (Wilson et al., 2003; Wei et al., 2012), although outer Milky Way clouds may exhibit $\Gamma \lesssim -1.1$ and LMC clouds $\Gamma \sim -0.7$ (Rosolowsky, 2005). Moreover, while GMC masses obviously provide an upper limit to cluster masses, it isn't obvious why the global cloud mass function should be reflected in cluster masses that are one to two orders of magnitude smaller. Even if the fraction of dense gas which can form clusters is similar among molecular clouds (and the evidence for this is mixed; see Bastian, 2008; Lada et al., 2010; Burkert & Hartmann, 2013; Battisti & Heyer, 2014), the manner in which the dense gas component might be broken up into individual protocluster clouds is not necessarily the same (see Hennebelle, 2012, for a model of modified turbulent acccretion).

Long ago, Zinnecker (1982) showed that if bodies accrete mass at a rate proportional to the square of their mass, $\dot{M} \propto M^2$, a population with a narrow initial mass range will develop a power-law mass distribution which asymptotically approaches $\Gamma = -1$. Zinnecker pointed out that "Bondi-Hoyle-Lyttleton" (BHL) accretion, with a mass accretion rate characterized by

$$\dot{M} = \frac{4\pi G^2 M^2 \rho_\circ}{(c_s^2 + v_\infty^2)^{3/2}} \equiv \alpha M^2 \,, \tag{2.1}$$

(see discussion in Edgar, 2004) has the requisite dependence on the central gravitating mass M.

In the standard picture of BHL accretion, a central gravitating mass, M, travels through an infinitely large ambient medium $\rho_\circ$ which has constant sound speed c_s at constant relative velocity v_∞. The mass's gravity focuses material into a wake bound to the object from which it accretes material at the rate in Eq. 2.1. But the molecular clouds within which stars and clusters form exhibit density and velocity fields that are far from uniform; in addition, the cloud itself is self-gravitating. Nevertheless, using isothermal SPH simulations with decaying turbulence, Ballesteros-Paredes et al. (2015) (BP15) demonstrated the development of power-law sink mass functions with $\Gamma = -1$. These results suggest that gravitational focusing - which is at the heart of the BHL accretion process - is able to operate despite the complex, time-variable environment.

In this contribution, we examine the conditions for which gravitational focusing can produce star clusters with the required mass function. We show that observations of cluster-forming clouds are consistent with the requirements provided the observed supersonic velocity distributions are understood as being gravitationally-generated rather than turbulence driven by an external agent. We suggest that the signature of the dominance of gravitational over thermal physics is the power-law behavior of the mass function thereby linking the cluster and stellar IMF.

2.3 Numerical Simulations

The power-law sink mass functions found by BP15 were produced in SPH calculations with an initial supersonic velocity field but allowing the turbulence to decay. To minimize the role played by thermal physics, an isothermal equation of state was adopted. If, as suggested by the possible connection with BHL accretion gravity dominates, a similar result should be found with gravitational accretion without including any gas physics. We therefore explore results using a pure N-body code.

2.3.1 Numerical Setup

To test the scenario of purely gravitational accretion, we use the *ChaNGa* (Charm N-body GrAvity solver) code (Jetley et al., 2008; Menon et al., 2015). Since *ChaNGa* is a cosmological code, using the "dark matter" particle implementation ensures that all interactions are purely gravitational, with no gas physics included. With a standard Λ-CDM cosmology, we choose a set of units in which the code length unit corresponds to 1 kpc of proper distance, the mass unit is 2.22×10^5 $M_\odot$ and the time unit is 1 Gyr. For generality, the simulation can be rescaled to representative values. Particles are originally distributed so as to have a uniform density within the chosen geometry. We generate a three dimensional initial turbulent velocity field with the Kolmogorov power law spectrum $P(k) \propto \mathbf{k}^{-11/3}$ with maximum wavenumber $k_{max} = 64$, so that each run is seeded with turbulent velocity fluctuations. The primary function of the initial turbulence is to 'stir' up random density fluctuations.

We include both spherical and disk geometries, run with different random seeds. The initial conditions are sub-virial for both cases, with the initial virial parameter, $\alpha_i = 2|K|/|U| = 5\sigma^2 R/GM$, given in Table 2.1, leading to an overall collapse. All runs have particle distributions of total mass $M = 1$, total radius $R = 1$, and we use $G = 1$ in code units; disk runs start off with a thickness, $h = 0.1$. We employ the default periodic boundary conditions, with a box size set to $10R$, to avoid interactions with the boundary. Force smoothing to avoid tight binaries is implemented in the form of a softening parameter ε, based on Dehnen (2001). Table 2.1 lists each run and its relevant parameters.

2.3.2 Cluster Finding with FOF

To evaluate the formation of star clusters over time in the simulation, we implement a cluster finder based on the Friends of Friends (FOF) algorithm. FOF has been widely used in the cosmology community as a halo-finder instrumental in extracting halo mass functions from simulations (Knebe et al., 2011). The algorithm has only one free parameter, the linking length b, and operates on a set of particle positions in three dimensions. To locate clusters, the algorithm iteratively

Table 2.1: List of *ChaNGa* runs: Relevant parameters include; number of particles, N, initial average interparticle distance $\bar{\ell}$, softening parameter, ε, minimum scale of turbulent fluctuations ℓ_k, and initial virial parameter α_i.

run	N	geometry	seed	$\bar{\ell}_i$	ε	min ℓ_k	α_i
40s1b	40000	sphere	1	0.047	0.001	0.016	0.01
40s2b	40000	sphere	2	0.047	0.001	0.016	0.01
40d1b	40000	disk	1	0.031	0.001	0.016	0.01
40d2b	40000	disk	2	0.031	0.001	0.016	0.01
400s1b	400000	sphere	1	0.021	7E-4	0.016	0.01
400s2b	400000	sphere	2	0.021	7E-4	0.016	0.01
400d1b	400000	disk	1	0.015	7E-4	0.016	0.01
400d2b	400000	disk	2	0.015	7E-4	0.016	0.01

determines all the particles in a group that are within the linking length b away from at least one other particle in the group.

The FOF algorithm offers a few advantages as a cluster finder: it is easier to capture irregular structures, an advantage when looking for stellar clusters, unlike some density threshold methods that construct halos/clusters out of spheres. With only one free parameter, there is relatively little fine tuning needed to produce mass functions, as long as there is some basis for the selection of the linking length.

To generate complete mass functions that probe substructure across different size scales, we use a hierarchical FOF. This approach utilizes a range of linking lengths to generate several sets of mass functions, with smaller values of the linking length finding smaller sub-structures. The mass functions generated at each scale can be summed, removing duplicate structures where applicable to create one hierarchical mass function. We empirically determine the base linking length for our setup by using the value that optimizes both the amount of particles in groups and the number of groups created. For most of the setups, this value runs close to $0.2\bar{\ell}_i$, where $\bar{\ell}_i$ is the initial average interparticle distance, which guarantees groups that are at least 125 times denser than the initial state and an overdensity of at least 3 above the expected interparticle density if the final state were homogeneous. With hierarchical FOF, we probe down to $0.08\bar{\ell}_i$ at maximum .

The final step for our cluster finder is to filter out structures that are clusters of clusters, which we don't want to include in our analysis. In the case of FOF, clusters that are adjacent to one another can be grouped together into one single cluster, even if they are not representative of a single object. To filter out these cases, we adopt a criterion based on the behavior of the average cluster density with mass. In a mass accretion scenario that produces large scale structures by the accretion of smaller scale structures onto a larger gravitating bound structure, the mean densities of more massive structures tend to increase. This will not be true for clusters of clusters, which are grouped solely on the basis of their adjacency. The average density of these objects flattens out and decreases, consistent with groups that are growing more in radius than they are in mass.

In Figure 2.1, we see that there exists a rough truncation mass above which the clusters are likely to be clusters of clusters due to a turnover in average cluster density. By only including clusters less massive than the truncation mass in our analysis, we remove clusters of clusters, but keep all sub-structures that comprised them due to the hierarchical nature of the data sets.

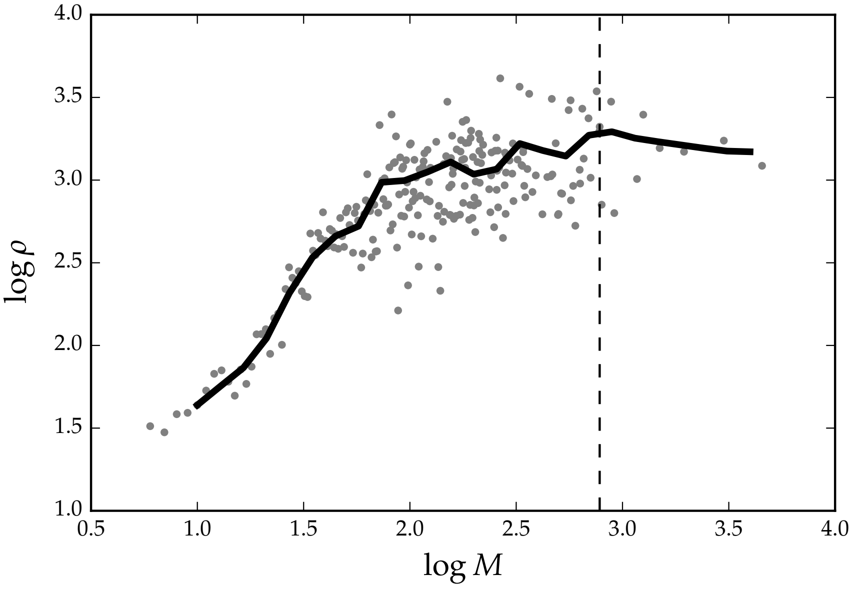

Figure 2.1: Sample view of the upper mass refinement process. Gray dots show the mean density of groups at that mass. The black solid line is the interpolated mean density binned by mass. The identified threshold location is the maximum of the interpolation, where the overall density trend starts to decrease, shown as a black dashed line. In this example, the mass function will be truncated at masses above $\log M = 2.89$.

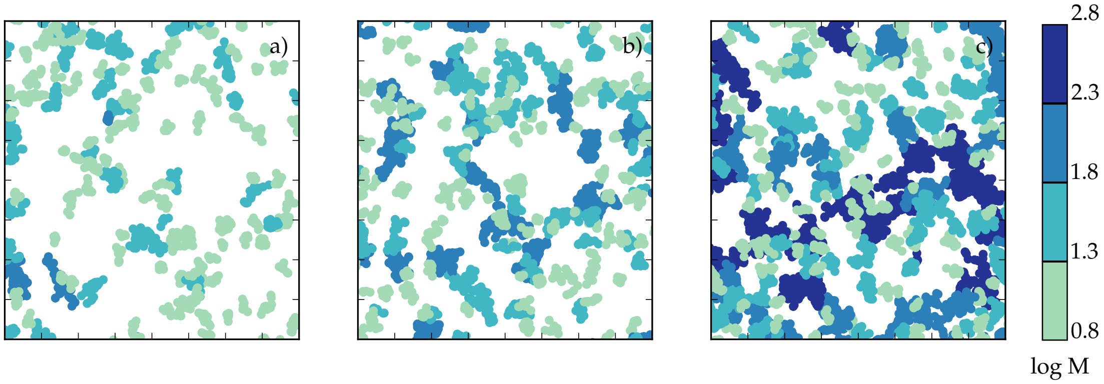

Figure 2.2: Thick slice of a central box $0.4R \times 0.4R \times 0.2R$ in volume, where clusters are color coded by mass. In units of initial free-fall time, panels a)-c) are taken at t = 0.8, 1.0, and 1.3. Scaling to typical molecular cloud values, the time between panels is $\Delta t = 2.74$Myr.

2.3.3 Results

2.3.3.1 Cluster Growth Through Gravitational Focusing

In Figure 2.2, we present a series of three epochs of cluster formation in run 40s1b. Run 40s1b is an initially spherical distribution of 40000 particles. In Figure 2.3, we show the time evolution of its mass function, where the right panels of the Figure correspond to the three epochs in Figure 2.2. (For the sake of generality, we will use the number of particles in a cluster as a proxy for the mass of the cluster for all figures, i.e. $M = N[\bar{m}]$). Figure 2.2 frame a) shows an initial phase where most groups are of a similarly low mass. At this point, over half of the particles in the simulation can be assigned to a group. This distribution is a result of the initial turbulent mixing in the simulation. By the epoch in Figure 2.2 frame b), some intermediate mass groups have been created. We see this in the corresponding frame in Figure 2.3 d), where the tail of the distribution has started to grow, creating a shallower slope. In the last epoch shown in Figure 2.2 c) and the last panel of Figure 2.3, the intermediate mass clusters have rapidly accreted new members, such that many of them are now some of the most massive clusters and the mass function has grown to approach the asymptotic $\Gamma = -1$ slope. While at this stage, all groups found by FOF are bound by virtue of the virial parameter $\alpha < 1$, there is a subset of particles that were not assigned to groups and remain unbound. We include the final power law fits of the mass function for all runs in Table 2.2, as well as sample values for fits with small and large numbers of bins. The "averaged" slope values are a weighted average of fits over a range of bin sizes and different density refinement algorithms.

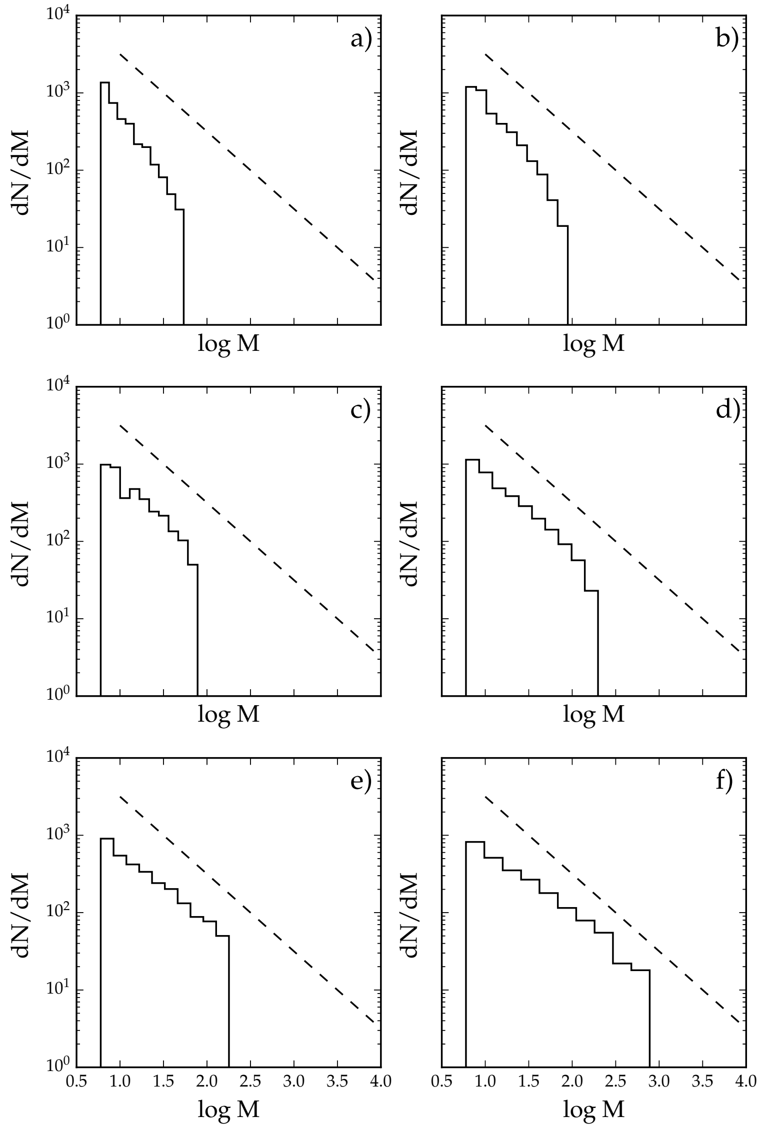

Figure 2.3: Time evolution of the mass function for run 40s1b, a set of 40000 particles initially distributed in a homogeneous spherical distribution. Particle number is used as a proxy for mass here. The dashed line has a slope of -1. Frames a)-f), in units of initial free-fall time, are take at t = 0.52, 0.77, 0.90, 1.02, 1.15, and 1.3 . Adopting typical molecular cloud values we can rescale such that the time between snapshots $\Delta t = 1.37$Myr.

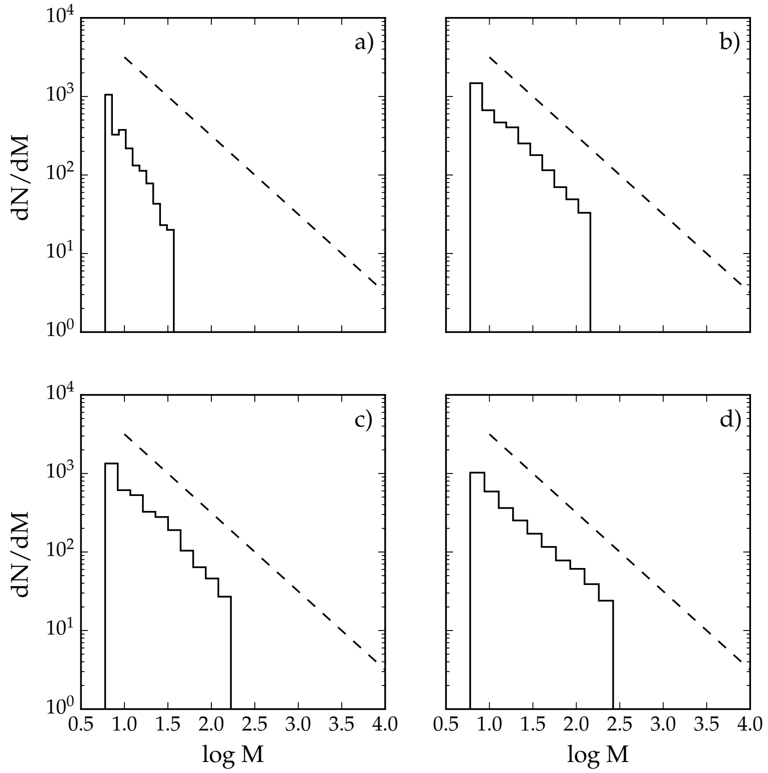

Figure 2.4: Time evolution of the mass function for run 40d1b, a set of 40000 particles initially distributed in a homogeneous disk. Particle number is used as a proxy for mass here. The dashed line has a slope of -1. Frames a)-d), in units of initial free-fall time, are taken at t = 0.50, 0.65, 0.80, 0.95

In the final frame (f), the mass function appears to be a little flatter than -1 at lower masses, but this is inevitable, the reasons for which are twofold: the initial conditions and the limits on the cluster finder. First, the $\Gamma = -1$ limit is an asymptotic one, and as the starting cloud is finite, eventually smaller mass clumps will simply cease to form due to a lack of replenishing material. Second, while a hierarchical mass function ought to probe the substructure of clumps, we are limited by the smallest linking length we set for the cluster finder: an arbitrary limit due to computational constraints.

In Figure 2.4, we find that the flatter feature does not exist in the disk geometry; the mass functions produce a relatively constant slope across the entire mass range. Disks are prone to an edge effect, where the outside of the disk tends to collect a ring of particles as it contracts (Burkert & Hartmann, 2004). This thin layer of excess pile-up creates a region with an overabundance

Table 2.2: Fits for the mass function slope of all *ChaNGa* runs: Slope of the power law mass function is given for each run in terms of 'averaged', min, and max values. For each run, fits were taken using three different density refinement techniques and using 10 different values for the binning. Min and max values for the fit are sample values taken for the smallest and largest number of bins, respectively. The 'averaged' value corresponds to a weighted average of the fit to the slope across all binnings and truncation masses.

run	slope ± error (averaged)	slope ± error (min)	slope ± error (max)
40s1b	-0.89 ± 0.03	-0.87 ± 0.03	-0.90 ± 0.03
40s2b	-0.91 ± 0.08	-0.80 ± 0.04	-0.95 ± 0.04
40d1b	-0.99 ± 0.04	-1.07 ± 0.05	-1.01 ± 0.04
40d2b	-1.06 ± 0.03	-1.06 ± 0.03	-1.09 ± 0.05
400s1b	-0.99 ± 0.05	-0.90 ± 0.03	-1.00 ± 0.02
400s2b	-0.98 ± 0.06	-0.85 ± 0.04	-1.00 ± 0.03
400d1b	-1.18 ± 0.04	-1.20 ± 0.03	-1.16 ± 0.02
400d2b	-1.17 ± 0.04	-1.10 ± 0.03	-1.20 ± 0.03

of lower mass groups which, in this case, compensates for the underpopulation of lower mass clusters we see in the spherical geometry. Despite these differences, slopes between the different geometries vary by < 0.2.

.

2.3.3.2 Mass Accretion History

For additional insight into the development of the mass function, we look at the mass accretion history of representative groups. Selecting groups from the power law tail of the distribution, we characterize the fashion in which the group attains mass by tracing the former groups its members belonged to over time. We can demonstrate that for a typical group at early times there exists a dominant sub-group which will attract smaller groups and accrete them (Figure 2.5). Combined with the demonstration that the $\Gamma = -1$ power law is not present at early times, it is unlikely that the mass distribution we see is seeded in the initial conditions, but instead is a function of gravitationally-driven accretion from a random distribution.

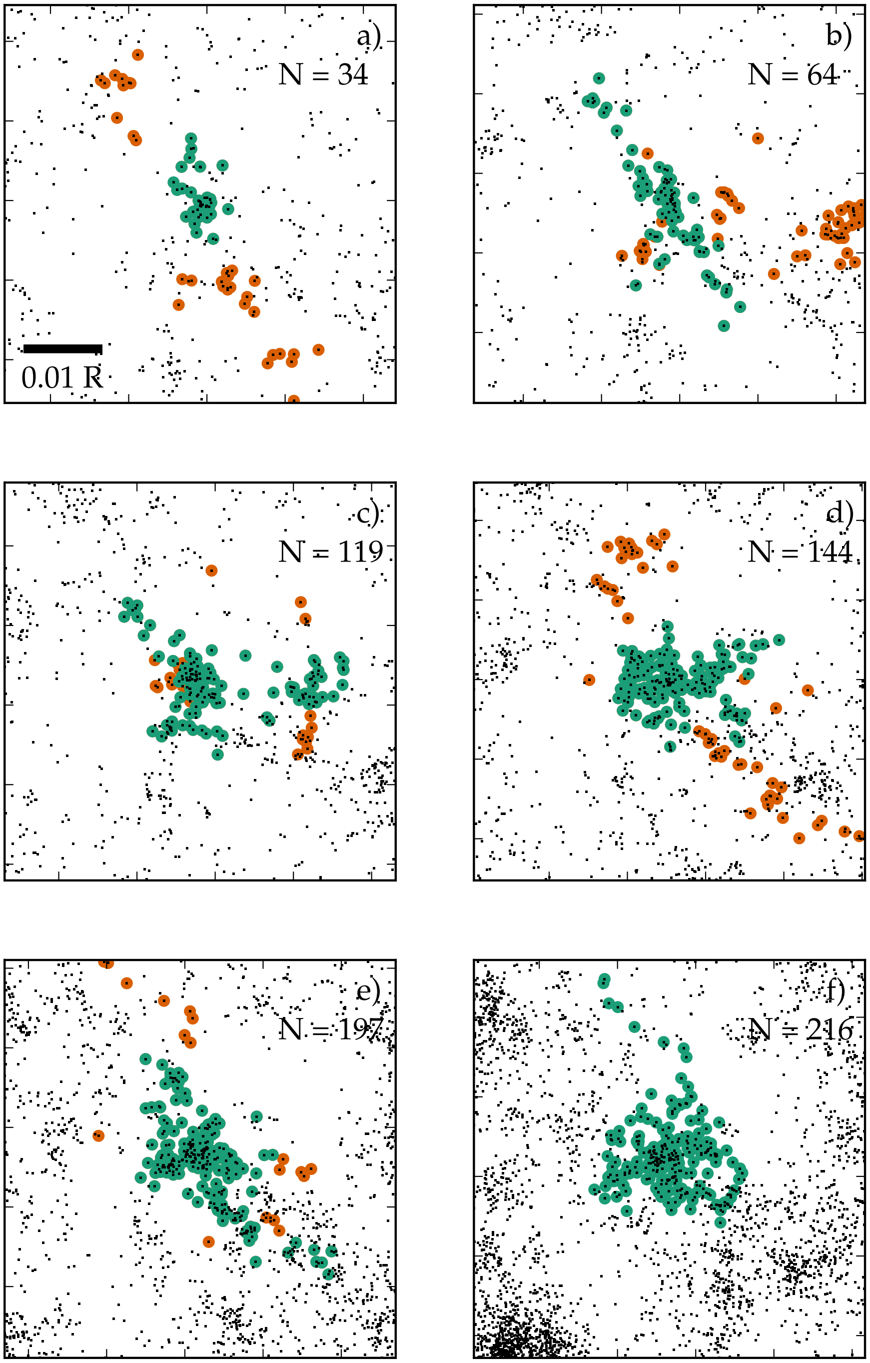

Figure 2.5: Mass accretion through time for a sample group from run 40s1b on the higher mass tail of the mass function for run 40s1b, each panel corresponds to the one shown in Figure 2.3. Teal circles represent members of the largest group, orange circles represent members that will be accreted onto the group between snapshots. Black dots plot a projection of all particles in view.

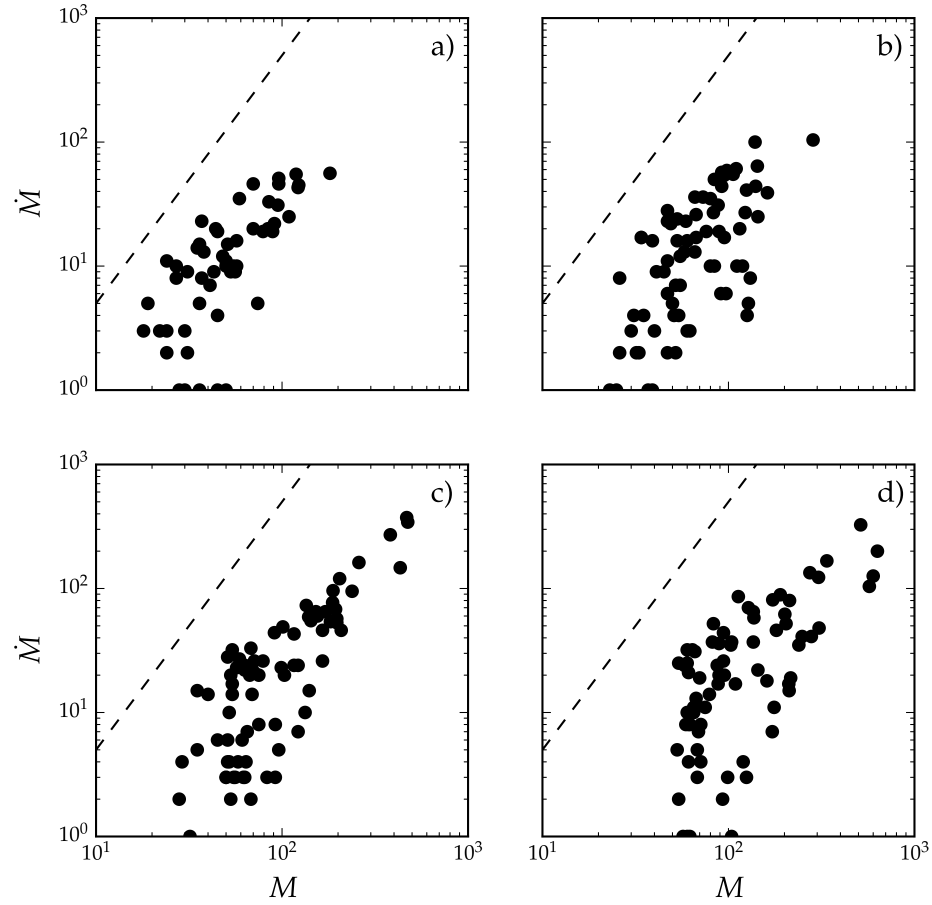

Figure 2.6: $M vs \dot{M}$ on an arbitrary scale for run 40s1b. These panels correspond to the last 4 panels of Figures 2.3. The dotted line has a slope of 2 in log space, representing the canonical $\dot{M} \propto M^2$ relation.

2.4 Gravitational focusing vs. BHL accretion

As mentioned in the Introduction, Zinnecker (1982) showed that if the accretion of an initial population of similar masses scales directly as M^2 (as is the limiting case of BHL accretion), $\Gamma \rightarrow -1$ asymptotically. As shown in Fig. 2.6, $\dot{M}$ vs M starts off as roughly M^2, but later shows bending at low and high masses. The same behavior was seen in BP15, in which the SPH simulation nevertheless produced a $\Gamma = -1$ power law in the sink mass function. BP15 attributed this to "starving" the small masses by competition with higher mass sinks, and slowing down the high masses due to depletion of their environments. But if the strict BHL accretion formula, or a pure

$\dot{M} \propto M^2$ is not strictly applicable, why does $\Gamma \to -1$?

In the case of the SPH runs with sink formation, BP15 suggested that the answer was that the gas densities and velocities were uncorrelated with the final sink mass; thus on average the M^2 dependence wins out. They found that specific *local* groups of sinks, embedded in similar environments, exhibited accretion rates proportional to M^2 but with different values of α (equation 2.1) for differing groups. BP15 then argued that adding up the individual groups with similar power-law distributions results in a common power law.

The difficulty with attempting to find an analytic or schematic understanding of the development of the mass function is that the environment is not static, but instead is strongly perturbed by the formation of local centers of gravitational attraction. A naive application of the BHL formula (equation 2.1) might suggest that accretion over large enough scales to make massive clusters is difficult, given the observed increase in cloud velocity dispersions with increasing size (Larson, 1981). However, as Heyer et al. (2009) showed, the Larson velocity-size relation for molecular clouds is consistent with near-virial motions, as would be expected if gravity were the driving force (see also Ballesteros-Paredes et al., 2011). In this case it is difficult to identify the appropriate value of v to use in equation 2.1, and so formally the BHL accretion picture doesn't apply. However, the power-law mass function that results and its development with time (Figures 2.3, 2.4) is quite similar to simulations of pure BHL accretion (see, e.g., Figure 10 in Hsu et al., 2010)). Perhaps a schematic way of understanding the results is that the initial random velocity fluctuations average out so that overdensities can accrete matter at a rate $\propto M^2$. Whatever the interpretation, the common results of both the SPH simulations in Ballesteros-Paredes et al. (2015) and the N-body calculations in this chapter provide strong evidence for gravitational accretion producing power law distributions with $\Gamma \sim -1$.

2.5 Discussion

The simulations in this chapter and in Ballesteros-Paredes et al. (2015) refer to collections of particles and sink particles, respectively. Protostar clusters involve a combination of gas and stars. To apply our results to real clusters, we must assume that the protocluster gas + star mass function maps directly into the final scIMF. This seems reasonable because the total mass in stars is generally thought to be $\gtrsim 0.3 - 0.5$ of the original protocluster cloud mass for the cluster to remain gravitationally bound (unless gas loss is extremely slow; Hills, 1980; Mathieu, 1983; Geyer & Burkert, 2001; Lada & Lada, 2003). Star formation regions with lower star formation efficiencies will likely not be able to become clusters at all (Kroupa et al., 2001). In addition, observations of nearby star clusters, like the ONC, show that clusters themselves form in regions of dense gas at high efficiencies, without significant contributions from diffuse gas components of molecular clouds (Hillenbrand & Hartmann, 1998). Moreover, the similarity of cluster mass functions both younger and older than 10 Myr in the interacting galaxy system of the Antennae and the LMC, suggests that feedback does not alter the shape of the cluster mass function (Fall et al., 2010).

Our identification of the cluster mass function as a result of gravitationally-driven accretion implies that clusters form subvirially. Generally speaking, the formation of a massive star cluster must occur in $\lesssim 3 - 10$ Myr, to avoid disruption by the energy input from the massive stars. This requires that the free-fall time be ~ 10 Myr or less, which requires molecular hydrogen densities $\gtrsim 100cm^{-3}$, a plausible value for molecular clouds. The other requirement is that expansion velocities or dispersions be at most roughly virial (assuming some dissipation of supersonic motions). While observed velocity dispersions of molecular clouds increase with increasing scales (Larson's first law; Larson, 1981), recent observations suggest that these motions are roughly virial (Heyer et al., 2009) (see also Larson (1981)). If the supersonic velocities are largely gravitationally-driven, avoiding the problem of too rapid dissipation (Ballesteros-Paredes et al., 2011), this second criterion is automatically satisfied.

Testing the hypothesis of gravitationally-driven accretion and/or subvirial initial conditions directly with the currently available observations is difficult (Proszkow et al., 2009; Kuznetsova et al., 2015), but the advent of Gaia may make it possible to search for collapse in statistically-significant samples of stars, especially combined with radial velocity measurements (Tobin et al., 2009; Kounkel et al., 2016; Da Rio et al., 2016). The gravitationally-driven accretion seen in simulations tends to form infalling filamentary streams, and this may be observable in the gas using appropriate molecular tracers.

Morphological tests are possible and even easier to apply. As Burkert & Hartmann (2004) showed, gravitational focusing tends to produce concentrations of mass in finite clouds near regions of smaller radii of curvature at the cloud edge; the simplest example of this is formation of dense gas near the ends of filamentary clouds. While this picture is consistent with the spatial structure of the Orion A cloud (Hartmann & Burkert, 2007), it might be possible to put this on a firmer statistical basis, using large-scale maps from the *Spitzer* and *Herschel* Space Telescopes and other facilities (Churchwell et al., 2009; André et al., 2010; Mairs et al., 2016).

Our picture of gravitationally-focused accretion naturally explains the tendency of stars to form in groups and clusters. It is also consistent with the idea that the supersonic motions in dense molecular clouds tend to be driven by gravity (Ballesteros-Paredes et al., 2011). Finally, this picture suggests a close connection with the upper-mass slope of the stellar IMF (Ballesteros-Paredes et al., 2015), with departures from the limiting $\Gamma = -1$ slope to that of the Salpeter value arguably the result of feedback from high-mass stars halting accretion.

Detailed numerical simulations of star and cluster formation in galaxy models with complicating effects such as stellar feedback and magnetic fields could probe the limits of this simple picture and help constrain the expected masses of star clusters as a function of environment for comparison with observations.

2.6 Acknowledgements

AB acknowledges important conversations with Clare Dobbs, LH with Mike Fall, Javier Ballesteros-Paredes, and Mark Heyer. This work was supported in part by NASA grants NNX16AB46G and NNH15ZDA001N-XRP,by the University of Michigan, and in part through computational resources and services provided by Advanced Research Computing at the University of Michigan, Ann Arbor.

CHAPTER 3

Signatures of Star Cluster Formation by Cold Collapse

This chapter appears in the Astrophysical Journal, Volume 815(1), pp 27 (Kuznetsova et al., 2015). This work is co-authored with Lee Hartmann and Javier Ballesteros-Paredes. The paper is reproduced here with minor stylistic revisions.

3.1 Abstract

Sub-virial gravitational collapse is one mechanism by which star clusters may form. Here we investigate whether this mechanism can be inferred from observations of young clusters. To address this question, we have computed SPH simulations of the initial formation and evolution of a dynamically young star cluster through cold (sub-virial) collapse, starting with an ellipsoidal, turbulently seeded distribution of gas, and forming sink particles representing (proto)stars. While the initial density distributions of the clouds do not have large initial mass concentrations, gravitational focusing due to the global morphology leads to cluster formation. We use the resulting structures to extract observable morphological and kinematic signatures for the case of sub-virial collapse. We find that the signatures of the initial conditions can be erased rapidly as the gas and stars collapse, suggesting that kinematic observations need to be made either early in cluster formation and/or at larger scales, away from the growing cluster core. Our results emphasize that a dynamically young system is inherently evolving on short timescales, so that it can be highly misleading to use current-epoch conditions to study aspects such as star formation rates as a function

of local density. Our simulations serve as a starting point for further studies of collapse including other factors such as magnetic fields and stellar feedback.

3.2 Introduction

Most stars form in clusters (Lada & Lada, 2003), and our own Sun is likely no exception (Adams, 2010). As a building block of star formation, the dynamical state of molecular clouds plays an important role in determining the properties of star clusters. Theoretical studies of young star clusters have generally started with a relatively dense cloud of gas with "turbulent" motions that are approximately virial (e.g., Bate et al., 2003; Scally et al., 2005; Tan et al., 2006; Price & Bate, 2008; Bonnell et al., 2008; Hennebelle, 2012; Myers et al., 2014). In the case of numerical simulations, this choice of initial conditions is often made for practical reasons, but this begs the question of how the protocluster gas (and stars) formed (with quasi-virial motions) in the first place.

Generally speaking, there are two main pictures of the formation of star clusters. The first posits some type of structuring in the molecular cloud which results in massive clumps which initially are supported by roughly virial (and supersonic) motions (Tan et al., 2006; Hennebelle, 2012), while the second invokes gravitational collapse (Hartmann & Burkert, 2007; Elmegreen, 2007; Allison et al., 2009, 2010; Allison & Goodwin, 2011). Several studies have addressed the issue of cluster evolution after the stars have been born and investigated whether gas removal by stellar feedback is important (Lada et al., 1984; Kroupa, 2000; Kroupa et al., 2001; Scally et al., 2005; Kruijssen et al., 2012; Moeckel et al., 2012), but relatively little attention has been given to the formation of the protocluster gas (Hartmann & Burkert, 2007; Elmegreen, 2007; Hennebelle, 2012).

With the advent of multifiber, high-resolution spectrographs, it has become possible to study the stellar kinematics in star-forming regions efficiently (Fűrész et al., 2008; Tobin et al., 2009; Tobin et al., 2015; Foster et al., 2015; Cottaar et al., 2015). The populous Orion Nebula Cluster (ONC), with substantial amounts of molecular gas and continuing star formation is of particular interest as it is potentially young enough (e.g., Da Rio et al., 2010) to show kinematic signatures of their formation. Fűrész et al. (2008) and Tobin et al. (2009) showed that most of the ONC stars that can be studied optically have radial velocities consistent with those of the molecular gas, with a substantial velocity gradient north of the cluster center in contrast to the southern region. This kinematic behavior led Tobin et al. (2009) to suggest that ONC gas and stars are still infalling, though others have argued that the ONC is in expansion (Da Rio et al., 2014; Kroupa et al., 2001) or approximate equilibrium (Tan et al., 2006).

Previous numerical work focused on simulating young clusters with applications to the ONC has primarily utilized N-body simulations without including the gravity of the gas. These studies have shown that initial substructure is rapidly smeared out (Scally & Clarke, 2002; Parker & Meyer, 2012; Parker et al., 2014), mass segregation such as that observed in the ONC (Hillenbrand & Hartmann, 1998) occurs rapidly (Allison et al., 2010), and that attempts to fit the current distribution of stars in the ONC to a specific scenario yield a host of possible initial conditions (Scally et al., 2005; Allison et al., 2010; Parker & Meyer, 2012; Parker et al., 2014). However, the presence of significant masses of gas in very young clusters means that the self-gravity of the gas can be important in determining the gravitational potential and thus whether clusters like the ONC are bound or not (Hillenbrand & Hartmann, 1998).

Proszkow et al. (2009) took an initial step toward including the gas along with cluster stars by modeling it with a static potential included in the N-body calculations. They showed that sub-virial , with $E_G > E_K$, or cold collapse of the stars in an elongated additional gravitational potential - as likely given the filamentary structure of the dense gas in the ONC - observed at an appropriate angle of inclination to the line of sight could explain the observed stellar radial velocities, which show a difference in kinematics between the northern and southern parts of the cluster (Tobin et al., 2009).

To test the subvirial collapse (what we will refer to as cold collapse in this chapter) picture further, it is necessary to include the time-dependent gravitational potential of the gas, which should also be collapsing along with the stars. In the large-scale "toy model" of the Orion A cloud, Hartmann & Burkert (2007) found that an elongated, rotating, cold collapse model could reproduce the observed morphology of the ^{13}CO gas and formed a dense massive “protocluster” at one end of the cloud. This model, however, had limited resolution and did not include star formation (creation of sink particles). Also motivated in part by the structure of Orion A, Bonnell et al. (2008) simulated star (sink) formation in an initially cylindrical cloud of gas given an initially equilibrium velocity field, which dissipated its kinetic energy and collapsed to form clusters; in this case the evolving gravitational potential of the gas was included. However, Bonnell et al. were focused on the formation and accretion of brown dwarfs and did not focus on the kinematic signatures of the clusters or cloud. Similarly, Bate (2012) presented calculations of cluster formation in a collapsing environment with either a barotropic equation of state or including radiative transfer, but focused mostly on the mass function and relative spatial distribution of low- and high-mass sinks.

In this chapter, we seek to improve upon the work of Proszkow et al. (2009) by allowing the potential of the gas to evolve dynamically. Our simulations are qualitatively similar to that of Bonnell et al. (2008), but we focus on a search for spatial or kinematic properties that could provide observational tests of the sub-virial or cold-collapse picture. The calculations also provide qualitative insights into the difficulties of testing models of star formation from observations at a single epoch in a dynamically-evolving environment. These simulations provide a starting point from which more complex models including magnetic fields and stellar feedback can be developed for comparison with observations.

3.3 Numerical method

To simulate cold collapse of a finite cloud with sink formation, we used the smoothed-particle-hydrodynamics (SPH) code Gadget2 (Springel, 2005). The simulations are evolved on the order of a free fall time, $t_{\rm ff} = 32\pi(G\rho)^{-1/2} = 0.85$ Myr. The simulation is isothermal (T=10K), so dimensions of the cloud, time evolved, and masses can be rescaled with the sound speed.

In Table 3.1, we list the details of initial conditions of runs we have analysed. Based on the idea of the Orion A model in Hartmann & Burkert (2007), we create an initially homogeneous, ellipsoidal triaxial geometry, which can be thought of as a part of a molecular cloud undergoing collapse. As star clusters form in a relatively dynamic interstellar medium, some imparted angular momentum is likely, so we put the cloud initially in uniform rotation, along the most elongated axis, again following Hartmann & Burkert (2007). In addition to runs which serve to replicate the morphology and kinematics of Orion, we include run HR22, an isotropic distribution of gas with no rotation, meant to test which characteristics of infall are generalizable to clusters of arbitrary morphology.

Velocity fluctuations were created through the use of a random decaying supersonic turbulent field of various phases, like that of (Stone et al., 1998), and following the prescriptions of Ballesteros-Paredes et al. (2015), where wave phases scale as $2\pi/L$ for each direction, where L represents the dimensions of a box defined by the principal axes of the initial ellipsoid. Supersonic fluctuations shock the gas, but without constant energy injection, shocks dissipate rapidly. In this context, turbulence serves as a way to create primordial inhomogeneities within a globally collapsing object.

To simulate star formation, we use the sink implementation from Jappsen et al. (2005). While gas particles interact with one another through hydrodynamic and gravitational forces, sinks interact with each other and the particle fluid purely through gravity. Sink formation occurs when a parcel of gas with $\nabla \cdot u < 0$ eaches some threshold critical density within a certain radius. We set the critical density and radius of sink creation to meet SPH resolution requirements where the critical radius is the Jean's length that corresponds to the minimally resolvable mass (Bate & Burkert, 1997). The accretion radii, R_{inner} and R_{outer} are scaled according to the critical radius. All particles within R_{inner} are automatically accreted, where it represents the "physical" boundary of the sink. Particles between R_{inner} and R_{outer} are tested to see if they are gravitationally bound to the sink, (i.e. if $E_{tot} = E_G + E_K < 0$)

Resolution in SPH refers to the minimum resolvable mass, $M_{res} = 2M_{tot}N_{neigh}/N_{tot}$ (Bate & Burkert, 1997) and depends on particle parameters as opposed to spatial parameters like grid size. The high resolution runs have $M_{res} = 0.05M_{\odot}$ and the low resolution runs have $M_{res} = 0.15M_{\odot}$.

Table 3.1: Low and high resolution runs

Run	Mass [$M_\odot$]	N_{tot} [$\times 10^6$]	Dims [pc^3]	Mach #	t_{end} [t_{ff}]	Notes
LR	2320	2	$3\times2\times1$	8	1.1	Low res, ONC like
HR	2320	6	$3\times2\times1$	8	0.9	High res, ONC like
LRb	1160	1	$3\times2\times0.5$	8	1.3	Low res, flattened ONC like
LRc	580	0.5	$3\times2\times0.25$	8	1.8	Low res, flattened ONC like
LRd	580	0.5	$3\times1\times0.5$	2	1.3	Low res, lower Mach #
HR22	1000	6	$1\times1\times1$	8	1.2	Cubical, no rotation (BP15)

Lower resolution runs are suitable for investigating general morphological and kinematic properties. Higher resolution runs are used in situations where better statistics are necessary.

3.4 Results

3.4.1 Morphology of Orion-like runs

Figure 3.1 shows the time evolution and cluster morphology and star formation over 1.1 $t_{\rm ff}$ (0.9 Myr) for an Orion-like geometry (run LR) projected in the XY plane. (From this point on, referenced coordinates are based on those marked in bottom left corner of Figure 3.1) Figure 3.1a shows by the end of $0.4t_{\rm ff}$ (0.3 Myr), the velocity field shocks, dissipates, and leaves behind density inhomogeneities. Uniform rotation along the longest axis contributes to preferential pile up of material at areas of high curvature, creating regions of high gas potential; star formation is an ongoing process throughout, particularly robust in areas where infall helps coalesce inhomogeneities into flows (seen at $0.6t_{\rm ff}$ (0.5 Myr) in Figure 3.1b). At $0.8t_{\rm ff}$ (0.7 Myr), the region of high potential has grown deeper as subclusters have started to merge during cluster assembly (Figure 3.1c). Panel d of Figure 3.1 is the culmination of $1.1t_{\rm ff}$ (0.9 Myr) of evolution; the result is a dense embedded star cluster at one end of a gaseous filament, comparable to the ONC at the end of Orion A.

Runs LRb and LRc are intermediaries between the final three-dimensional Orion-like runs, described above, and the limiting case of a rotating sheet as in the toy model of Hartmann & Burkert (2007). As the ellipsoids become more flattened, we can show that the geometry approaches the

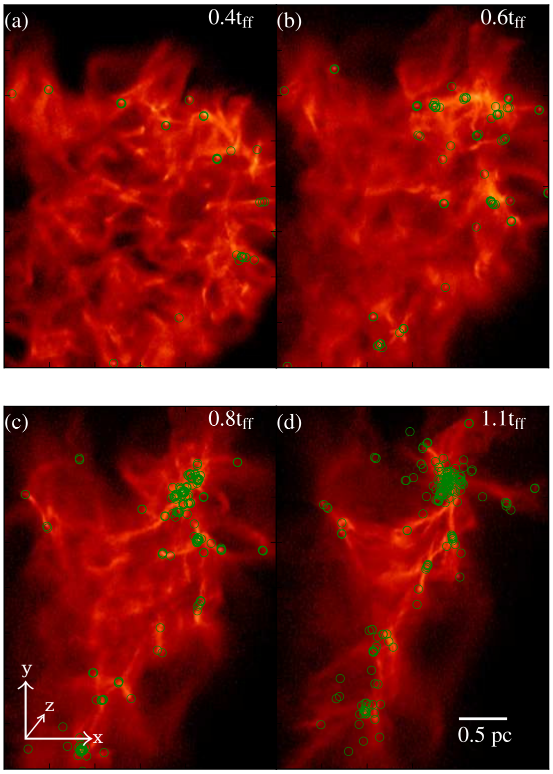

Figure 3.1: Time series evolution in the XY plane of run LR at (a) 0.4, (b) 0.6 (c) 0.8 and (d) 1.1 t_{ff}. Sink positions are shown by empty circle markers. a) Effect of the initial turbulent velocity field b) Density fluctuations remaining after turbulence dies down, start of vigorous star formation c) Sub clusters start to merge together in area of high potential d) End of simulation with formation of newborn cluster along a dense gaseous filament.

simplified case seen in HB07 (Figure 3.2). As such, we demonstrate that the natural outcome of a collapse of a finite rotating object into a filament with a knot of condensation at one end is generalizable to three dimensions.

The cloud and cluster morphology is roughly comparable to that of the simulation of Bonnell et al. (2008). They started with a cylindrical molecular cloud 10 pc in length and 3 pc in diameter, with a linear density gradient from one end of the cylinder to the other. Bonnell et al. also initiated their simulation with a supersonic turbulent velocity field such that the dense end of the cloud was subvirial while the other end was slightly unbound. The main difference between their results and ours is that they formed two large clusters and one significant group rather than the single main cluster we form, possibly due to a stronger focusing effect in our geometry (Burkert & Hartmann, 2004).

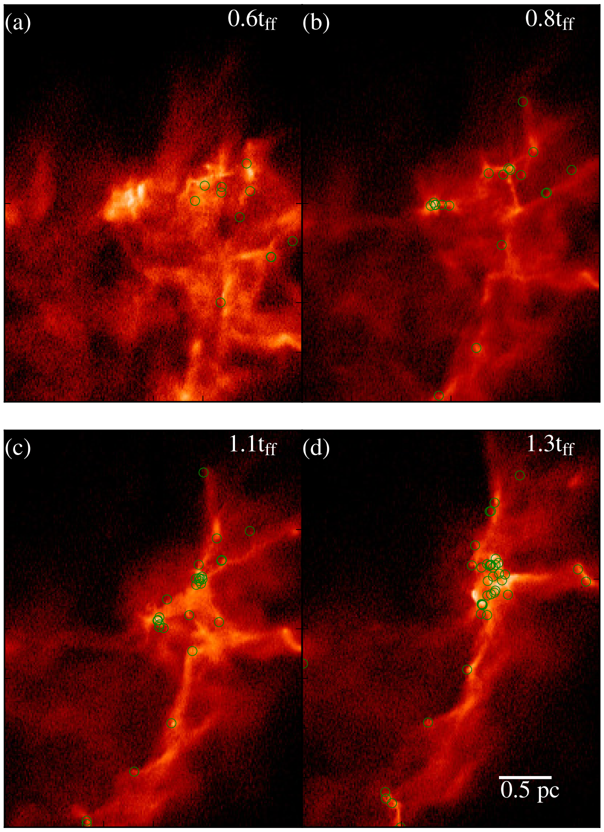

Figure 3.2: Morphological progression of run LRb over time at (a) 0.6 (b) 0.8 (c)1.1 (d) 1.3 $t_{\rm ff}$. a) Formation of density inhomogeneities and subfilaments b) Beginning of noticable infall c) Emergence of filamentary structure d) Gas collapses into final filament with knot of condensation at one end, housing clustered stars.

3.4.2 Dynamic Evolution

3.4.2.1 Gravity - dynamic driver

As gravity is driving cluster formation, it is useful to characterize the evolution of the gravitational potential over time. At early times ($t < 0.5t_{\rm ff}$), the gas potential is dominant, determining the location of the future cluster potential minimum. The increase in densities in this region results in concentrated and star formation centered at $x = 2.23$, $y = 1.89$, $z = 0.0$; this position does not shift as time proceeds. We use this potential minimum as the cluster center in what follows.

In Figure 3.3 we show the contributions of stars and gas to the gravitational potential along a line in the y-direction at the cloud midplane ($z = 0$) and at the $x = 2.23$ value of the cluster center.As star formation and cluster assembly continues, the stellar potential deepens the existing well on small scales close to the future cluster center. The stellar potential does not begin to be significant until later times ($t > 0.8t_{\rm ff}$), when it reaches the same order of magnitude as the potential near the cluster center.

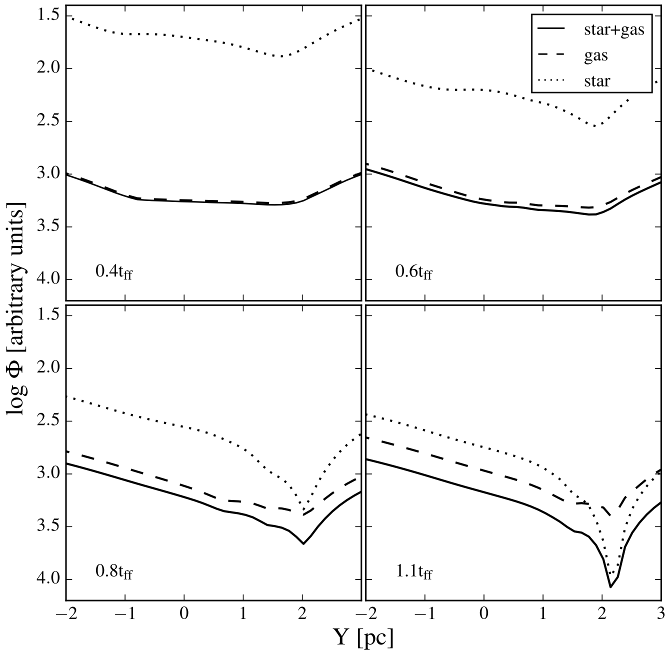

Figure 3.3: Potential wells sliced along the y axis due to stars(dotted), gas(dashed), and both stars and gas (solid) over time shown at 0.4, 0.6, 0.8 and 1.1 $t_{\rm ff}$ shown for run LR

3.4.2.2 Kinematic signatures

Proszkow et al. (2009) showed that radial velocity gradients as seen in the ONC (Tobin et al., 2009) by a model of cold collapse of stars in a fixed spheroidal gravitational potential of gas, viewed from an appropriate angle. In Figure 3.4, we plot position velocity diagrams for the cluster (run HR) and its surrounding region in various projections (XY, ZY, and XZ planes) at $t = 0.9t_{\rm ff}$ (0.71 Myr) for comparison with the Proszkow et al. results.

Proszkow et al. (2009) found that a gradient such as the one in the ONC was only found when viewing the region at an angle to one of the principal axes of the spheroid. Changing the projection from the ZY plane to the XZ plane by tilting the cluster about 60 degrees about the z axis (tilting from panel b to panel c of Figure 3.4) can reproduce a weak velocity difference of 1.0 kms^{-1} between the "north" and "south" regions of the gas (Figure 3.5), smaller than the 2.4 kms^{-1} difference found in Orion (Tobin et al., 2009). This occurs, in part, due to a projection effect achieved by placing regions of the cluster gas and the filament gas in the same plane. To achieve an appreciable gradient, the projection should be in the plane of the initial imparted rotation (i.e. projecting panel a of Figure 3.4 toward panel c does not have the same effect). To that effect, runs without added rotation do not develop a significant gradient.

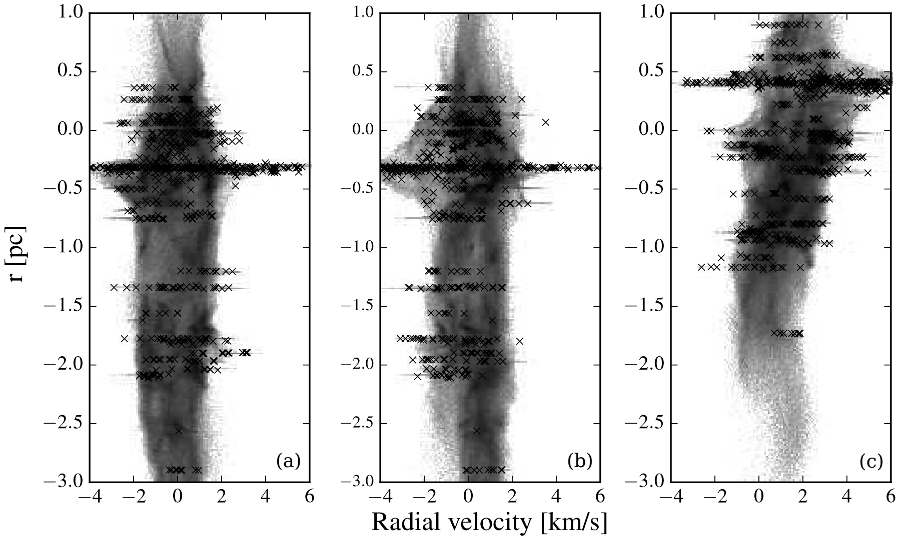

Figure 3.4: Position-radial velocity diagrams for views in (a) the XY plane vs v_z (b) the YZ plane vs v_x (c) the XZ plane vs v_y at $t = 0.9$ff. .

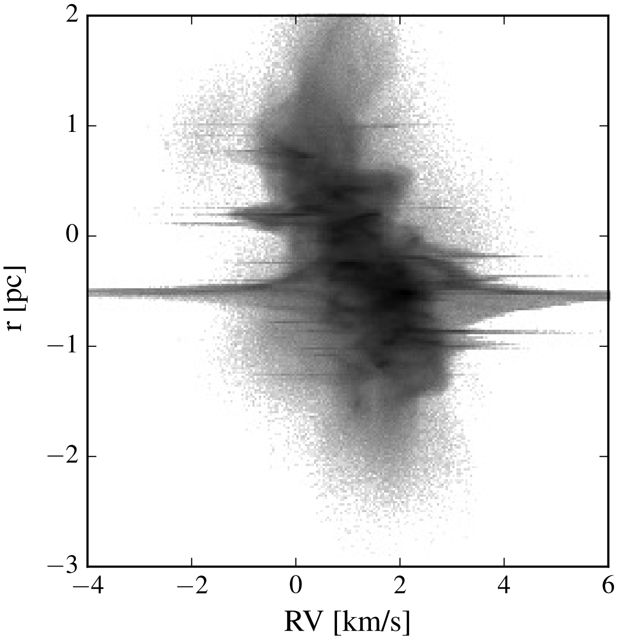

Figure 3.5: Position-radial velocity diagrams plotted for a 60 degree projection of the ZY projection about the z axis (panel b of Figure 3.4). Velocity difference between the north and south is 1.0 kms^{-1}

Earlier in the formation process (t = 0.7 t_{ff}, Figure 3.6), proper motions tend toward the cluster center. The cluster center at this time is characterized by a large amount of gas and some captured stars. While some proper motions visible in Figure 3.6 are clearly directed toward this location, others are less clear as signatures of infall. Even though we know that infall is occurring, it might be difficult to discern at early times. As the gas potential is the driver of cluster evolution, dense gas structure could play an important part in determining the motions of stars during times before massive cluster assembly.

During the final timestep of the simulation (t = 0.9 t_{ff}), proper motions of sinks far outside the cluster follow the global infall dictated by the gas (Figure 3.7a), but within the newborn cluster, infall is (unsurprisingly) difficult to distinguish. In Figure 3.7b, we plot the proper motions of stars within the cluster at the same timestep as Figure 3.6b, shown oriented around the cluster center. Using Figure 3.7, it is evident that infall signatures exist primarily at larger scales, several parsecs outside the cluster. Many of the proper motion vectors do not point directly at the cluster center, due in part to the global angular momentum imparted to the cloud as an initial condition. However,

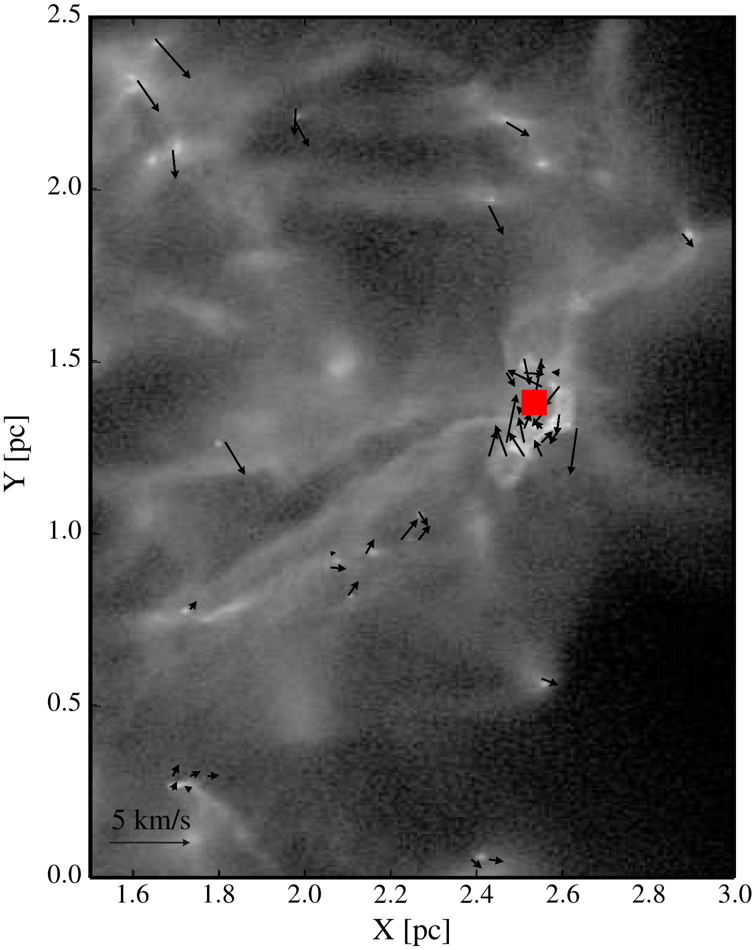

Figure 3.6: Sample proper motions plotted on the large scale at early times ($t = 0.7\mathrm{t_{ff}}$) where proper motions are heading toward the current cluster position (denoted by the red square). Background is gas surface density at those locations.

there is a general, though weak, signal of collapse in that the proper motions shown in the upper half of Figure 3.6, while the proper motions in the lower half are much smaller and oriented much differently (see also Figure 3.7).

There is little evidence of infall when looking at proper motions within the cluster bounds (Figure 3.7, right panel). We can attribute this effect to something like violent relaxation during the collapse where the rapid growth of the stellar potential in the cluster location can induce a rapid relaxation for particles within the cluster bounds. Two body relaxation is not a plausible

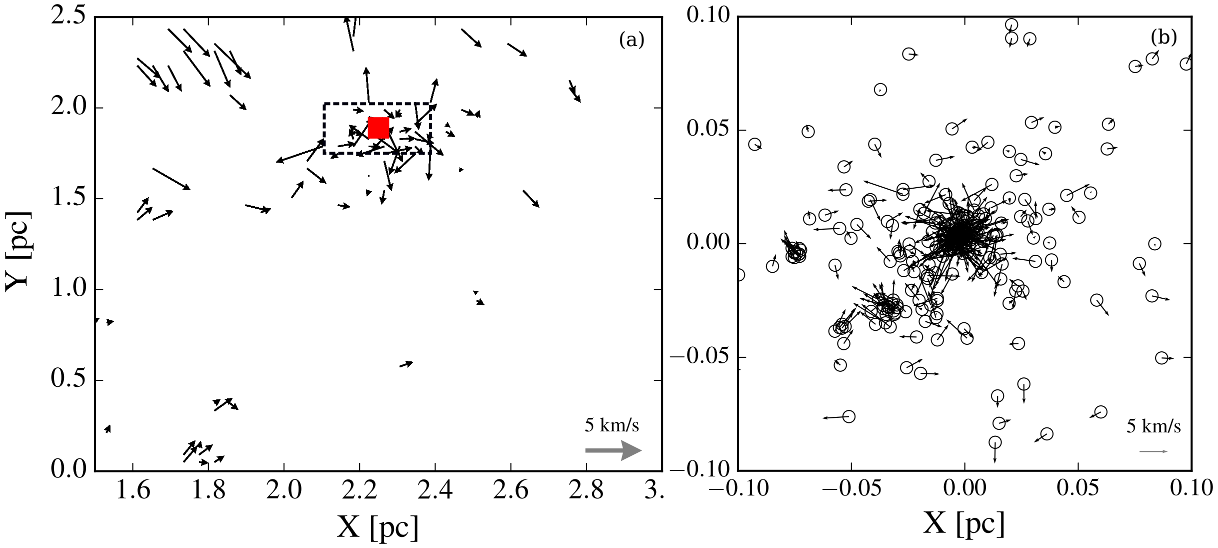

Figure 3.7: Proper motions of stars at t = 0.9 t_{ff}, post cluster assembly (a) at large scales, proper motions are toward the cluster center (b) enlarged view of the dashed rectangle centered at the cluster center.

mechanism to explain the lack of infall signatures as the timescale for a cluster with the parameters matching our model cluster is on the order of a few Myr, much longer than the freefall time and cluster assembly time for the cluster. Due to dynamical processing associated with global collapse, it appears that there exists a time dependent length scale on which infall signatures manifest.

At the end of the simulations, the velocity dispersions of stars within the cluster are nearly isotropic, with values of $3-4\mathrm{kms}^{-1}$, comparable to that observed in the ONC, while the velocity dispersions of the gas of $1-2\mathrm{kms}^{-1}$ are somewhat smaller than ONC values (Tobin et al., 2009; Bally et al., 1987).

Decoupling of the stars from gas increases over time as the growth of the stellar dispersion accelerates due to infall. The velocity distributions of the gas do not change significantly over time, unlike the stellar distribution which widens dramatically over a few fractions of the free-fall time. This effect can be attributable to the infall, where the kinematics of the sink particles in the simulation are much more susceptible to the effects of gravity than the gas particles which can experience damping due to the hydrodynamics.

To more generally investigate the effects of infall on cluster kinematics, we perform the same analysis on run HR22, an initial setup without elongation or rotation. Similar decoupling between stellar and gas velocities as stellar dispersions grow is observed over the formation and evolution.

3.4.3 Substructure

Larger scale infall is responsible for creating the main potential well in which the final cluster forms, while subclusters are created out of the smaller scale primordial density perturbations arising from dissipated shocks made by the initial velocity perturbations. The substructure is initially subvirial, but approaches a virial state as the cluster assembles. We can track cluster assembly by looking at the evolution of substructure over time, from a heavily substructured filamentary gas cloud to a centrally concentrated star cluster.

Various methods have been used to quantify substructure in a star cluster; the Q parameter (Parker & Meyer, 2012; Cartwright & Whitworth, 2004), the two point correlation function(Bastian et al., 2009, TPCF) and its close relative, the mean surface density of companions (MSDC) (Bate, 1998; Larson, 1995). Here we use the TPCF as a proxy for substructure evolution and to track when the cluster begins to assemble into its final distribution. As we are interested in when our final cluster is a smooth power law distribution and do not need to look at multi-scale substructure, the TPCF is an adequate measure of substructure evolution.

We generate a distribution of all possible distances between sink particles, N, over the cluster area, up to 1.5 pc from the cluster center, and compare it to a random uniform distribution, $N_{\rm ref}$, scaled over the same area. We define the TPCF as $N/N_{\rm ref} - 1$ and compute it for various times. When the two point correlation function for a certain timestep reaches zero, the sample and reference distributions become the same. Using the zero point of the TPCF at different timesteps, we quantify the changing scale of structure over time. The zero point denotes at what scale (in pc) the distribution and its corresponding reference begin to match up, or, in this case, what the largest scale is at which non uniform structure exists. In Figure 3.8, the zero point steadily decreases with time, levelling off at the start of cluster assembly, so that structure becomes relegated to smaller and smaller scales as the cluster forms and homogenizes.

We find that the final distribution of stars in the newborn cluster is relatively smooth. The stellar

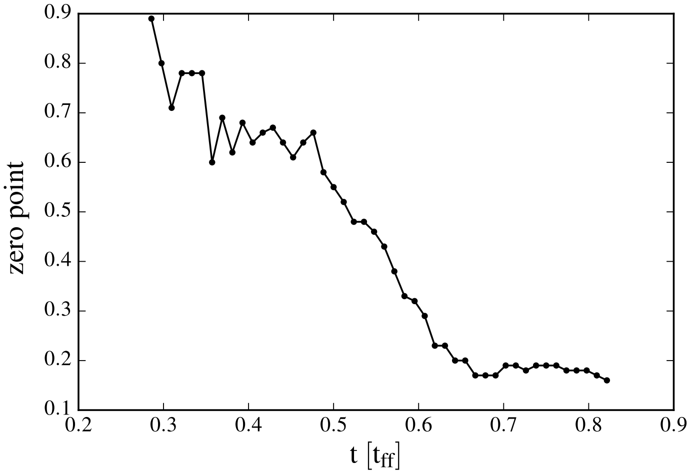

Figure 3.8: Zero point of the TPCF shown as a function of time. As structure gets wiped out, the zero point decreases and levels off.

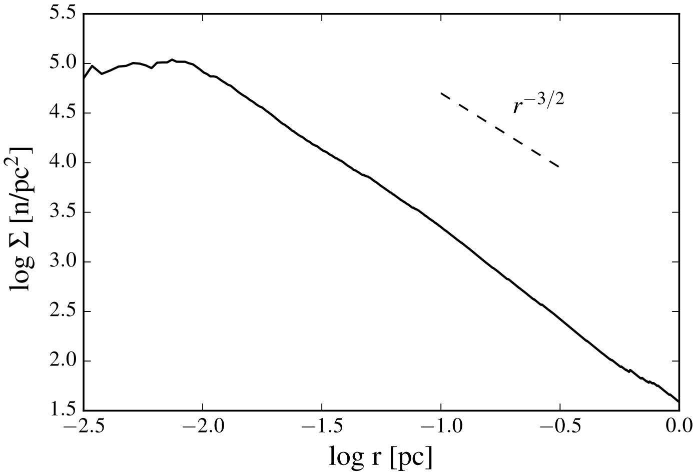

Figure 3.9: Profile of star surface density in the ONC-like cluster within 1 pc for run HR. Dashed line indicates a profile of $\Sigma \propto r^{-3/2}$.

surface density of the local cluster area is comprised of a small inner core decreasing with a power law profile, $\Sigma \propto r^{-3/2}$ (Figure 3.9) consistent with results from other studies that create profiles with $\Sigma \propto r^{\alpha}$, $\alpha < -1$ (Scally & Clarke, 2002) and observations of the ONC (Hillenbrand & Hartmann, 1998; Tan et al., 2006). We find a similarly centrally cored surface density profile for our non-ONC like run, HR22, but with a sharper power law drop-off, $\Sigma \propto r^{-2}$. This difference is likely a product of the different geometries between non-ONC and ONC like runs. Run HR22 experienced a more symmetrical collapse without the influence of rotation or an elongated geometry; its initial geometry is probably more efficient at assembling a cluster as it doesn't contain a filament, making the stellar and gas potential wells deeper at the location of the cluster. In cold collapse scenarios, initial geometry is likely an important factor in determining the final cluster geometry.

3.4.4 The mass function and mass segregation

As Figure 3.1 shows, sinks form first in subclusters along dense filaments and areas of initial gas pileup. Figure 3.10a shows that the (ultimately) more massive sinks form earliest, as we also found in Ballesteros-Paredes et al. (2015). Figure 3.10b shows that on average, larger sinks tend to be more effective accretors. As a result, older sinks have had more time to accrete and gain gravitational influence in an environment becoming more favorable for accretion with time. Previous studies (e.g. Bonnell et al., 2001b, 2008; Ballesteros-Paredes et al., 2015), have found that competitive accretion can reproduce a realistic initial mass function, as we see in our own case for high resolution runs with enough dynamic range (Figure 3.11).

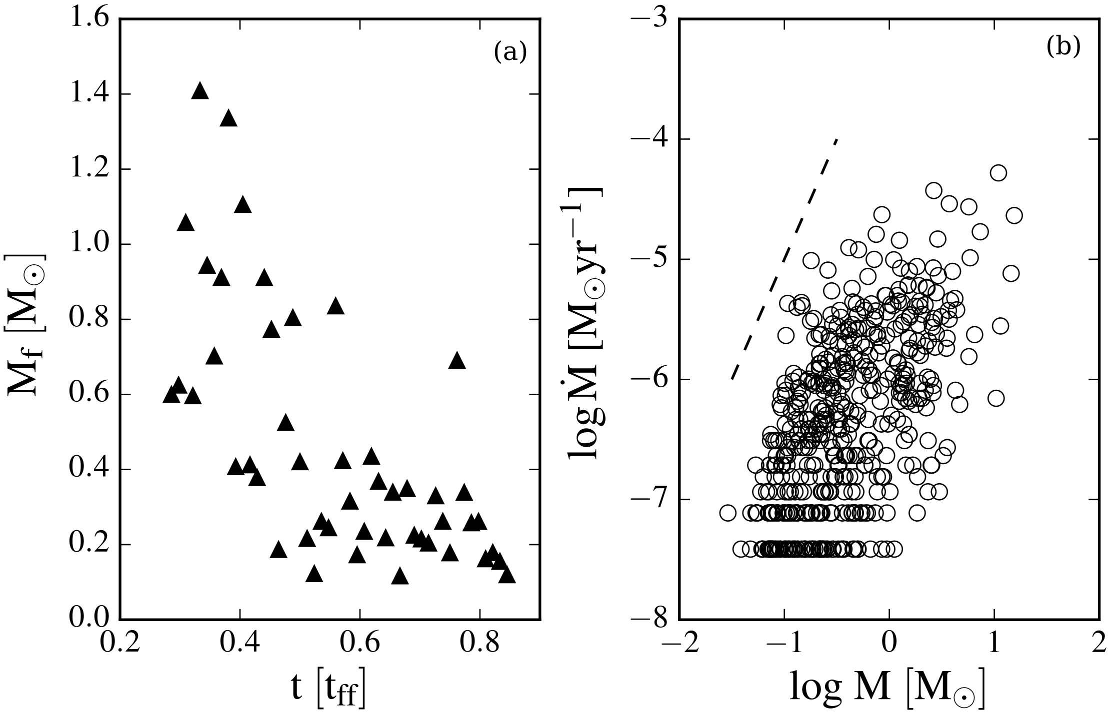

Figure 3.10: (a) Plotted at each time is the average final mass (at $t = 0.9t_{ff}$) of the sinks formed during that timestep. (b) Accretion rate for various mass sinks at 0.9 t_{ff} (run HR). Discrete accretion rates at low values are a result of minimum mass limits for gas particles in the simulation. Dashed line shown has a slope of 2.

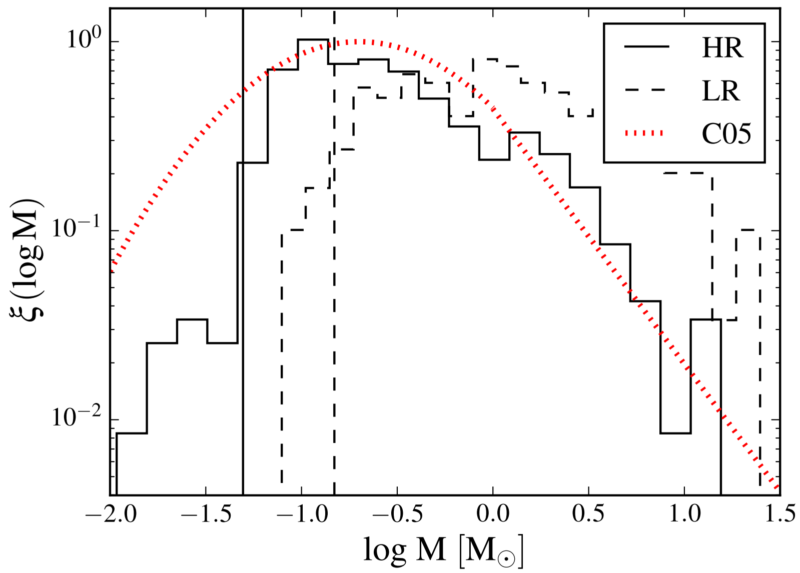

Figure 3.11: Initial mass functions for high resolution (HR-solid) and low resolution (LR-dashed) runs. Plotted against the IMF from Chabrier (2005), normalized uniformly to match numerical IMFs. Locations of the limits of mass resolution are marked by vertical lines. The turnover for higher resolution runs is well defined and develops earlier due to better statistics.

The effects of resolution in this study are seen primarily in the mass function. Figure 3.11 shows the IMF for the low resolution and high resolution runs at the same timestep with vertical lines indicating the minimum resolvable mass for each resolution.Plotted against the empirical model from Chabrier (2005), the high resolution run has a well developed power law tail, however, the location of turnover is an artifact of our choice of mass resolution. With a smaller minimum resolvable mass, the higher resolution runs have a better developed turnover in the IMF shifted toward smaller masses. This leads to more readily produced sinks and overall better statistics. The overall morphology and general kinematics remain unchanged between higher and lower resolutions.

Measurements of Orion's population in Hillenbrand & Hartmann (1998) found clear evidence of mass segregation of the highest mass population, with some evidence for segregation down to lower masses like $1-2M_\odot$. Using the IMF, we divide sinks in the simulation by mass based on different regions of the mass function. Low mass sinks ($M < 0.1M_\odot$) are those smaller in mass than the peak of the mass function. High mass sinks ($M > 2M_\odot$) are those definitively in power law tail of the mass function, with intermediate mass sinks in the region in between. Cumulatively binning the different mass populations in Figure 3.12 on different scales, we find evidence for mass segregation between all three populations.

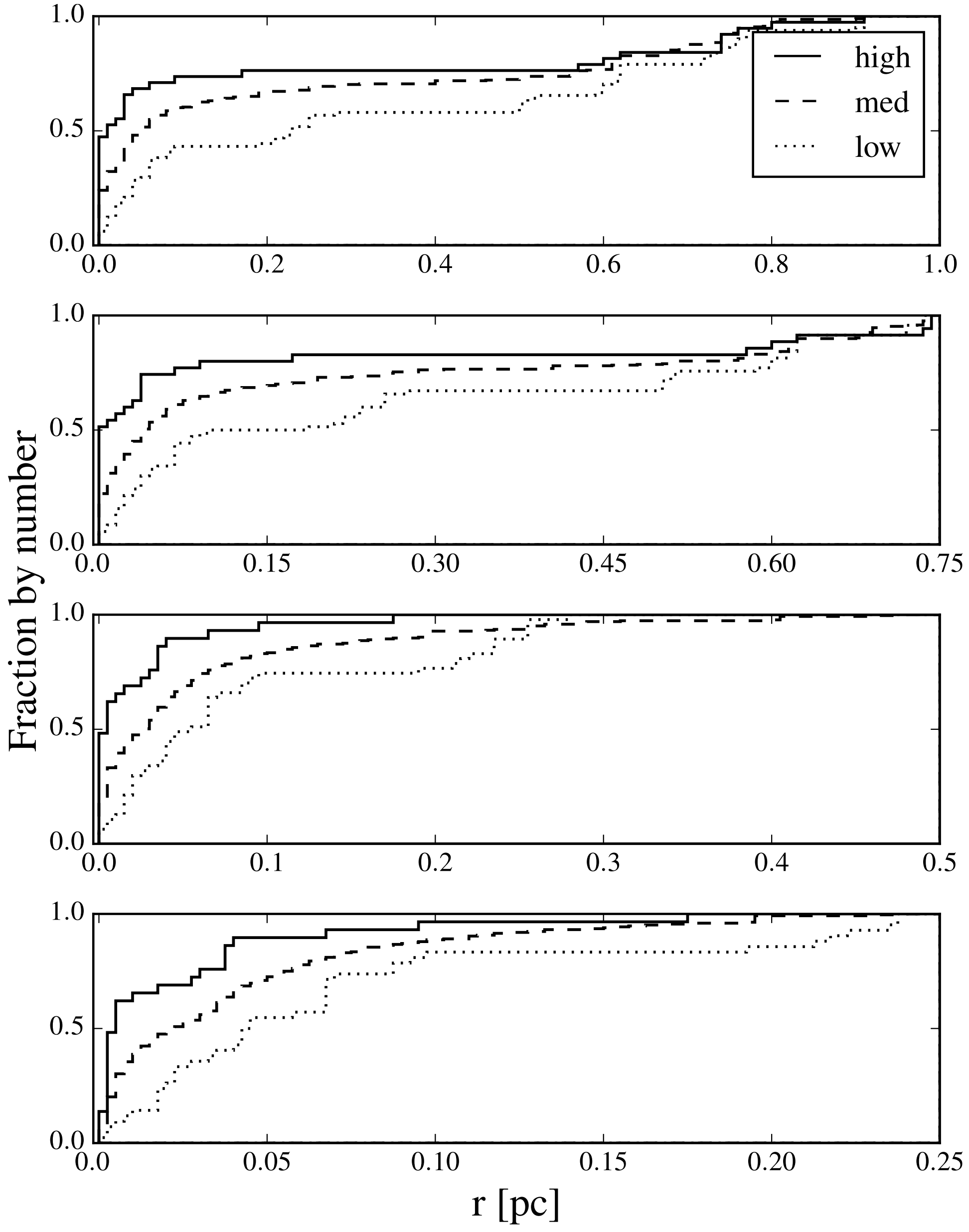

Figure 3.12: Cumulative distributions of stellar populations within (from top to bottom) 1.0, 0.75, 0.5, and 0.25 parsecs from the cluster center. There is clear mass segregation as high mass stars ($M > 2M_{\odot}$) dominate close to the cluster center. Further mass segregation occurs between intermediate ($0.1 < M < 2M_{\odot}$) and low ($M < 0.1M_{\odot}$) mass cluster members as well. (run HR)

3.5 Discussion

3.5.1 Effects of an evolving gas potential

Comparing our results to those of Proszkow et al. (2009), we find some similarities in the types of signatures we can detect in the ONC-like cluster - specifically, that the final cluster is fairly elongated and there exists a radial velocity gradient in the gas between the north and south regions of the cloud. While we see a gradient in Figures 3.4 and 3.5, it is due to projection effects that place the filament and the cluster in the same plane combined with the added initial rotation imparted to the cluster. This emphasizes the importance of projection effects, in agreement with the findings of Proszkow et al. However the importance of the initial rotation component in our simulation can not be discounted in creating these signatures.

The geometry of the gas potential is very similar between our study and that of Proszkow et al. (2009), so significant differences in kinematic signatures can be attributed to the presence of an evolving gas potential and the addition of rotation. The extra dynamical processing of the gas that we have added by introducing a non-static gas potential likely ensures that signatures seen in the static case are short-lived in an evolving potential. In addition, the introduction of small scale fluctuations in the gas imparted by the initial supersonic velocity field, can create additional departures from the static case. However, these departures are probably minor due to the fact that the overall gas potential (which dominates the total) is still relatively smooth.

In a system dominated by infall, we expect to see stellar proper motions pointed toward the center of the cluster. However, as we see in Figures 3.6 and 3.7, even though the simulated cluster is relatively young, obvious signatures of infall no longer exist within bounds of the cluster, and few can be seen on the outskirts of the cluster.

Stellar dispersions grow suddenly and quickly, starting more than halfway through the simulation and growing over a few tenths of a free-fall time.The difference between gas and stellar velocity dispersions is consistent with the study of Foster et al. (2015), who observed that dense cores in NGC 1333 have smaller velocity dispersions than that of the fully formed stars, suggesting that the growth of stellar velocity dispersions over time occurs as stars become dynamically hotter during infall. They concluded this discrepancy between dense gas and stellar dispersions can be explained by global collapse of a gaseous medium of initially subvirial substructure. We find our simulations to be in agreement with the proposed scenario. Similarly, the velocity dispersion of stars in the ONC is larger than that of the associated ^{13}CO gas (Tobin et al., 2009). Time dependence established in observations, like those of NGC 1333 is likely to be erased. The relaxation time for a star cluster with parameters of our final cluster is on the order of a few million years, a loose upper bound that does not take into account gas clearing processes.

3.5.2 What is a bound cluster?

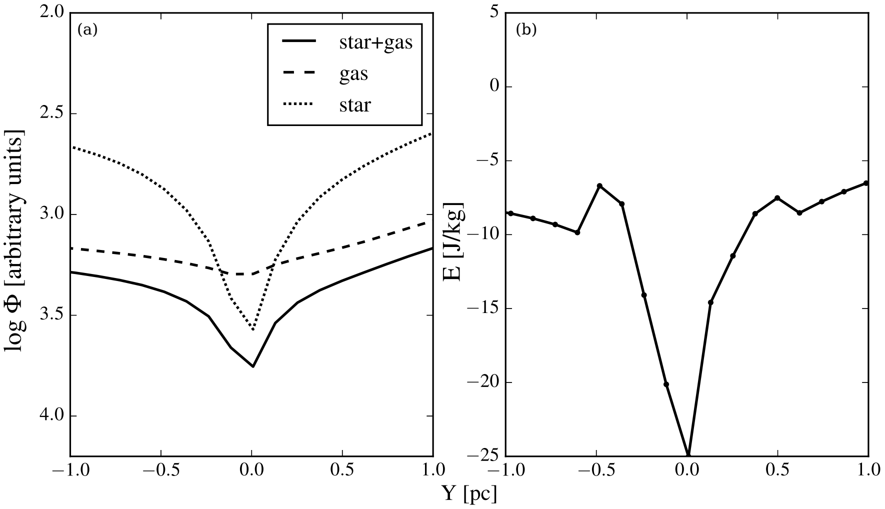

Figure 3.13: Looking at the newborn cluster, we can compare the gravitational potential with the kinetic energy of the stars to look at how bound stars are in regions of the cluster. a) Potential well through the middle of the cluster site, with gas and star potentials shown separately. b) Average energy (E = KE + PE) per unit mass of stars found in the cluster region, where $E < 0$ indicates stars in the region are bound on average.

In Figure 3.13a, we plot a slice of potential through the center of the newborn cluster for run HR (at $t = 0.9t_{\rm ff}$), distinguishing between stellar and gas potential. The stellar potential is responsible for generating the well for a fraction of the cluster region; the gas potential not only deepens the well, but extends its bounds. Figure 3.13b shows the average energy of stars centered around the newborn cluster at 0.9 t_{ff} where stars are firmly bound with $E < 0$. Since the distribution is highly centrally concentrated, most of the stars are within 0.3 pc of the center in the deepest part of the potential well shown in Figure 3.13a.

The virial parameter, $\alpha_{\mathrm{vir}} = 5\sigma^2 R/GM$, is often used to discuss whether a cluster is bound or not . In this study, with full knowledge of the potential, we find the system to be subvirial during formation, only approaching virialized at the end of free fall. This, however, does not ensure the accuracy of the virial parameter. Observational effects and survey design preclude the complete knowledge of the dynamical elements in a system so that without a complete census of the gas in the system, the virial parameter is likely to be misapplied.

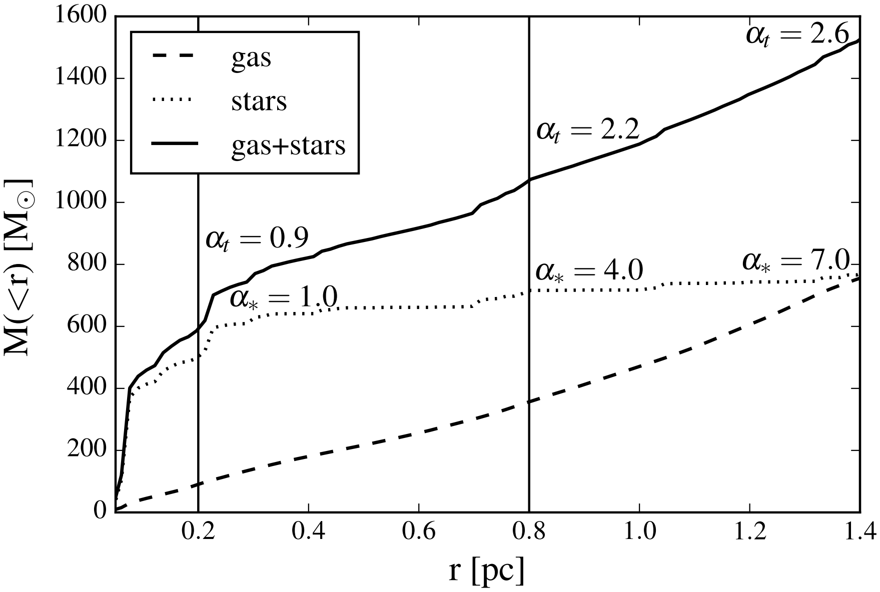

Figure 3.14: Mass enclosed as a function of radius from the cluster center. Labeled at 0.2, 0.8 and 1.4 pc are virial parameters, α_* and α_t at those radii. α_* - virial parameter comparing kinetic energy in stars and only the stellar potential. α_t - virial parameter comparing the kinetic energy in stars with the total potential.

We find that the virial parameter is highly sensitive to observational techniques. Shown in Figure 3.14, the enclosed stellar mass levels off within 0.3 pc, but gas mass grows linearly with radius. Labeled at intervals is the calculated virial parameter using only the stellar potential, α_* and the calculated virial parameter using the total potential, including the contribution of the gas mass, α_t. We see that α_* is roughly virial when taken within the cluster, but supervirial at and beyond the cluster radius. The virial parameter that takes into account the gas potential, but not the kinematic properties of the gas, α_t, is subvirial within the cluster bounds and virial to supervirial at and outside the cluster radius. When calculating a virial parameter that incorporates all the information at our disposal, kinetic and potential energies for both the gas and the stars, we get that the system is subvirial within the cluster and virial outside the cluster bounds. Since observations of star clusters depend on estimates of cluster size and gas content, using a virial parameter like α_* is unlikely to present an accurate picture of a cluster's dynamical state.

3.5.3 Star forming environments

During cold collapse, the environment in the forming cluster/cloud are likely to vary in time and space. Inhomogeneities and filamentary flow create density variations on a variety of spatial scales, while global collapse inherently changes the density of the medium. In assembling the final cluster, stars in this simulation can travel great distances from their birthplaces. We can see in Figure 3.15 and Table 3.2 that some of the most massive stars travel several parsecs to get to their final position within the cluster. These groups are born in separate locales, coming from different environments, and accreting material of various density along the way.

The substantial migration of accreting sinks (stars) is a result of our initial conditions. The initial supersonic velocity fluctuations, although rapidly damped, provided non-linear density perturbations in a distributed environment which then collapsed. Alternatively, one might have started with smaller density perturbations, and arranged collapse to a dense, more filamentary structure in which the sinks would form. In the latter picture, potentially sinks would not travel far from their birthsites, as seen in many non-clustered regions such as Taurus (Hartmann, 2002). The spatial and kinematic relations between local gas and stars might thus provide clues to the level of turbulent structure in the initial cloud. As an example, for run LRd where we've lowered the magnitude of all initial velocity perturbations by a factor of 4, we see less clustering and more filamentary star formation(Figure 3.16). The rotation component remains dominant, but star formation occurs along collapsing filamentary structures within the cloud.

There is evidence for mass segregation in the final cluster, shown in Figure 3.12. However,

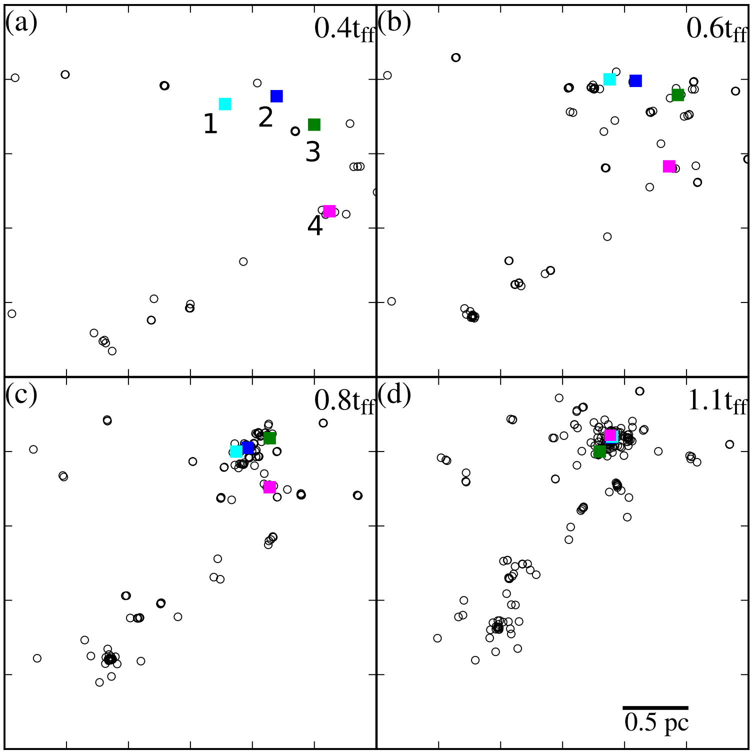

Figure 3.15: Locations of 4 groups (colored squares) of the 10 most massive sinks in the simulations, numbered to correlate with the groups in Table 3.2. a) Sinks form within subclusters that can travel as groups in areas of high curvature spurred on by infall b) Infall starts to bring massive sinks together c) The more massive sinks and their subclusters coalesce to make a newborn cluster d) Newborn cluster houses predominantly the most massive sinks in the center.

Table 3.2: Cumulative distances traveled by massive star groups in Figure 3.15

Group	Distance traveled [pc] at time		
#	0.6 t$_{ff}$	0.8 t$_{ff}$	1.1 t$_{ff}$
1	0.34	0.35	0.65
2	0.23	0.38	0.54
3	0.41	0.90	1.28
4	0.66	1.38	2.10

delineating between a primordial or dynamical origin is difficult as we have shown that stars in a cluster do not have to form anywhere near their final location and can come from different

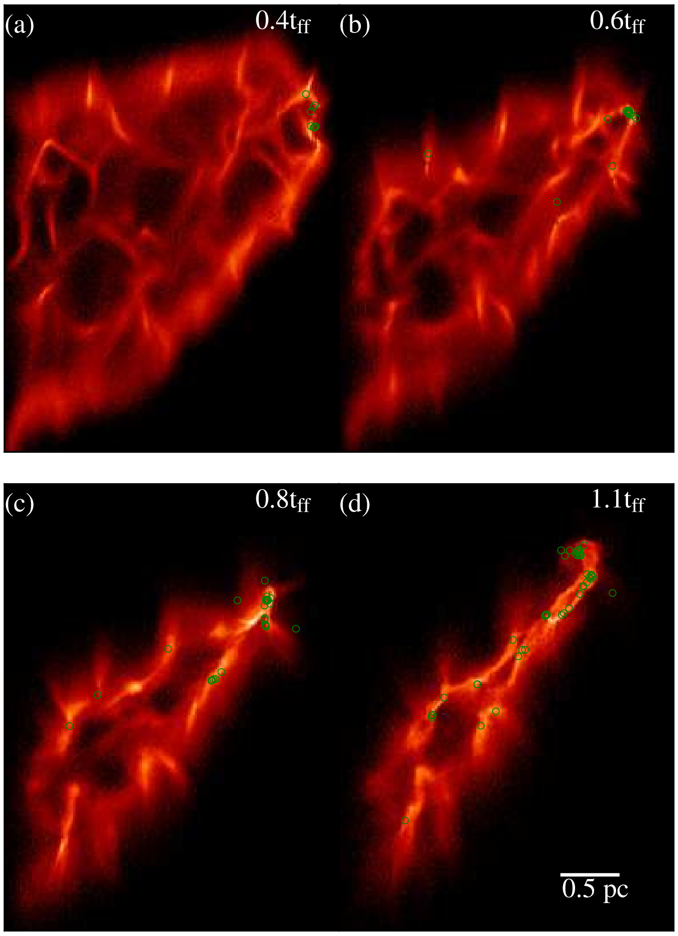

Figure 3.16: Time progression of cluster evolution of simulation where the rotational component is more dominant as the magnitude of initial velocity perturbations has been decreased.

subcluster environments all together. It is possible that because sinks that become the most massive tend to form first they can thus easily become the first real cluster members during assembly while smaller mass stars form closer to the cluster environment as infall condenses the gas. More than likely, mass segregation is a mix of primordial advantages and dynamical processing. Our results show that mass segregation is likely due to the geometrical advantages inherent in the set up. However, it is a look at early mass segregation and later effects of feedback processes that disperse gas could very well change the segregation profile of the cluster as seen in studies of feedback in clusters by Parker et al. (2015).

Another result of the changing landscape that stars form in is that a star forming environment does not simply refer to what is near the cluster, but can refer to varied material that the star forms in and accretes along the way. In fact, we find that, on average, sinks can reach more than half their final mass before even entering the near environs of the cluster (Figure 3.17).

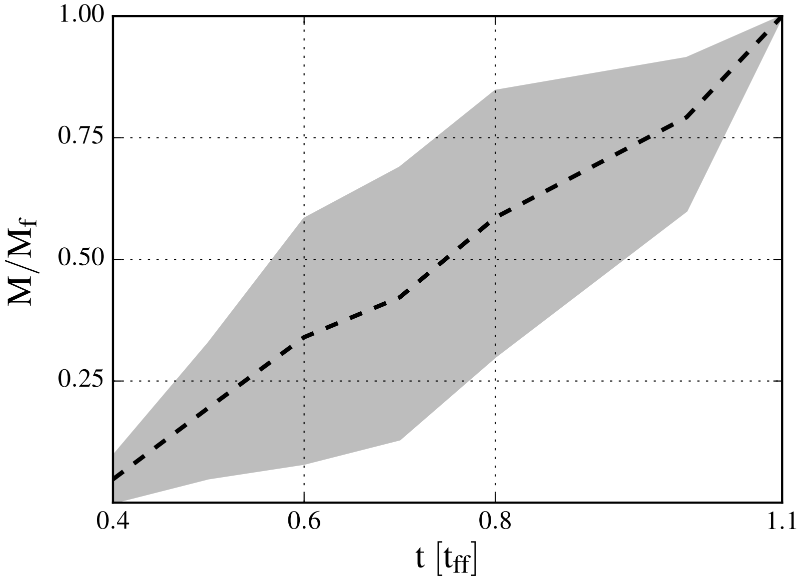

Figure 3.17: Line shows the fraction of mass accreted between the snapshots for a typical sink in Figure 3.15. Shaded region designates upper and lower bounds for sinks in the simulation. Generally, a sink will be over half its final mass by the time it enters the cluster (around t = 0.8 $t_{\rm ff}$ for the low resolution run corresponding to panel c in Figure 3.15).

As a result, measuring star formation efficiency by scaling with local freefall time is misleading as what is meant by “local” is constantly changing for stars traveling many parsecs through different environments on their way to the final cluster. In addition, an evolving gas potential guarantees that the environment in which stars form and accrete can be very different from the cluster that they are observed in. As brought up in Allison et al. (2010), star clusters that we observe only serve as snapshots in a larger and ever shifting story. Attempting to piece together the formation of stars based on the current environment, without thought as to their potential initial conditions, is not likely to be representative of their formation histories.

Around 20-40% of the initial gas mass gets converted to stars at the final stage of the simulation. Using our initial freefall time, the star formation efficiency per freefall time, $\mathrm{SFR_{ff}}$ (defined in Krumholz & Tan (2007)), ranges from 0.2 to 0.36. However, the final cluster environment is, on average, much denser than the inital density. The local free fall time is 0.2 Myr, at most, for near cluster environs. Using this value, the $\mathrm{SFR_{ff}} \lesssim 0.05$, more congruent with estimates made by Krumholz & Tan (2007). As cold collapse will increase density over time, using current conditions makes metrics like the $\mathrm{SFR_{ff}}$ inherently flawed.

Low star formation efficiency measurements have been used in studies (Krumholz & Tan, 2007; Tan et al., 2006, e.g.) to justify initially virialized conditions similar to current cloud conditions. To slow down star formation, mechanisms such as magnetic support and driven turbulence have been invoked. The origin of consistent turbulent driving is still murky, but simulations which inject energy into a system with feedback or turbulence must include gravity, as well, as its effects are demonstrably important.

3.6 Summary

Cold collapse has managed to reproduce general morphological and kinematic features of real life clusters. While neglecting “the kitchen sink”, we demonstrate a proof of concept where much of the cluster formation process can be attributed to gravity. We show that large-scale effects of gravity can naturally produce clusters, even if the near environs of the cluster are dominated by the stars’ gravity.

Subvirial initial conditions and an evolving gas potential do not generate long lived kinematic signatures. To be able to confidently identify infall signatures in an observed cluster one would have to catch the cluster early in its formation process and expand the search outside what one might regularly call its bounds. Outside of ideal conditions, it is difficult to adequately confirm what the initial state of a typical star cluster might be.

Future kinematic studies of nearby open clusters will emerge in the coming years, through radial velocity surveys and large scale efforts like GAIA. With future results used in conjunction with a testable model of cold collapse we can make better predictions of the physics involved in a star forming region. While our simulations do not include all potentially important processes (radiative transfer and feedback, magnetic fields), they serve as a starting point for further studies to investigate effects of those processes on the cold collapse paradigm.

3.7 Acknowledgements

We acknowledge a helpful report from an anonymous referee. JBP and LH acknowledge UNAM-PAPIIT grant number IN103012. Numerical simulations were performed either at Miztli, a 4096 core cluster at DGTIC-UNAM, as well as at University of Michigan HPC center, partially supported by UNAM-PAPIIT grant number IN103012 to JBP. AK would like to acknowledge funding by the Rackham Graduate School at the University of Michigan.

CHAPTER 4

Kinematics and Structure of Star-forming Regions: Insights from Cold Collapse Models

This chapter appears in the Monthly Notices of the Royal Astronomical Society, Volume 473, pp 2372 (Kuznetsova et al., 2018). This work was co-authored with Lee Hartmann and Javier Ballesteros-Paredes. The paper is reproduced here with minor stylistic revisions.

4.1 Abstract

The origin of the observed morphological and kinematic substructure of young star forming regions is a matter of debate. We offer a new analysis of data from simulations of globally gravitationally collapsing clouds of progenitor gas to answer questions about sub-structured star formation in the context of cold collapse. As a specific example, we compare our models to recent radial velocity survey data from the IN-SYNC survey of Orion and new observations of dense gas kinematics, and offer possible interpretations of kinematic and morphological signatures in the region. In the context of our model, we find the frequently-observed hub-filament morphology of the gas naturally arises during gravitational evolution, as well as the dynamically-distinct kinematic substructure of stars. We emphasize that the global and not just the local gravitational potential plays an important role in determining the dynamics of both clusters and filaments.

4.2 Introduction

Star forming regions generally show significant substructure on a variety of scales. Observations of the dust continuum have found that many star forming regions are threaded by networks of filaments, often connected to "hubs" of dense gas and clusters of stars (Myers, 2009; André et al., 2010). Studies of the dense gas in these filaments have identified fibrous substructure by correlating related structures in position-position-velocity space (Hacar et al., 2013). It has become clear that models of star formation must be able to explain the origin and role of filaments, clumps, cores, and related substructures.

Previous work has looked at filament formation as the result of the collisions of turbulent planar shocks (e.g. Mac Low & Klessen, 2004; Federrath, 2016) and even cloud-cloud collisions (Balfour et al., 2015). In this paradigm, the formation of star clusters occurs at the intersections of filaments, where there is enough dense material collected. However, globally collapsing non-spherical mass distributions can also form filaments because of collapse along the shortest axis first. Hartmann & Burkert (2007) applied this idea to a collapsing, rotating elliptical sheet of gas and were able to qualitatively reproduce the structure of the Orion A cloud, in particular the structure of the integral-shaped filament of dense gas running through the Orion Nebula Cluster (ONC).

Multi-object high resolution spectrometers have begun to add to the understanding of star-forming regions with large surveys investigating the kinematic as well as the spatial relationships of the young stars in clusters to the dense gas (Tobin et al., 2009; Kounkel et al., 2016). The most recent of these, from the IN-SYNC near-infrared spectroscopic survey, has provided the clearest analysis yet of kinematic and spatial properties in Orion A (Da Rio et al., 2017). This investigation showed that (a) the stellar radial velocities mostly follow the nearby molecular gas motions; (b) there is a small blueshift of the stars relative to the gas, as originally found in the optical survey of Tobin et al. (2009); (c) several groups exhibit kinematic subclustering, with the Orion ONC showing a smoother velocity structure; and (d) there is evidence that some of the groups may be gravitationally unbound, with the ONC itself possibly expanding. On the other hand, Hacar et al. (2017) infer that the dense gas in the OMC-1 cloud associated with the ONC is gravitationally collapsing, based on observations of N_2H^+.

These new results on gas and stellar kinematics motivated us to perform a new analysis of simulations from Kuznetsova et al. (2015) to characterize the substructure expected from a young star forming region formed by global gravitational collapse. Our simulations assume "fast" star formation, where initial turbulence seeds the cloud with density perturbations; the subsequent evolution is driven by gravity without continued turbulent forcing. While stellar feedback (jets, winds, photoionzation/dissociation) can be important and even dominant once massive stars form, this simplification allows us to identify features which can be explained by gravitational collapse alone. Kuznetsova et al. (2015) found that cold collapse models can naturally produce a cluster over short timescales, but that the rapid dynamical evolution inherent in global gravitational collapse tends to erase obvious kinematic signatures of infall within cluster bounds. In this new analysis, we find that several of the features identified by Da Rio et al. (2017) in Orion A can be explained qualitatively and semi-quantitatively by gravitational driving. Our results are also in good agreement with the inference of gravitational collapse by Hacar et al. (2017).

4.3 Method

We analyse data from a simulation of the sub-virial collapse of a 2320 $M_\odot$ triaxial ellipsoidal shell of molecular gas (run LR from Kuznetsova et al. (2015)) using the smoothed-particle-hydrodynamics (SPH) code Gadget2 (Springel, 2005) with a sink implementation from Jappsen et al. (2005). As in Hartmann & Burkert (2007), the cloud is given some element of rotation along the long axis. Supersonic turbulence was seeded initially with the same prescription as in Ballesteros-Paredes et al. (2015). Because no continued forcing is applied, turbulent velocities quickly damp, leaving behind small-scale density fluctuations which collapse to form sinks while the overall cloud evolves purely under gravity. The run was evolved for 1.1 free-fall times, where $t_{\mathrm{ff}} = 32\pi(G\rho)^{-1/2} = 0.85$ Myr.

To make a comparison between our simulations and the kinematic substructure observed by Da Rio et al. (2017), we use an algorithm based on friends-of-friends in order to correlate substructure spatially and kinematically. Friends-of-friends (FOF) is a clustering algorithm, commonly used for identifying halos in cosmological simulations (Huchra & Geller, 1982), that finds groups of members that are denser than a threshold value. For our dataset, we use the 3-D spatial data to locate groups of sinks in which all members are at a linking length, b, away from one another. We use a linking length that corresponds to an overdensity of $n = 125n_0$, where n_0 is the number density of stars at $t = 1.1t_{\rm ff}$ if they were homogeneously distributed across the initial volume. To ensure that the groups found are a single moving group, i.e. a group with a characteristic mean velocity and a given velocity dispersion, we further refine the spatially identified clusters by first making sure that the distribution in velocity space peaks around a single value. However, we merge groups that both a) could be grouped as one structure with a linking length on the order of the structures' sizes and b) have velocity dispersions larger than their difference in mean velocities. Then, we iterate over all groups with a relaxed linking length criterion and accept new members if the velocities of potential members are within 1 standard deviation of the mean velocity of the group.

Because proper motions are generally not available, similar analyses on observational data must either locate groups by identifying overdensities in position-position-velocity (PPV) space (Da Rio et al., 2017) or by employing an FOF-like scheme in PPV space (Hacar et al., 2013). Da Rio et al. (2017) create a stellar density field by sampling the local density at regular points in PPV space, using the closest n stars and a conversion metric such that 1° corresponds to $4\,\mathrm{km s^{-1}}$. Structures are then identified as local maxima in the field.

While PPV methods identify structures in our simulation that are qualitatively similar to those identified with our 3-D FOF scheme, the group properties are much less robust in the former than the latter, mainly because we have about a factor of ten fewer sink particles than stars with radial velocities in the IN-SYNC survey. Therefore we opt to characterize the substructures from the 3-D kinematically refined FOF scheme.

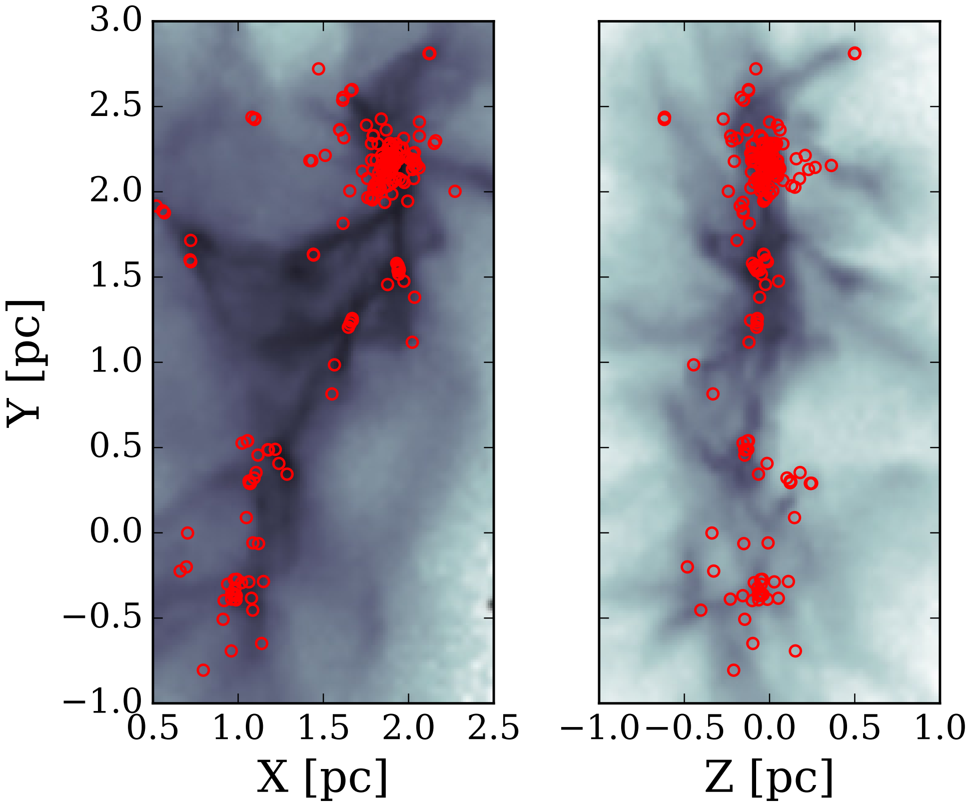

Figure 4.1: Projection of gas density and sink locations (red circles) at $t = 1.1 \mathrm{t_{ff}}$ for a) XY projection, where the line of sight is along the initial rotation axis b) YZ projection, with a line of sight perpendicular to the initial rotation axis. Spatially, stars generally follow the gas.

4.4 Results

At $1.1t_{\mathrm{ff}}$, run LR formed 265 sink particles (about $950M_{\odot}$; the median sink mass was about $1M_{\odot}$). The resulting distribution of gas and sink particles, seen in two distinct projections in Figure 4.1, exhibits the filament and hub morphology seen in many star forming regions (for example, the NH_3 filaments in OMC 1; Wiseman & Ho (1998); see also Teixeira et al. (2006), Peretto et al. (2014)). The projections vary due to the preferential direction of the angular momentum that was initially injected into the system. The left (XY) projection has the line of sight along the initial rotation axis so that all rotation is in the plane of the image, while the right (YZ) projection's line of sight is perpendicular to the rotation axis.

The global structure of gas and sinks is qualitatively similar to that of Orion A (e.g., Figure 1 of Da Rio et al., 2017). This is a reflection of the in intial geometry of the cloud, with the ellipsoidal shape resulting in forming a filament and the concentration of gas and stars resulting from gravitational focusing near the closed end of the ellipse (e.g., Hartmann & Burkert, 2007). However, it is the action of gravity that creates these global structures out of an initially smooth distribution, with the sinks and groups forming from gravitational collapse of the substructure introduced by the random initial velocity perturbations.

The position-radial velocity diagrams for the two projections shown in Figure 4.2 again show a qualitative resemblance to the observations of Orion A (Da Rio et al., 2017, Figure 1 of), with larger velocity dispersions where groups of sinks (stars) are present, particularly in the major group at $Y \sim 2.3$ pc. These velocity dispersions are simply the result of gravitational acceleration as the density concentrations collapse. In addition, the gas shows V-shaped velocity gradients centered on the ONC-like main cluster, as observed in OMC-1 by Hacar et al. (2017) (see §4). The main difference between the qualitative behavior of our simulation and the observations of Orion A is that our simulation does not show as large overall velocity gradient from top to bottom.

The optical radial velocity survey of Tobin et al. (2009) found that while the stars mostly follow the motions of the dense (^{13}CO) gas, there is a broader wing of members with more blueshifted velocities. This issue was reinvestigated by Da Rio et al. (2017) using their near-infrared radial

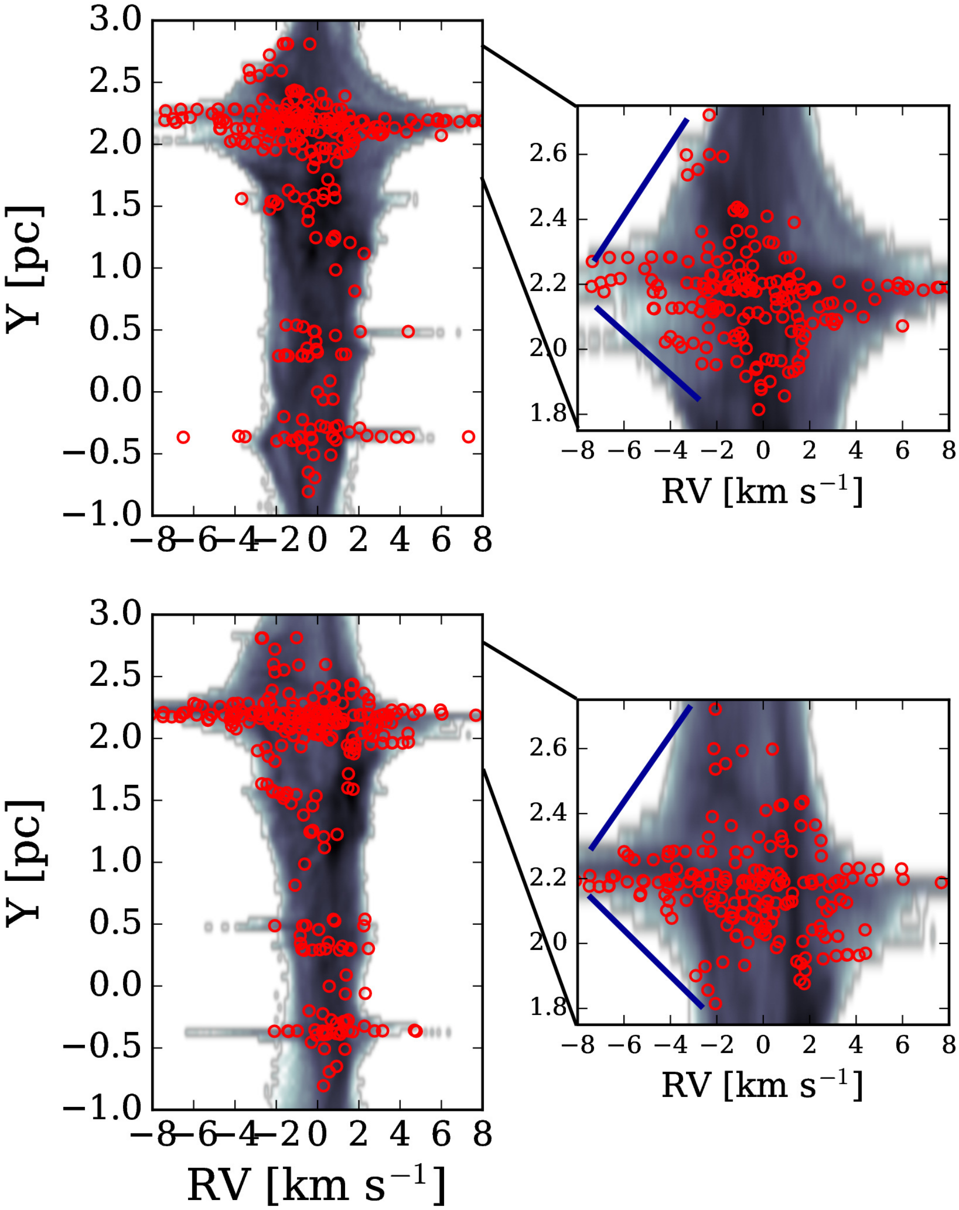

Figure 4.2: Position-velocity diagrams for the gas and sinks (red circles) at $t = 1.1\mathrm{t_{ff}}$ for XY projection (top row), where the line of sight is along the initial rotation axis. The inset is a zoomed in view, annotating the velocity gradients along the gas in the hub cluster region which are on the order of 6km s^{-1}pc^{-1}.The YZ projection (bottom row) has a line of sight perpendicular to the initial rotation axis. The inset shows these velocity gradients are $4-7$km s^{-1}pc^{-1}.

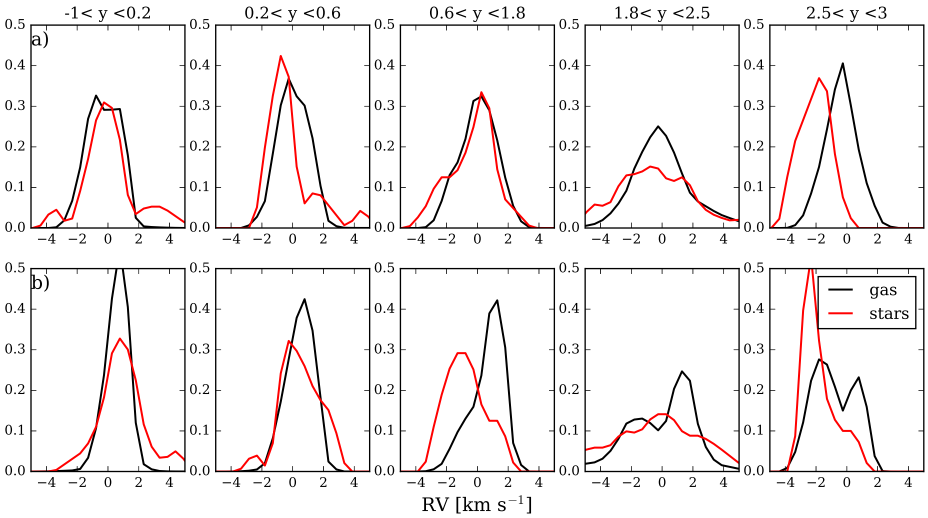

Figure 4.3: Probability density functions of radial velocities for the stars and gas, taken in slices perpendicular to the long axis, shown for two different projections: a) XY (top row) and b) YZ (bottom row). Each column corresponds to a slice at a position along the long axis of the filament containing a grouping of stars. The first 3 columns are populations of stars along the south end of filament, while the 4th column is the slice of the main ONC-like hub cluster region. The last column is a smaller sub cluster region north of the main cluster.

velocity measurements, and thus with a sample less affected by extinction. They similarly found a blue offset due to an asymmetry in the stellar velocity distribution with respect to the CO emission. To explore our simulation in this respect, we constructed probability density distributions of velocities in slices perpendicular to the main filament at different Y positions, as in Figure 4 of Da Rio et al. (2017). Figure 4.3 shows that, as expected, most of the sinks (stars) follow the gas, although in some projections and certain positions we find a small (1 - 2 $\mathrm{km\,s^{-1}}$) blueshift. It is not obvious that this shifted population is simply that of a broad wing, although this conclusion is tentative given our small number statistics. The origin of the blueshift is not clear, but it may be a result of the initial rotation of the cloud, given that it is more evident in the YZ projection.

The velocity dispersions of stellar groups are also larger than that of the gas, as also seen in Orion A (e.g., Figure 10 in Da Rio et al., 2017). This is especially evident in groups at smaller Y. The larger stellar dispersions are the result of close interactions between sinks.

We identify kinematic substructure by the method described in §2 at different times during the simulation. At early times, the substructures are representative of the early subclusters, collapsed cores along the two main filaments which form by early collapse along the boundary of the ellipsoid. During the course of collapse, kinematic substructures grow larger via two mechanisms: by the addition of stars forming within their potential wells and by merging with other substructures. By the end of the simulation at $t = 1.1\mathrm{t}_{\mathrm{ff}}$, substructures in the stars trace out the main cluster and the densest parts of the largest filament (Figure 4.4). The resulting groups, which are the product of clustering due to gravitational interactions in the subvirial cloud, qualitatively represent the PPV groups in Orion A identified by Da Rio et al. (2017) (their Figure 7).

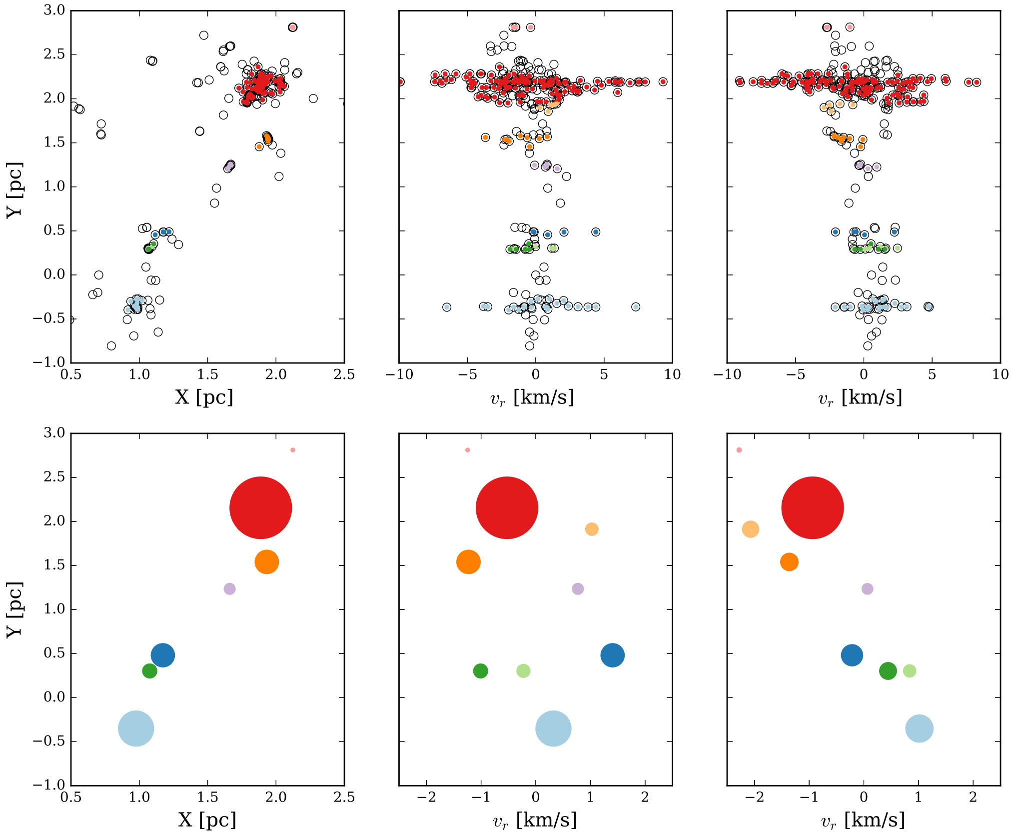

Figure 4.4: Kinematic substructure identified by FOF at $t = 1.1\mathrm{t}_{\mathrm{ff}}$. The ONC-like cluster is the largest group with N = 128 members out of N = 265 total stars. Top row: position and position-velocity diagrams for individual stars. Colored circles represent stars that have been assigned to groups. Bottom row: position and position-velocity diagrams for stellar substructures. Circles are centered around the mean velocity of the identified structures and their sizes correspond to their relative projected areas in position-position-velocity space. The middle column is the position-velocity diagram in the XY projection and the rightmost column is the YZ projection.

4.5 Discussion

In the context of cold collapse, we find that filaments represent bound structures that can form contemporaneously with other structures of high stellar density. While Burkert & Hartmann (2004) have shown that gravitational collapse tends occur along the shortest dimension first, proceeding from cloud to sheet to filaments to cores, gravitational collapse also amplifies any anisotropies, meaning this process happens at a multitude of scales and speeds such that all of these structures form at similar times. Gravitational focussing can create a gravitational potential minimum at locations of high curvature, such that, unlike in Myers (2009), the creation of both a hub and filaments does not require a spherical overdensity in the location of the hub. This also means that the familiar hub-filament paradigm does not necessitate that filaments form first or even that filaments form the hub by feeding it material, although flow along filaments can occur as a result of the hub usually representing a potential minimum, like rivers flowing downstream into the ocean.

While the parameters of our simulation were chosen to obtain an overall morphology akin to that of Orion A, there was no intention of producing an exact correspondence. The simulations only incorporate two forces: gravity and pressure gradients so that the simulation can be rescaled with length, mass, and time units such that $L^3M^{-1}T^{-2} =$ constant. While the precise value of the sound speed is not important since the cloud is highly subvirial thermally, a rescaling of the sound speed by $(M/L)^{1/2}$ or equivalently L/T keeps the ratio of the sound crossing time to the free-fall time the same, maintaining the relative importance of pressure to gravity.

Because the proportion of mass in our main cluster is larger relative to the entire cloud than the ONC is to Orion A, a single rescaling is not possible to address the entire region. However, the gravitational potential in the main cluster region at the end of the simulation is much deeper than the global cloud (Figure 3 of Kuznetsova et al. (2015)), so to first order one can treat the cluster dynamics separately from the large scale cloud structure.

At the end of the simulation, the main cluster has a mass of about 500 $M_\odot$ (dominated by stars/sinks) within a radius of about 0.2 pc, Kuznetsova et al. (see Figure 14 in 2015). From Figure 4.3, the average 1-D velocity dispersion of stars within 0.2 pc of the cluster center is 2.7

km s^{-1}, ranging between 2.2 and 3.2 km s^{-1}. These velocity dispersions are roughly "virial", consistent with the 1-D estimate assuming isotropic motions $v \sim 3^{-1/2}\sqrt{2GM/R} \sim 2.7$ km s^{-1}.

To compare our results to the observed velocity dispersion of the ONC $\sim$ 2- 2.5 km s^{-1} (Jones & Walker, 1988; Tobin et al., 2009; Da Rio et al., 2017) we need to scale the mass and radius. The ONC has a mass of $\sim 2000 M_{\odot}$ within a radius of 2 pc (Hillenbrand & Hartmann, 1998) in stars alone.The mass in gas within the same region is uncertain, but (Hillenbrand & Hartmann, 1998) argue that it might be as large as twice the mass in stars. If we adopt a total ONC region mass of 6000 $M_{\odot}$, we would need to scale up the cluster region mass by a factors 12 and the radius by a factor of 10 from 0.2 to 2 pc, increasing our velocity dispersion from ~ 2.7 to ~ 3 km s^{-1}. This is easily within the uncertainties; if we instead use the virial mass estimated by (Hillenbrand & Hartmann, 1998) of 4500 $M_{\odot}$, the resulting scaled velocity dispersion is 2.5 km s^{-1}.

We qualitatively observe the evidence of gravitational acceleration toward the cluster center as V-shaped radial velocity gradients centered around the hub cluster (Figure 4.2), similarly to the $5-7$km s^{-1}pc^{-1} V-structure seen in N_2H^+ emission from OMC-1 by Hacar et al. (2017). The simulation's symmetric collapse produces two V-shaped features, in the red and the blue, compared to the OMC's one sided feature. A rescaling according to size and mass scales of the ONC can produce velocity gradients consistent with those in OMC-1, but direct comparisons are difficult to do as it depends on the inclination of the filament to the line of sight, which is highly uncertain.

The kinematics of the subclusters that form along the filament at the same time as the early natal cluster stars present an interesting opportunity to study the dynamics of star formation without the dynamical processing that occurs in the populated main cluster erasing kinematic signatures. Recent studies of the *APOGEE* data for Orion have identified kinematic substructures (Da Rio et al., 2017; Hacar et al., 2016). While Da Rio et al. (2017) interpret the substructures they find along the filament to have inherited the properties of their natal turbulence, Hacar et al. (2016) similarly posit that these stellar groupings inherit the dynamical properties of their natal gas clumps. However, we show in the context of our simulations that since these substructures clearly accrete both stars and other subclusters of stars, any signature of natal turbulence will be short lived. The properties of these structures are more likely determined by the material they accrete; the initial turbulent fluctuations serve only as seeds for the structures to develop. As discussed in detail in Kuznetsova et al. (2015), it is possible for initial infall signatures like proper motions to be preserved by the substructures in the filament. With Gaia and complementary radial velocity studies in the optical and IR (e.g. Tobin et al., 2009; Kounkel et al., 2016), these filament populations can become an important testing ground for star formation theories.

As stellar substructures grow in membership and mass, their velocity dispersions also grow, outpacing the velocity dispersion of the gas and mirroring the global trend identified in Kuznetsova et al. (2015) for stellar velocity dispersions to be higher than that of the gas. Massive substructures from earlier timesteps in the simulation have smaller dispersions than massive substructures at later times. This further suggests that gravitational interactions between stars during accretion of members could play a role in determining the dynamics of stellar substructures.

Da Rio et al. (2017) showed that in the southern region of Orion A (L 1641), the velocity dispersion predicted from the estimated gravitational potential of the broad (several pc-wide) filament predicted a velocity dispersion of only about $0.65\,\mathrm{km\,s^{-1}}$, much smaller than the observed dispersions of gas and stars which are on the order of $2.5\,\mathrm{km\,s^{-1}}$. They concluded that this region could be gravitationally unbound. However, the mass to length ratio is a metric reserved for narrow cylindrical filaments, which is not true of either simulated filament or Orion A, which are both 3D objects. While the velocity dispersions of the simulation substructures also exceed the 1-D filament prediction, the groups are, in fact, bound. The filamentary condition for virial equilibrium does not account for the total mass in gas present deepening the global gravitational potential or for the mass in stars present in the groups, which dominate the local gravitational potential of the sub-clusters.

While the sinks (stars) constitute only a small fraction of the gas mass in the region, they are much more centrally concentrated than the gas, and so increase the magnitude of the *local* gravitational potential over that of the gas (see Kuznetsova et al., 2015).

In embedded systems such as Orion, taking stock of gas mass for properly diagnosing kinematics becomes especially important. In Kuznetsova et al. (2015), we show that without complete information about the gas content, the virial parameter, $\alpha = 5\sigma^2 R/GM$, for a gas rich cluster is at best an upper limit for which completely bound systems can appear to be supervirial. The virial parameter assumes that the cluster has the gravitational potential of a uniform sphere and exhibits isotropic motion, neither of which are obviously applicable in Orion, nor in our simulation. We show in Kuznetsova et al. (2015) that calculating a virial parameter for the cluster in the simulation can yield a range of values from 0.9 to 4.0, depending on how much gas mass is accounted for and how the bounds of the cluster are defined. Thus, the virial parameter of 1.8 from Da Rio et al. (2017) could easily result from underestimating the mass of the system.

We have shown that stellar groups can appear red or blue shifted from the bulk motions of the gas, depending on the projection used (Figure 4.3). It is also evident from Figure 4.3 that projection effects can hide or display the presence of rotation. The projection dominated by the rotational component (YZ) shows the clear development of a double peaked profile from north to south along the filament. This projection also most closely matches the observed velocity gradient of substructures in Orion A shown in Da Rio et al. (2017), but attributing that phenomenon to angular momentum injection at large scales is difficult. The gas in the Northern end of Orion A has likely been disturbed by the formation of super bubbles (Bally, 2008), corrupting velocity information that could definitively identify large scale rotation. However, velocity gradients themselves are susceptible to projection effects where the projection of filament populations along the line of sight to the cluster can produce a radial velocity gradient in stars and gas along the filament axis (Kuznetsova et al., 2015). Even without projection, the subcluster populations along the filament can be expected to have different velocities from the hub cluster simply because they are kinematically different, having had a separate dynamical history than stars that end up processed by the hub cluster.

We emphasize that the only way in which we ”seeded” the initial condition in a way to produce a desired outcome was in the shape of the initial ellipsoidal cloud, which provided an axis of symmetry to produce somewhat filamentary structure, along with a smaller radius of curvature at one end which the simulations of Burkert & Hartmann (2004) and Hartmann & Burkert (2007) showed would produce a focal point to form a massive region and hence a large cluster. The other groups of stars arose from the density perturbations resulting from the random initial velocity fluctuations.

The results of this simple simulation illustrate the power of gravity to naturally produce groups and clusters of stars. This is in line with our previous study in which we argued that gravitational focusing effects are responsible for producing the observed power-law mass distribution of young clusters (Kuznetsova et al., 2017).

4.6 Summary

We perform a new analysis of simulation datasets from Kuznetsova et al. (2015) to identify and characterize the type of substructures that can be expected in a star forming region created by the global gravitational collapse of molecular gas. We find that substructure such as filaments and sub cluster forms contemporaneously with many of the stars that end up in the main star cluster. These structures could be useful probes of star cluster formation at early times and complete kinematic information could provide a detailed test of star formation theories.

In addition, we examine and compare the kinematic features identified in Orion A by Da Rio et al. (2017) to those we can identify in our simulations. We find that features, such as the difference between stellar and gas velocity dispersions in groups of stars, are reproduced by our simulations. Disparities between the kinematics of filament and cluster stars could be due to rotation or manifest primarily due to projection and/or extinction effects, which should always be considered when dealing with anisotropic dense structures. Finally, we find a V-shaped structure in the gas around our most massive cluster very similar to that observed by Hacar et al. (2017) in the ONC region, supporting their interpretation of collapse.

Our simple cold-collapse model driven entirely by gravity can easily produce the familiar hub-filament morphology such that turbulence is not required to play a leading role in forming substructures. While simulations including many other effects, such as magnetic fields and stellar feedback, will ultimately be required to fully understand the structure of star-forming regions such as Orion, our calculations focusing on the effects of gravity can provide an initial basis for more complicated simulations in the future.

4.7 Acknowledgements

AK acknowledges funding from the Rackham Graduate School of the University of Michigan and from NASA grant NNX16AB46G. J.B.-P. acknowledges UNAM-PAPIIT grant number IN110816, and to UNAM's DGAPA-PASPA Sabbatical program. He also is indebted to the Alexander von Humboldt Stiftung for its invaluable support. Numerical simulations were performed at the Miztli cluster at DGTIC-UNAM.

CHAPTER 5

The Role of Gravity in Producing Power-Law Mass Functions

This chapter appears in the Astrophysical Journal, Volume 868, pp 50 (Kuznetsova et al., 2018). This work was co-authored with Lee Hartmann, Fabian Heitsch, and Javier Ballesteros-Paredes. The paper is reproduced here with minor stylistic revisions.

5.1 Abstract

Numerical simulations of star formation have found that a power-law mass function can develop at high masses. In a previous paper, we employed isothermal simulations which created large numbers of sinks over a large range in masses to show that the power law exponent of the mass function, $dN/d\log M \propto M^{\Gamma}$, asymptotically and accurately approaches $\Gamma = -1$. Simple analytic models show that such a power law can develop if the mass accretion rate $\dot{M} \propto M^2$, as in Bondi-Hoyle accretion; however, the sink mass accretion rates in the simulations show significant departures from this relation. In this chapter we show that the expected accretion rate dependence is more closely realized provided the gravitating mass is taken to be the sum of the sink mass and the mass in the near environment. This reconciles the observed mass functions with the accretion rate dependencies, and demonstrates that power-law upper mass functions are essentially the result of gravitational focusing, a mechanism present in, for example, the competitive accretion model.

5.2 Introduction

Many analytic arguments and hydrodynamic simulations over the past few decades have been employed in attempts to understand the origin of the stellar initial mass function (IMF) (see Offner et al., 2014, for a recent review). In recent years, most such efforts have been numerical because of the complexity of the environments in which stars form. Many simulations now have managed to produce sink particle mass functions which are qualitatively similar to the IMF, with a peak around $0.2\mathrm{M}_{\odot}$ and a width in mass consistent with observational estimates such as the Chabrier (2005) IMF (e.g., Bate 2012; Krumholz et al. 2012; Lee & Hennebelle 2018; Haugbølle et al. 2018).

Because these simulations involve complex, turbulent regions with varying levels of detailed physics, the results have been explained in qualitatively different ways. Some authors emphasize the importance of density and velocity perturbations in local environments (e.g., Padoan & Nordlund, 2002), while others emphasize accretion from global scales ("competitive accretion"; Bonnell et al., 2001a,b; Bate et al., 2003). In addition, although most investigators emphasize the importance of thermal physics to establishing the peak of the IMF (Jappsen et al., 2005; Bate, 2012), this has been contested by Haugbølle et al. (2018), who argue that isothermal MHD turbulence alone is sufficient.

While simulations differ in assumptions about equations of state, magnetic fields, stellar feedback, driven or decaying turbulence, etc., all ultimately rely on gravitational collapse to form stars. This has led us to perform investigations which isolate the effects of gravity in star and star cluster formation with a minimum of additional complications. In Ballesteros-Paredes et al. (2015) (BP15) we presented isothermal smooth-particle hydrodynamic (SPH) simulations with decaying turbulence and sink particle formation. With this limited set of physics, we were able to produce enough sinks to clearly show the development of a power-law distribution in masses. While many other simulations have shown indications of power-law behavior at large masses (e.g., Figure 5 of Jappsen et al., 2005), our simulations covered a sufficiently large dynamic range to allow a statistically robust estimate of the IMF slope of $dN/d\log M = M^{\Gamma}$, with $\Gamma = -1 \pm 0.1$.

To further simplify the physics involved and focus on the effects of gravity, in Kuznetsova et al. (2017) we showed that pure N-body simulations with an initial set of velocity fluctuations also produce power-law mass functions of similar slopes. Since the classical Salpeter value of $\Gamma = -1.35$ for the stellar IMF is only slightly steeper, and as the young cluster mass function is estimated to be $\Gamma \sim -1$ (Lada & Lada, 2003; Fall & Chandar, 2012), we have argued that gravitational physics is dominant in collecting the mass that forms both high-mass stars and star clusters.

The robust value of $\Gamma = -1$ found in these simulations led us to suggest that something like Bondi-Hoyle-Littleton (BHL) accretion (Edgar, 2004) was occurring. Zinnecker (1982) (Z82) long ago showed that this mass function slope could be produced by BHL accretion, with a dependence of mass accretion rate on accreting mass of $\dot{M} \propto M^2$, as long as enough mass is added to the original distribution of "seed" masses. In this view, the Salpeter slope is steeper because mass growth is often terminated before the fully asymptotic limit can be realized.

However, the standard BHL formula assumes a non-self-gravitating environment of constant density and relative velocity that is not realized in simulations (or in real star-forming regions). Furthermore, the Z82 model assumes sink accretion rates $dM/dt \propto M^2$ which is only roughly (at best) exhibited in simulations (Hsu et al., 2010), partly due to variations in environmental densities and velocities (BP15). These departures led Maschberger et al. (2014) (M14) to argue that BHL accretion was not occurring in their simulations, even though they obtained a Salpeter-like upper IMF slope.

In an attempt to further clarify how gravitationally-driven accretion proceeds in simulations of star formation, in this chapter we present additional numerical experiments with sink formation in isothermal clouds with decaying turbulence. We show that to understand the accretion process it is necessary to consider the self-gravity of the near environment of sinks, not just that of the sink itself. We conclude that gravitational focusing is an effective process for power-law mass functions with $\Gamma \sim -1$.

5.3 Numerical experiments

5.3.1 Basic Assumptions and Sink Implementation

We use the Eulerian fixed grid code *Athena* (Stone et al., 2008) to simulate the collapse of a molecular cloud by self-gravity. We solve the system of equations

$$\frac{\partial \rho}{\partial t} + \nabla \cdot (\rho \mathbf{v}) = 0 \tag{5.1}$$

$$\frac{\partial \rho \mathbf{v}}{\partial t} + \nabla \cdot (\rho \mathbf{v}\mathbf{v} + P) = -\rho \nabla \Phi \tag{5.2}$$

$$\nabla \Phi = 4\pi G \rho \tag{5.3}$$

with periodic boundary conditions. To improve the time order of the scheme, especially in the context of sink dynamics and accretion, we implemented a RK3 integrator (Gottlieb & Shu, 1998), which advances the fluid equations (eqs. 5.1 and 5.2) at third order in time. We further adopt an isothermal equation of state such that $P = c_s^2 \rho$ for simplicity, which is a reasonable approximation for low-mass star-forming regions on the scales we study. The Poisson equation (eq. 5.3) is solved every RK3 substep, using the FFT solver that comes with the stock version of Athena.

We adopt a sink and near-environment ("patch") geometry similar to those in Bleuler & Teyssier (2014) and Gong & Ostriker (2013). The motivation for the sink implementation is twofold; to enable modeling of the dense peaks that occur during gravitational collapse and to study the gas properties of the sink environs. The Truelove et al. (1997) criterion sets the maximum ratio of the cell size Δx to the Jeans length allowed to avoid artificial fragmentation; in the isothermal case, this corresponds to a maximum density

$$\rho_{\mathrm{t}} = \frac{\pi}{16} \frac{c_s^2}{G \Delta x^2}, \tag{5.4}$$

with the sound speed c_s and the (fixed) cell size Δx. Sink-patches can be created when the density peak across a group of cells exceeds ρ_{t}, the flow is converging such that $\nabla \cdot v < 0$ in the patch, and the patch gas is bound, $E_K + E_G < 0$, where E_K is the sum of both bulk motion and thermal energy. The gravitational energy E_G is calculated from the gravitational potential, rather than from the standard equation $3GM^2/5R$, since there can be significant misinterpretation on whether the core is bound or unbound (see Ballesteros-Paredes et al., 2018, for a discussion).

Since the sink patches do not necessarily align with the underlying grid, their content is recalculated at every timestep. Patches are allowed to overlap, but sinks are made to merge when one sink enters another sink's patch. Sinks are initialized with a token mass ($10^{-4}\rho\Delta x^3$) proportional to the local density, and they gain the rest of their mass by accretion from the patch, the reservoir for the sink. The accretion rate onto the sink is dictated by the (net positive) mass flux into the patch and regulated by the ratio of the mean density $\bar{\rho}$ over the threshold density dictated by the Truelove criterion, ρ_t (Eq 5.5, see Bleuler & Teyssier, 2014 for details),

$$\dot{M}_s = \left(1 + \eta \log \frac{\bar{\rho}}{\rho_{\text{thr}}}\right) \int \nabla \cdot (\rho(\mathbf{v} - \mathbf{v}_{\text{sink}}))dV, \tag{5.5}$$

where η is an adjustable parameter. We have experimented with both $\eta = 0.1$ and $\eta = 1$; the results are not sensitive to the particular choice. The resulting sink mass accretion rate $\dot{M}_{\text{sink}}$ and the local patch densities ρ determine how much mass Δm is removed from each cell in the patch by

$$\Delta m = \Delta t \frac{\dot{M}_{\text{sink}}}{n_{\text{cells}}} \frac{\rho}{\bar{\rho}}, \tag{5.6}$$

where n_{cells} is the number of cells in the sink patch. Equations 5.5 and 5.6 regulate the flow of mass onto the sink so as to avoid large jumps in density or velocity. Since mass is removed instantaneously across the patch (but spatially varying, depending on the local density, see eq. 5.6), the size of the patch is the relevant resolution element.

The number of patch cells is tuned by the accretion radius parameter r_{acc}, which determines the number of cells, in addition of the center cell that contains the sink, that make up the radial extent of the patch. The simulations presented here have an $r_{\text{acc}} = 2$, such that the resulting patches contain 5^3 cells in total. Therefore, the linear sink patch size is only slightly larger than the stencil size used for reconstructing the hydrodynamic quantities (3 cells), which determines the actual numerical resolution. Sink-patch data is output as the three dimensional sink velocity, sink position, and the conserved variables in the patch cells (and an additional set of boundary cells).

The gravitational interaction between sinks and between sinks and gas is calculated via the Fourier gravity solver that comes with Athena. To that purpose, the sink mass is distributed on the density grid before the gravity-solve, via the triangular-shaped-cloud scheme using three support points (Hockney & Eastwood, 1981, see also Gong & Ostriker, 2013). Note that this interpolation occurs on the underlying grid, not within the sink patch. Therefore, the sink is not necessarily located at the center of a cell. The standard kernel used in the Fourier solver implies a gravitational softening of one cell. Though this method is not capable of accurately calculating close sink encounters, this is irrelevant for our purposes, since (a) sinks merge when entering each other patches, and (b) the run times are too short for sinks to orbit around each other.

5.3.2 Parameters and Initial Conditions

All the runs used in this chapter are of a 4 pc radius spherical, constant density cloud in a 20 pc box. The initial density of the cloud is $\rho_c = 1.5 \times 10^{-21} \mathrm{g cm^{-3}}$, which is 100 times the ambient density in the box, giving the cloud an initial free-fall time $t_{\mathrm{ff}} = 1.7$ Myr. The simulations are isothermal with a temperature of 14 K, assuming molecular gas with $\mu = 2.4$. We set up a decaying supersonic turbulent power spectrum $P(k) \propto k^{-4} dk$, initially at Mach 8, which leads to an initial velocity dispersion of $\sim 2\,\mathrm{km\,s^{-1}}$ typical of molecular clouds. These supersonic motions dissipate rapidly and the velocity dispersion of the cloud is driven by gravity as the cloud collapses, becoming roughly virial as observed in star-forming clouds(see Ballesteros-Paredes et al., 2011, 2018).

We ran simulations with $N_{\mathrm{cell}} = 256^3, 512^3, 1024^3$, for which the cell size $\Delta x = 0.08$, 0.04, 0.02 pc and the patch radii are $r_p = 0.2$, 0.1, 0.05 pc, respectively. We present our fiducial runs at 512^3 in the following section, and discuss results for the 1024^3 run in the Appendix. Because these simulations are isothermal, the smallest resolvable structures scale with the grid, and therefore details of the fluid dynamics will not converge with increased resolution. However, because isothermal simulations can be rescaled (Hsu et al., 2010),[1] runs with differing grid sizes essentially test whether changing the dynamic range of the simulation affects the overall results. Therefore, while we cannot expect convergence in the details of density and velocity fields, statistical measures such as mass functions can ”approach convergence” when increasing the resolution (e.g. Haugbølle et al., 2018).

5.4 Results

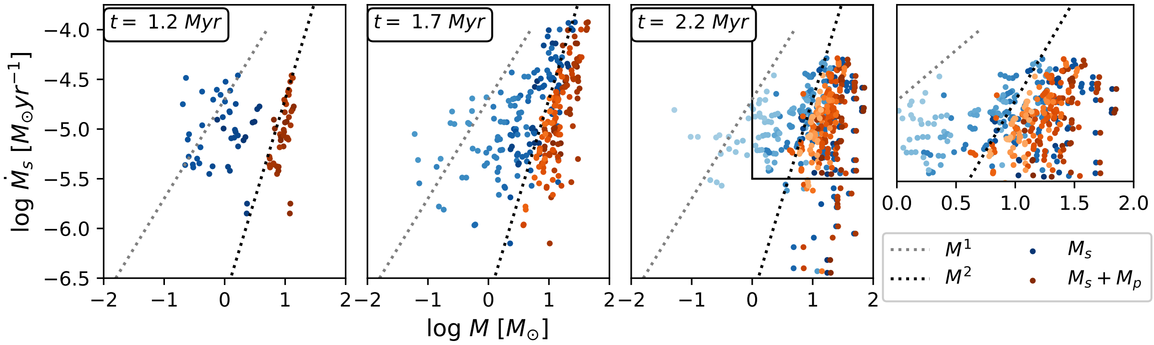

Figure 5.1: Accretion rate onto the sink $\dot{M}_s$ vs sink masses alone M_s (blue) and total mass enclosed within the patch boundary, a sum of the sink mass and patch gas mass $M_s + M_p$ (orange) combining several outputs around 1.2 Myr, 1.7 Myr, and 2.2 Myr in the simulation. Lighter shades of blue and orange are sinks that have formed later in the simulation. The gray dotted line goes as M^1 and the black dotted line as M^2. The inset is a zoom of the x dimension to show the scatter in mass and corresponds to the area of the rectangle drawn in the third panel.

In Figure 5.1 we plot the relationship between the sink accretion rate $\dot{M}_s$, the mass of the sinks M_s, and in contrast, the total mass enclosed within the patches $M_s + M_p$ at three different times in the simulation $t = 1.2,\ 1.7$, and $2.2\,$Myr. This leads to an important insight: the mass-squared dependence is seen much more clearly when using the total mass $M_s + M_p$. At 1.2 Myr, when the first sinks are forming, the accretion rate is tightly correlated with the $\dot{M}_s \propto (M_s + M_p)^2$ dependence, and the correlation is still strong at 1.7 Myr. Near the end of the simulation at 2.2 Myr, the scatter in the accretion vs. total mass relation increases significantly, though the overall

---

[1] If the size scale is changed by a factor of D and the total mass is similarly scaled by D, the density changes by D^{-2}; thus for the same gas temperature the ratio of the sound crossing time to the free-fall time is the same, and the number of initial Jeans masses in the cloud also remains fixed.

mass-squared dependence remains. It is likely that the increased scatter is due to the depletion of the environment as mass accretes onto sinks (BP15), especially for the very massive sinks with low accretion rates; these have strongly depleted their surrounding gas.

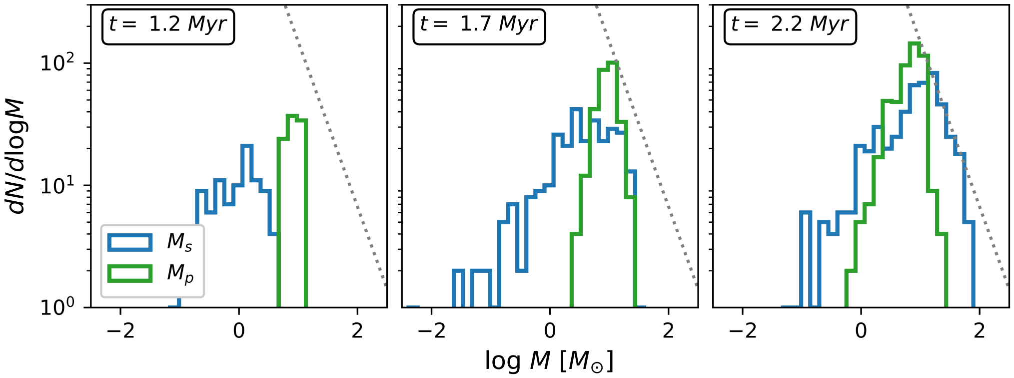

Figure 5.2: Mass functions for the sink mass M_s (blue) and the patch gas mass M_p (green) at 1.2, 1.7, and 2.2 Myr into the simulation. The gray dotted line is the Salpeter slope.

In contrast, the accretion-sink mass relation exhibits much larger scatter and only approaches $\dot{M}_s \propto M_s^2$ at late times. The reason why the dependence of the accretion rate on sink mass is so different is that the sink masses constitute only a fraction of the total gravitating mass throughout most of the simulation. As shown in Figure 5.1, and emphasized by the mass functions shown in Figure 5.2, sink masses can be an order of magnitude smaller than patch masses at early times. It is only near the end of the simulation that many sink masses become comparable to or larger than patch masses, at which point the $\dot{M}_s - M_s$ relation approaches the mass-squared dependence.

Thus, the main objection to attributing the growth of a power-law mass function to BHL-type accretion, that the $\dot{M} \propto M_s^2$ dependence is weakly if at all present (e.g., M14, BP15), is shown to be the result of misidentifying the gravitating mass as only that of the sink.

One question is whether our prescription for sink accretion differs sufficiently from that of the SPH simulations of M14 and BP15, and from some other implementations in grid codes, to strongly affect our basic conclusion. We find that in the simulations shown, with $\eta = 0.1$ (Equation5.5), the accretion rate onto the sink is generally $\sim 90-95\%$ of the accretion rate into the patch, so Figure 5.1 would be essentially unchanged if the patch accretion rate were used instead

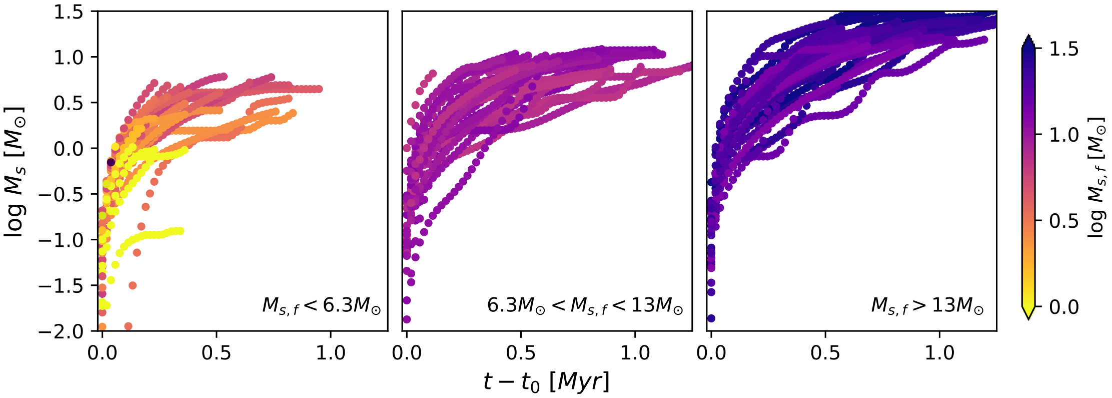

Figure 5.3: The sink mass growth over time, zeroed at the formation time for each sink t_0, shown for three populations binned and color-coded by the final sink mass. From left to right; sinks with a final mass $M_{s,f} < 6.3M_\odot$, $6.3M_\odot < M_{s,f} < 13M_\odot$, $M_{s,f} > 13M_\odot$. All sinks grow rapidly within the first few 0.1 Myr, but turn over at different rates.

of the sink accretion rate; we use the latter for comparison to the literature. (Note that the density and velocity distributions within the patch must be uncertain due to limited resolution of the hydrodynamics, such that more complex prescriptions are not clearly warranted.)

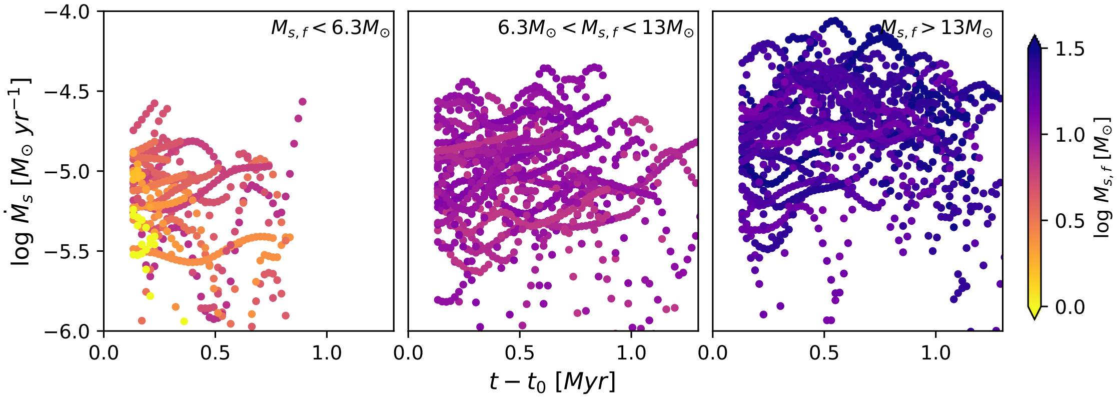

Figure 5.4: Time averaged sink accretion rate $\dot{M}_s$ as a function of the time since formation $t - t_0$, binned and color coded by final sink masses for the same sinks as in Figure 5.3. Each panel represents a different final sink mass range. From left to right: lower mass sinks - $M_s < 6M_\odot$, intermediate mass sinks - $6M_\odot < M_s < 13M_\odot$, and highest mass sinks - $M_s > 13M_\odot$. Individual sink mass growth rates are highly variable, even when averaged across 0.1 Myr windows.

More generally, our results for the accretion rates onto sinks as a function of time show the characteristic "banana-shaped" shape seen the SPH simulations (e.g., Figure 1 in M14 and Figure

14 in BP15), the large fluctuations in accretion rates with time (Figure 5.4 as in M14 (their Figures 1 and 2), and a correlation of final sink masses with initial times of formation (Figure 5.5; cf. Figure 12 of M14 and Figure 15 of BP15). Thus, there is no indication from the behavior of dM_s/dt for individual sinks for a qualitative difference in behavior from M14 and BP15, despite the differences in the algorithms for sink accretion.

In addition, as in other simulations with sink formation in a turbulent environment (e.g., Figures 1 and 2 in M14), "instantaneous" accretion rates show frequent fluctuations of an order of magnitude or more over timescales of $\sim 0.1-0.3$ Myr (Figure 5.4). In our case, these fluctuations are related to the clumpy and moving filamentary structure of the gas in the sink environments (Smith et al., 2011).

As shown in the Appendix 8.2, increasing the resolution to 1024^3 results in the formation of a larger number of sinks with smaller masses; however, the main conclusion of this chapter, that the dM_s/dt tracks $(M_s+M_p)^2$ much more closely than M_s^2, is unchanged.

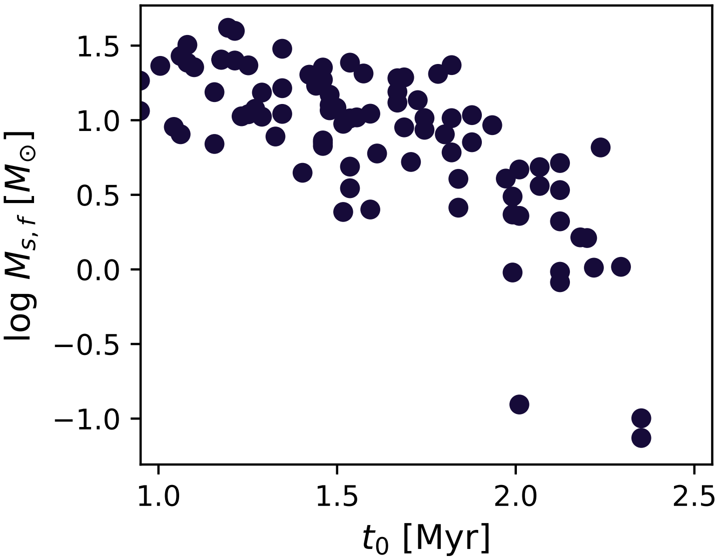

Figure 5.5: Final mass of the sinks in the simulation vs their formation time in the simulation.

These simulations only begin to provide an indication of a power-law upper mass function at 2.2 Myr (Figure 5.2). This is consistent with the argument from the simple BHL accretion model of Z82, in which the power-law distribution only develops once the masses have grown well beyond their initial values. In our case, the relevant initial mass distribution is not that of the sinks but that of the patches, as the patches set our effective resolution limit for the dynamics. With initial patch masses $\sim 5-10$ $\mathrm{M}_\odot$ (left panel of Figure 5.2), mass growth to $\sim 10^2 \mathrm{M}_\odot$ is required to produce sufficient dynamic range to indicate a power-law behavior. (We note that the power-law distribution is more apparent in the higher-resolution run; see Figure A.2).

5.5 Discussion

The essence of the BHL accretion formula is the concept of accretion from material passing within a gravitational capture radius $r_g \sim GMv^{-2}$, where in the simplest model v is flow past the point mass. Then

$$\frac{dM}{dt} = \alpha M^2\,, \tag{5.7}$$

where $\alpha \approx 4\pi G^2 \rho v^{-3}$, where $v^2 = v_b^2 + c_s^2$, v_b and c_s being the bulk flow velocity and sound speed, respectively (Edgar, 2004). Z82 then showed that if $\alpha =$ constant, then the mass of an individual object grows with time as

$$M(t) = \frac{M_0}{1-\alpha M_0 t} \tag{5.8}$$

where M_0 is the initial mass at $t = 0$.

M14 argued that BHL-type accretion was not occurring in their simulations, based on the departure of $\dot{M}$ from a M_s^2 relation. However, we have shown in our simulations that the mass-squared dependence *does* occur for $\dot{M}$ as a function of the total mass $M_s + M_p$, though with some scatter. Furthermore, we can check this result by revisiting the data from BP15. In Figure 5.6 we show a reanalysis of the BP15 results now plotting the mass accretion rate vs. the sum of the sink mass plus the mass of the near environment. As in the *Athena* simulations, the resulting distribution much more clearly exhibits the mass-squared dependence (compare with Figure 2 in BP15), again with significant scatter. The recognition of the importance of mass in the near-sink environment thus demonstrates how the power-law distribution $\Gamma \rightarrow -1$ seen in the BP15 simulations arose.

Thus, the gravitating mass that should be considered in reference to Equation5.7 is the total in the near environment, not just that of the sink. This is especially important at early times, when the sink mass is much lower than the patch mass. As seen in Figure 5.1, when the sink mass grows to be comparable to or larger than that of the patch mass, the mass accretion rate approaches M_s^2 as expected.

The fast initial rise in $\dot{M}$ as a function of the sink mass is qualitatively different than predicted by Equation 5.8. As argued by M14 and BP15, this phase is analogous to the formation of a central protostar surrounded by a massive envelope, as seen for example in the collapse of Bonnor-Ebert spheres or clouds of similar structure, which show an initial spike of very rapid central accretion (Foster & Chevalier, 1993; Henriksen et al., 1997). However, at the same time as the central protostar (sink) is undergoing this rapid phase of accretion, the protostellar envelope can be accreting at the mass-squared accretion rate, as shown in Figure 5.1.

Our patch masses, with their arbitrary size scale, are only a crude proxy for the gravitating mass responsible for accreting gas from the general environment. Indeed, it is not clear what prescription one should use to distinguish between "protostellar core/envelope" and "external environment" in a continuous medium. The size scale over which the accretion rate is measured naturally affects the value of $\dot{M}_s$, but the mass-squared dependence persists over a range of tested patch sizes - from 0.05 pc to 0.25 pc. The much stronger correlation of accretion rate with total mass, and its much closer approach to a mass squared dependence, adequately illustrates the need to consider scales well beyond that of the sink to see the mass-squared relation.

One common feature of simulations with sink formation in a turbulent environment is that (e.g., Figures 1 and 2 in M14), "instantaneous" accretion rates show frequent fluctuations of an order of magnitude or more over timescales of $\sim 0.1-0.3$ Myr (Figure 5.4; see also Figures 1 and 2 in M14). These fluctuations are related to the clumpy and moving filamentary structure of the gas in the sink environments (Smith et al., 2011). The result is a scatter in $\dot{M}$ that tends to obscure the overall mass dependence. Furthermore, the increasing scatter in the $\dot{M}$ vs. (M_s+M_p) relation as the simulation proceeds is arguably due to depletion of the environment as the sinks accrete mass. This of course is inconsistent with the Z82 model (cf. Equation5.8; Figure 5.4).

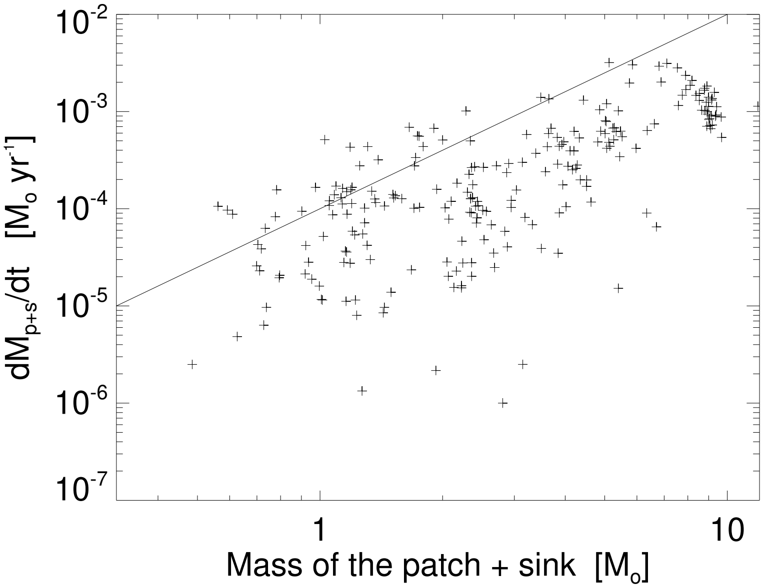

Figure 5.6: Accretion rates for run 22 of BP15 at $t = 2.5 \times 10^4$ yr, plotted as a function of the total mass within 6 $R_{\rm outer} = 1.08 \times 10^{-3}$ pc, where $R_{\rm outer}$ is the external radius where the physical properties are evaluated to determine whether an sph particle will be accreted or not (see BP15). The M^2 relation is clearer than using simply the sink mass (compare with Figure 2 of BP).

M14 argued any theory of the mass function must take the long- and short-timescale variations of accretion into account, as well as the difference in accretion times. However, this is not necessarily the case. Assume accretion is given by Equation5.7 holds for each mass M_i; then integration yields

$$\frac{1}{M_i} = \frac{1}{M_{i,0}} - \langle \alpha t \rangle_i \,, \tag{5.9}$$

where $M_{i,0}$ is the initial mass and $\langle \alpha t \rangle_i \equiv \int_{t_{0,i}}^{t_{f,i}} dt\, \alpha_i$. Starting from Equation5.9, Z82 showed that for constant $\langle \alpha t \rangle_i = \alpha t$, an initial distribution of masses $M_{i,0}$ could grow to produce a power-law distribution of final masses M_i with $\Gamma \rightarrow -1$ asymptotically. However, it is clear that alternatively one can fix $M_{i,0}$ and still produce the power law distribution of M_i by adopting a suitable variation in $\langle \alpha t \rangle_i$.

To provide a simple demonstration of how a range in accretion rates and times can produce a power law mass distribution, we use Equation5.9 to calculate the final masses for 200 objects, all with the same initial mass $M_{0,i} = 1$, and with a uniform spacing in $\langle \alpha t \rangle_i$ between 0 and 0.9. The

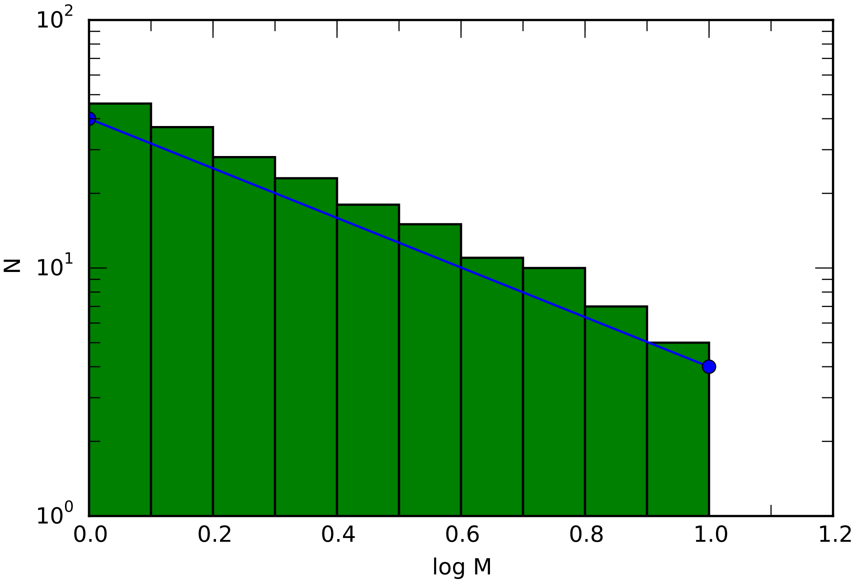

Figure 5.7: Histogram of the mass distribution using Equation5.9 for a population of 200 objects with an initial starting mass of unity with uniformly spaced values of $\langle \alpha t \rangle_i$ between 0 and 0.9 (see text). The straight line is not a fit, but demonstrates a slope of $\Gamma = -1$.

resulting histogram of the M_i distribution is shown in Figure 5.7, demonstrating the emergence of a $\Gamma \sim -1$ power law (straight line).

Thus, variation in $\langle \alpha t \rangle$, due either to varying $\alpha(t)$ or $t_f - t_0$, or both, need not prevent the development of the upper mass power law with $\Gamma \to -1$. In particular, simulations with $t_f =$ constant but differing $t_{0,i}$ can be accommodated with a suitable distribution of starting times; all that matters is the total mass accretion at the end of the calculation. As the final mass will tend to be larger for those objects that form first, as seen in Figure 5.5. Of course, not every possible distribution of $\int_{t_{0,i}}^{t_{f,i}} dt\, \alpha_i$ and $M_{0,i}$ will produce a clear asympotic power law mass distribution in M_i; further exploration of various forms may be instructive.

The actual simulation behavior is of course more complicated than in the above example. We therefore conducted some simple numerical simulations in which we evolve a population of stars with distribution of masses $\xi(M_0)$ through time as they accrete according to a BHL-like prescription (Kuznetsova, 2018)[2]. At each timestep, each star's current mass M_i is evolved to it's mass at the next timestep M_{i+1} with the equation:

---

[2] Codebase: `https://github.com/akuznetsova/BHL`

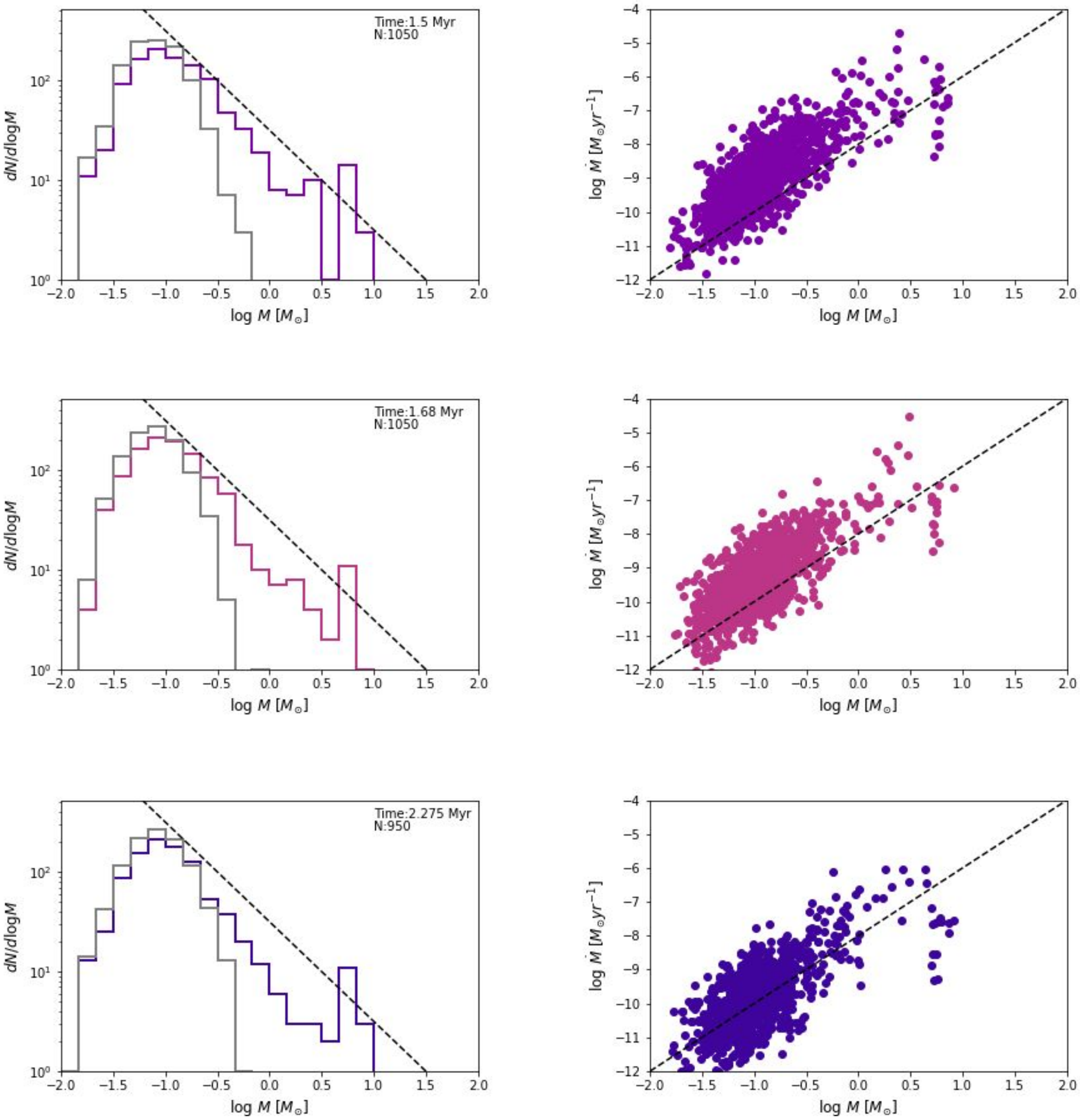

Figure 5.8: Mass functions $\xi(M)$ (Left) and dM/dt vs M (Right) for three types of simulation prescriptions. The initial $\xi(M_0)$ distribution sampled is shown as a light gray histogram. The dashed line on the mass function plot has a slope of -1 in dN/dlogM space. The dashed line on the dM/dt plot has a slope of 2. From top to bottom: a constant log-normal α distribution shown at $t = 1.5$ Myr - scatter originates from random sampling and spread in α. Middle row: A log-normal distribution of α that shifts to lower values over time shown at $t = 1.68$ Myr, where the primary difference is that it takes slightly longer to develop the power law tail. Bottom row: The same decreasing distribution of α, with a spread in star formation - that is the $\xi(M_0)$ is sampled at a specified star formation rate, forming 50 stars every 0.125 Myr, shown here at $t = 2.275$ Myr. Note that the distribution of dM/dt appears to have a different slope with regards to the mass, despite having the same $\dot{M} \propto M^2$ accretion prescription.

$$M_{i+1} = M_i + \alpha_i M_i^2 dt \tag{5.10}$$

where α_i is drawn randomly from a log-normal distribution. In Figure 5.8, we show $\xi(M)$ and dM/dt vs. M for three different cases all with a similar $\xi(M_0)$ drawn from a log-normal distribution centered at $\mu = 0.08 M_\odot$ with a spread of $\sigma_{\log M} = 0.25$, where $N_{\rm total} = 1050$, and all with the same starting α_0 distribution. For all cases, when masses reach a threshold mass of 8 $M_\odot$, the α value for only those stars is decreased by a factor $f(t) = 20(1 + t/t_{end})$ to avoid runaway growth of massive sinks and to account for massive stars eventually running out of material that they can accrete.

In the first case, α_i is drawn randomly from the same log-normal distribution at every time. This starting distribution α_0 is centered at $10^{-6} M_\odot^{-1} {\rm yr}^{-1}$ with logarithmic spread $\sigma_{\log\alpha} = 0.75$; these parameters are chosen to produce a reasonable range of values of dM/dt ($10^{-11} - 10^{-5} M_\odot yr^{-1}$) given a typical range of masses, $0.01 - 25 M_\odot$. This configuration can build a power-law tail for the mass function, even though the range of α can span ~ 4 orders of magnitude. In the next case, in order to simulate an environment being depleted of accretable material, α_i is drawn from a distribution shifting to lower values over time where $\alpha(t) = \alpha_0(1 - (t/t_{end})^2)$. The primary effect of this change is that, as expected, it takes a longer time for the power-law tail to develop. In the last case, in addition to the decreasing values of α_i, the stars are formed not all at once, but throughout the simulation, i.e. stars are drawn from $\xi(M_0)$ at a specified star formation rate - 50 new stars are initialized every 0.125 Myr. The slope of accretion rates vs stellar mass in Figure 5.8 is slightly steeper than mass squared, even though each simulation has the accretion rate explicitly prescribed to scale with M^2.For less massive stars, this departure from the M^2 relation is a result of the scatter in the α values and the shape of the mass function itself, rather than a difference in accretion behavior. At the most massive end, the mass loss rates begin to fall below the M^2 trend due to the additional factor $f(t)$ used when stars exceed a threshold mass in order to avoid runaway accretion, as described above. This reduction in accretion rates also results in the spike or pile up of objects at around $\log M \sim 0.8$ in the mass functions.

While the above analysis indicates that BHL-type gravitationally-focused accretion can produce upper-mass power-law mass functions, the emergence of the power law is dependent upon a) having a mechanism for starting a "seed" mass from a non-BHL process (via thermal fragmentation, for example) and b) growing masses well beyond the initial seed mass distribution. This suggests that the star cluster mass function should provide a better example of gravitational focusing producing a power law mass function (e.g., Kuznetsova et al., 2017), as the thermal fragmentation scale relative to the final mass should be much smaller in the cluster case than for the stellar mass function.

5.6 Summary

We have presented isothermal hydrodynamic simulations with sink formation to explore the effects of gravity in accretion. We found that, by including the mass in the near environment of sinks, the accretion rates exhibit an M^2 dependence similar to that in simple BHL accretion. Our findings strongly suggest that the apparent inconsistencies found in previous analyses were the result of only considering the sink mass, which at early times strongly underestimates the relevant gravitating mass. We also developed toy models to illustrate that several features seen in simulations that are incompatible with the simple Z82 model – complex time dependence of mass addition, departure from the M^2 dependence of accretion rate on mass in snapshots, range of accretion timescales, correlation of final mass with time of initial formation – are compatible with gravitationally-focused accretion. In turn, this provides an explanation for how the $\Gamma \to -1$ mass function tends to develop.

The gravitationally-focused accretion outlined here is a major feature of the "competitive accretion" model for star formation (e.g., Bonnell et al., 2001a,b, 2008), though in our case a global tidal potential plays no significant role. The slightly steeper Salpeter slope in our interpretation results from the exhaustion of material, especially as stellar feedback can be an important factor in dispersing gas; simulations with feedback are needed explore this conjecture.

5.7 Acknowledgements

This work was supported in part by NASA grant NNX16AB46G, by the University of Michigan. JBP acknowledges financial support from UNAM-PAPIIT grant number IN110816. We used computational resources and services provided by Advanced Research Computing at the University of Michigan, Ann Arbor, and by the Information and Technology Services at UNC Chapel Hill.

CHAPTER 6

The Origins of Protostellar Core Angular Momenta

This chapter appears in the Astrophysical Journal, Volume 876, pp 33 (Kuznetsova et al., 2019). This work was co-authored with Lee Hartmann and Fabian Heitsch. The paper is reproduced here with minor stylistic revisions.

6.1 Abstract

We present the results of a suite of numerical simulations designed to explore the origin of the angular momenta of protostellar cores. Using the hydrodynamic grid code *Athena* with a sink implementation, we follow the formation of protostellar cores and protostars (sinks) from the sub-virial collapse of molecular clouds on larger scales to investigate the range and relative distribution of core properties. We find that the core angular momenta are relatively unaffected by large-scale rotation of the parent cloud; instead, we infer that angular momenta are mainly imparted by torques between neighboring mass concentrations and exhibit a log-normal distribution. Our current simulation results are limited to size scales ~ 0.05 pc ($\sim 10^4$AU), but serve as first steps toward the ultimate goal of providing initial conditions for higher-resolution studies of core collapse to form protoplanetary disks.

6.2 Introduction

Disk formation is a natural consequence of gravitational collapse of protostellar cores even without complete angular momentum conservation, given the large difference in sizes between cores and stars. The disk mass surface density distribution, of obvious importance for understanding planet formation, results from the angular momentum distribution of the infalling protostellar envelope, modified by transport processes within the disk (Cassen & Moosman, 1981). The expected low turbulence in large regions of protoplanetary disks (see review by Turner et al., 2014), supported by observational limits (Flaherty et al., 2017, 2018) suggest that turbulent angular momentum transport is generally quite slow. Transport by disk winds may dominate (Bai, 2016), but winds may well be trapped by the infalling envelope, rendering them ineffective in redistributing mass until the infall phase ends. Thus, the early structure of protostellar and protoplanetary disks may be dominated by the angular momentum distribution of the parent infalling envelope. Given the increasing evidence for early planet formation (e.g., ALMA Partnership et al.,, 2015), developing a better understanding of envelope angular momenta is essential.

The analytic rotating collapse model of Terebey et al. (1984) (hereafter TSC) has been used often to predict disk structures and other properties assuming various levels of turbulent viscosity (for example, Zhu et al., 2010; Bae et al., 2014, 2015; Hartmann & Bae, 2018). However, the assumption of initial solid-body rotation in the TSC model is not necessarily realistic; differing distributions of angular momenta would result in differing initial disk mass distributions.

Due to the short dynamical timescales and spatial orders of magnitude inherent in gravitational collapse, a top-down approach that starts from cluster scales is necessary to develop better parameters for model input that accurately reflect that of a population of protostellar disks formed in a realistic environment. By far the most extensive investigation of disk formation with this approach is that of Bate (2018), who analyzed the properties of circumstellar disks formed in a radiation hydrodynamic simulation (Bate, 2012). The disks exhibited a wide range of properties, with typical radii ~ 100 AU and surface densities $\Sigma \propto R^{-1}$, in reasonable agreement with observational constraints. However, many disks were not well-resolved, and the amount of disk evolution due to artificial viscosity was not clear.

In this chapter we address a simpler, more basic, and more self-contained problem: what sets the angular momenta of protostellar cores? To this end, we present results from a series of numerical experiments based on the picture of cluster formation via sub-virial (cold) collapse, as in Kuznetsova et al. (2015). These simulations provide a distribution of initial conditions for disk formation by core collapse and allow an investigation of the importance of global cloud rotation on the angular momenta of individual cores.

Using a sink implementation that keeps track of properties in the near environments of sinks (e.g., the surrounding cloud core), we find that the resulting angular momenta do not behave according to the expectations of the TSC model, with no detected smooth growth of angular momentum over time for the protostars as a whole. This suggests that initial disk surface densities might be flatter, i.e. a weaker function of radius, than typical disk models, with implications for planet formation. The angular momentum of cores is insensitive to the global cloud rotation, indicating that the angular momentum inputs to the cores are the result of local gravitational torques. As in Bate (2018), we find considerable time variability in the accretion of the angular momenta and mass, which is the product of a lumpy episodic non-isotropic accretion of material onto the protostellar cores. These first results set the stage for further studies exploring the role of magnetic fields and higher-resolution simulations to provide more detailed collapse models as an essential input to investigations of protoplanetary disk structure.

6.3 Method

6.3.1 Basic Assumptions and Sink Implementation

The methods used here were described in (Kuznetsova et al., 2018), so we provide a short summary here. We use a modified version of the Eulerian grid code *Athena* (Stone et al., 2008) to simulate the collapse of a molecular cloud by self-gravity. We solve the system of equations

$$\frac{\partial \rho}{\partial t} + \nabla \cdot (\rho \mathbf{v}) = 0 \tag{6.1}$$

$$\frac{\partial \rho \mathbf{v}}{\partial t} + \nabla \cdot (\rho \mathbf{v}\mathbf{v} + P) = -\rho \nabla \Phi \tag{6.2}$$

$$\nabla \Phi = 4\pi G \rho \tag{6.3}$$

with an RK3 integrator (Gottlieb & Shu, 1998), which advances the fluid equations (eqs. 6.1 and 6.2) at third order in time. We further adopt an isothermal equation of state such that $P = c_s^2 \rho$ for simplicity, which is a reasonable approximation for low-mass star-forming regions on the scales we study. The Poisson equation (eq. 6.3) is solved every RK3 substep, using the FFT solver that comes with version 4.2 of Athena.

Using the same methods as our preceding companion paper on the accretion of the cores Kuznetsova et al. (2018), we adopt a sink-region geometry similar to those described in Bleuler & Teyssier (2014); Gong & Ostriker (2013), where at every timestep an accretion reservoir is drawn centered on the sink, which will hereinafter be referred to as the *sink-patch*. The radius of the sink-patch is set by the parameter r_{acc}, which describes the number of cells to be included in the patch radius, in addition to the central cell which houses the sink particle. Sink accretion of radially infalling material occurs instantaneously across the patch and leftover angular momentum is deposited in the patch cells; the diameter of the sink-patch, $2r_{acc} + 1$ cells , is the relevant resolution element to consider for our study.

6.3.2 Initial Setups

All of the simulations are initialized in a 20 pc box with a spherical top-hat density profile, where the ambient density is $\rho_0 = 1.5 \times 10^{-23}$ g cm^{-3} and the 4 pc radius spherical cloud has a density of $\rho_c = 1.5 \times 10^{-21}$ g cm^{-3}, giving an initial free-fall time of $t_{\rm ff} = 1.7$ Myr for the cloud. The initial conditions are seeded with a decaying Mach 8 supersonic turbulent velocity spectrum $P(k) \propto k^{-4} dk$, which introduces some base level of cloud angular momentum. On average, across all the turbulent random seeds, the total initial angular velocity from turbulence at the cloud scale is $\Omega_k = 0.1 \pm 0.03$ $\mathrm{kms^{-1}pc^{-1}}$, where the specific angular momentum at the cloud scale about the central axis from the cloud scale eddies is $j = 1.97 \times 10^{23} \pm 0.6$ $\mathrm{cm^2 s^{-1}}$. For greater physical insight, in the following we specify Ω^{-1} values in terms of Myr. We explore a parameter space of additional angular momentum input with several values of constant angular velocity added to the entire cloud which we refer to by the initial rotation period for the entire cloud: $\Omega_c^{-1} = 6, 3, 1.5\,\mathrm{Myr}$ (compare to the initial free-fall time of cloud at 1.7 Myr), where the turbulence only runs have average cloud scale rotation periods of $\Omega_k^{-1} \sim 10\,\mathrm{Myr}$. We supplement the runs in Kuznetsova et al. (2018) with additional high resolution runs, such that there is data at three resolutions; $N_{cell} = 256^3, 512^3, 1024^3$ and where the cell size is then $\Delta x = 0.08, 0.04, 0.02\,\mathrm{pc}$, respectively. In this chapter, we focus on data from the intermediate and highest resolutions to compare resolution effects and discuss the measurement of angular momentum at different scales. The fiducial run used in this work, HR_s2, has 1024^3 grid cells with $\Delta x = 0.02\,\mathrm{pc}$, a patch radius of $r_p = (r_{acc} + 1/2)\Delta x = 0.05\,\mathrm{pc}$, and an isothermal temperature $T = 14$ K. The list of runs used in this work and some of their attributes can be found in Table 6.1.

Table 6.1: A tabulated list of runs and their initial parameters used for this study. All runs have $r_{acc} = 2$ and $T = 14$ K.

Run	Seed	Ω_c^{-1} [Myr]	Ω_k^{-1} [Myr]	$\mathrm{t_{end}}$ [Myr]	$\mathrm{N_{sink}}$	$\langle n_s \rangle$ [$\mathrm{pc^{-3}}$]
$N_{cell} = 512^3$						
IR_s0	0	...	15	2.35	98	0.018
IR_r1_s0	0	6	15	2.35	66	0.012
IR_r2_s0	0	3	15	2.35	42	0.009
IR_r3_s0	0	1.5	15	2.35	19	0.002
$N_{cell} = 1024^3$						
HR_s2	2	...	10	2.1	115	0.028
HR_s0	0	...	15	1.9	110	0.024
HR_s1	1	...	8	2.4	70	0.011
HR_r1_s0	0	6	15	1.9	122	0.028
HR_r1_s1	1	6	8	2.5	88	0.014
HR_r2_s0	0	3	15	1.9	134	0.032
HR_r2_s1	1	3	8	2.5	54	0.009
HR_r3_s0	0	1.5	15	1.9	102	0.024
HR_r3_s1	1	1.5	8	2.5	10	0.001

6.3.3 Sink-Patch Data

Sink-patch data is output as the three dimensional sink velocity, sink position, and the conserved variables in the patch cells (and an additional boundary cell). The angular momentum of the patch is summed over the entirety of the patch cells $L = \Sigma_i m_i \mathbf{v}_i \times \mathbf{r}_i$ where m_i is the mass enclosed within the cell, $\mathbf{v}_i$ is the cell velocity relative to the sink and $\mathbf{r}_i$ is the radial distance of the cell center from the sink. The specific angular momentum is then the angular momentum divided by the total mass enclosed within the patch radius. As mass is removed from cells during sink accretion, angular momentum is removed from the patch and is implicitly put into the sink. The sink angular momentum is tracked during the calculation and is always an insignificant fraction of the patch angular momentum, so we do not consider it further.

To ensure that we discuss the angular momentum inheritance and evolution of systems where the angular momentum will go into the disk, we filter the dataset to remove sinks that are not likely to be single systems by virtue of three possible processes detailed below; sink merging, unresolved fragmentation, or rotational fragmentation.

Sink merging occurs when one sink enters anothers patch; these sinks are then merged into one sink with a combined mass. We identify sinks by unique id numbers and remove all instances of sinks post merger in the data set. The sink implementation requires both a negative gradient in the potential and an increasing density profile across the entire patch, so fragmentation due to the presence of two perturbed density peaks like that of the BB test (Boss & Bodenheimer, 1979) is unlikely. However, in some cases, it is possible that fragmentation could occur and we are simply not resolving separate density peaks that are spaced closer than the size of one grid cell Δx. Thus, we aim to remove sinks that could have fragmented shortly after formation on the basis of their initial angular momentum and mass. That is, sinks are removed if all of their initial angular momentum and mass when put into circular, equal-mass binaries results in separations that would be unresolved in our simulations. Lastly, we consider the conditions for rotational fragmentation of collapsing cores from Sterzik et al. (2003), which dictate that if the initial ratio of rotational energy to gravitational energy $\beta_0 \geq 0.02$ for a centrally concentrated core, the system is liable to rotationally fragment into a binary.

6.4 Results

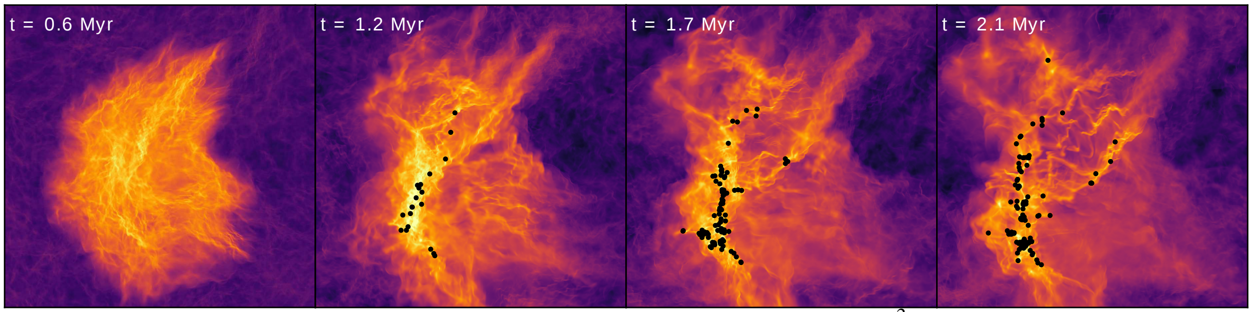

Figure 6.1: The evolution of the cloud in the high resolution ($N_{cell} = 1024^3$) fiducial run, shown here as the column density in the inner 12 pc of the simulation domain at four different snapshots in time $t = 0.6, 1.2, 1.7, 2.1$ Myr.

The initially sub-virial cloud undergoes global gravitational collapse, growing sheet-like and then filamentary over time. Gaseous overdensities seeded by the decaying turbulence rapidly grow until they reach the threshold density and form sinks, preferentially embedded in the filament. The fiducial run is evolved to $1.3t_{\rm ff}$ (Figure 6.1 shows the simulation column densities and sinks at four time snapshots), during which time it forms 115 sinks. At 1 $t_{\rm ff}$, the median sink mass and median enclosed patch mass are 4.5 $M_\odot$ and 10.2 $M_\odot$, respectively.

6.4.1 Angular Momenta Distributions

Figure 6.2 shows the values of mass and angular momenta enclosed in the patch for the fiducial run at a time of 2.2 Myr and highlights the populations of potential contaminants from each category (e.g., likely unresolved multiple systems). We find that the specific angular momenta at all times are consistent with a log-normal distribution. At the end of the fiducial run, the median value of the specific angular momentum is 3.2×10^{21}cm^{2}s^{-1}, or $\sim 1.0 \times 10^{-2}$kms^{-1}pc for the fiducial run; this is in reasonable agreement with the results of Goodman et al. (1993) at scales of $\sim 0.05 - 0.1$ pc.

Overall, the median specific angular momentum varies very little over time, while individual

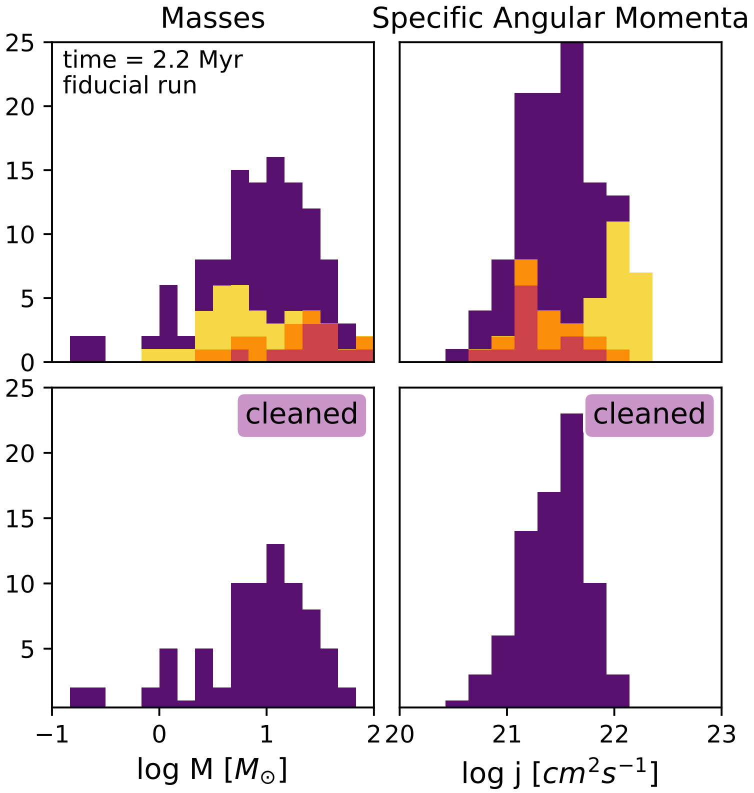

Figure 6.2: Stacked histograms showing the masses (left) and specific angular momenta (right) of all of the sink-patch systems in the simulation (violet) Top row: with the likely multiples highlighted: sinks that merged as ”mergers” in red, sinks that would have orbital radii within one central cell as ”unresolved” in orange, and sinks that could rotationally fragment as ”rotational” in yellow. Bottom row: Histograms showing the distributions of sink masses (left) and patch specific angular momenta (right) within the patches in the simulation after the likely multiples have been removed. The sinks shown are for the fiducial run at a time of 2.2 Myr into the simulation.

sink-patch specific angular momenta can be highly variable, as shown in Figure 6.3. These patches can drastically increase and decrease their total angular momenta over small accretion episodes, however, the long term trend is that patch specific angular momenta do not grow appreciably over time. During accretion episodes, patches seem just as likely to lose angular momentum as they are to gain it.

In addition, we construct the spin parameter, a ratio of the specific angular momentum in the sink-patch to the maximum possible angular momentum the core can have ,$\lambda_s = j/(p(GMR)^{1/2})$ as a measure of the angular momentum budget in use for a patch, where $M = M_s + M_p$ is the total mass enclosed within the patch and $R = r_p$. For specificity, we adopt $p = 2/5$, the rotation

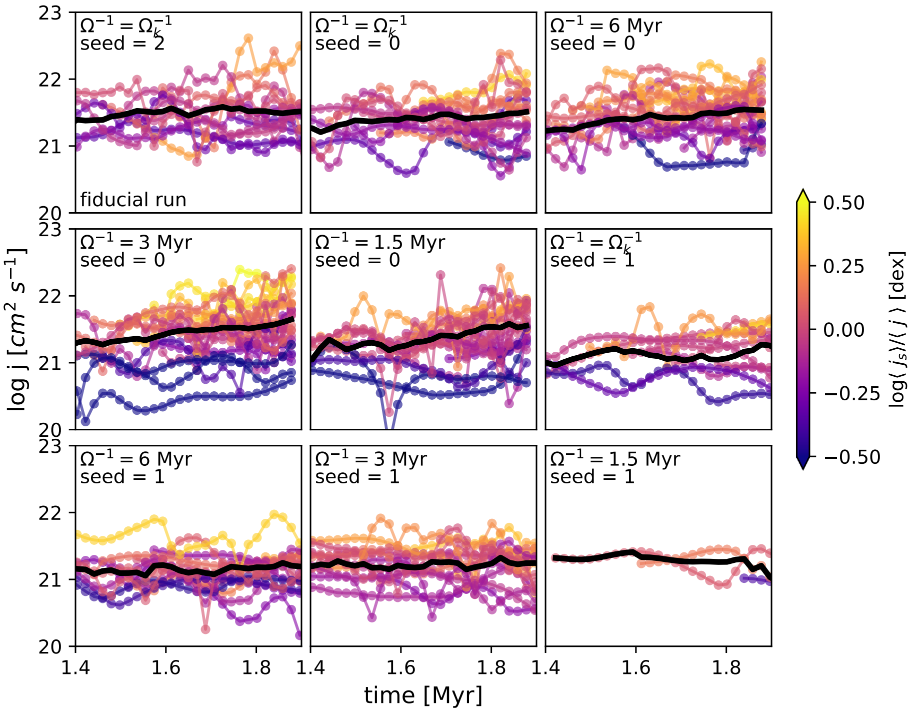

Figure 6.3: Specific angular momenta of subsets of patches for each of the high resolution runs from 1.4-1.9 Myr into the simulation, covering the formation of the first sinks to 1.1 $t_{\rm ff}$ are shown. The colored tracks are individual sinks in the run and the bold black line is the median value of the specific angular momentum at each time. The colorbar denotes how far the mean value for each individual sink track deviates from the median of all sinks in dex. These colors identify individual sinks, making it easier to see that there is little time evolution in j.

coefficient for a uniform density sphere. The behavior of the median spin parameter closely follows that of the total angular momentum and is also log-normally distributed.

The median values for specific angular momentum in Figure 6.3 are not consistent between runs. In Figure 6.4, we plot the quantities as a function of the bulk stellar density $\langle n_s \rangle$ at one free fall time for each simulation - both intermediate resolution runs where metrics are measured at $r_p = 0.1$pc and high resolution at $r_p = 0.05$pc. The bulk stellar density is calculated by computing the density of stars over the minimum spherical volume that contains every star in the simulation.

Among the high resolution runs, the median specific angular momenta at $r = 0.05$ pc are between $\sim 1.2 - 3.2 \times 10^{21}$cm^{2}s^{-1} and between $\sim 4 - 5.5 \times 10^{21}$cm^{2}s^{-1} for intermediate resolutions measured at $r_p = 0.1$pc (Figure 6.4 a). At similar bulk stellar densities, there is a factor of $\sim 2 - 2.5$

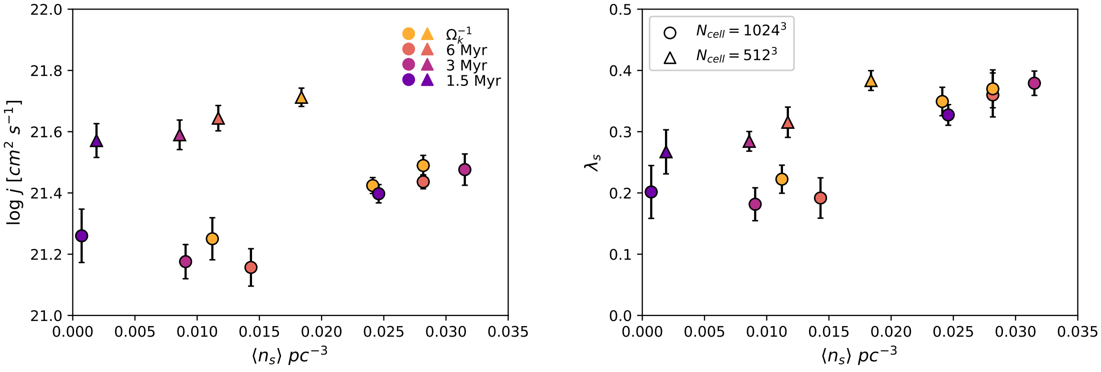

(a) (b)

Figure 6.4: For 4 intermediate ($N_{cell} = 512^3$) and 9 high resolution ($N_{cell} = 1024^3$) runs, shown here are median quantities averaged over the simulation time, weighted by the number of sinks at each time for (a) specific angular momenta and (b) spin parameter λ_s vs the bulk stellar density (at $t_{\rm ff}$) for each simulation. Vertical error bars denote the standard deviation of the median value over time. Markers of the same color denote runs that have the same initial rotation input but different turbulent seeds; for the initial rotation inputs of $\Omega^{-1} = \Omega_k^{-1}, 6, 3, 1.5$ Myr, the marker colors are yellow, peach, magenta, and violet, respectively. Both quantities scale with bulk stellar density, although there appears to be less correlation at lower stellar densities. The intermediate and high resolution runs are measured at different scales, $r_p = 0.1$ pc and 0.05 pc, respectively.

offset between the specific angular momenta of the intermediate and high resolution runs. Given the two-fold increase in resolution, a factor of 2 difference in specific angular momentum is expected from basic scaling arguments. Using the spin parameter reduces this effect, shown in Figure 6.4 b where the gap between resolutions narrows. In either case, it is evident that both specific angular momenta and spin parameter directly scale with $\langle n_s \rangle$. In terms of angular momentum budget, higher stellar densities lead to $\sim 35\%$ of angular momentum budget usage, while lower stellar densities, where stars form in more isolated environments, have stars that use $\sim 20-25\%$ of the maximum.

Different bulk stellar densities can be a result of the random seed for turbulent input or the initial additional angular momentum input. The turbulent seeds contribute to different initial filament geometries; initially centrally concentrated filament geometries tend to produce a higher stellar surface density as opposed to simulations which produce a spoke of sub-filaments which form a more diffuse network of stars.

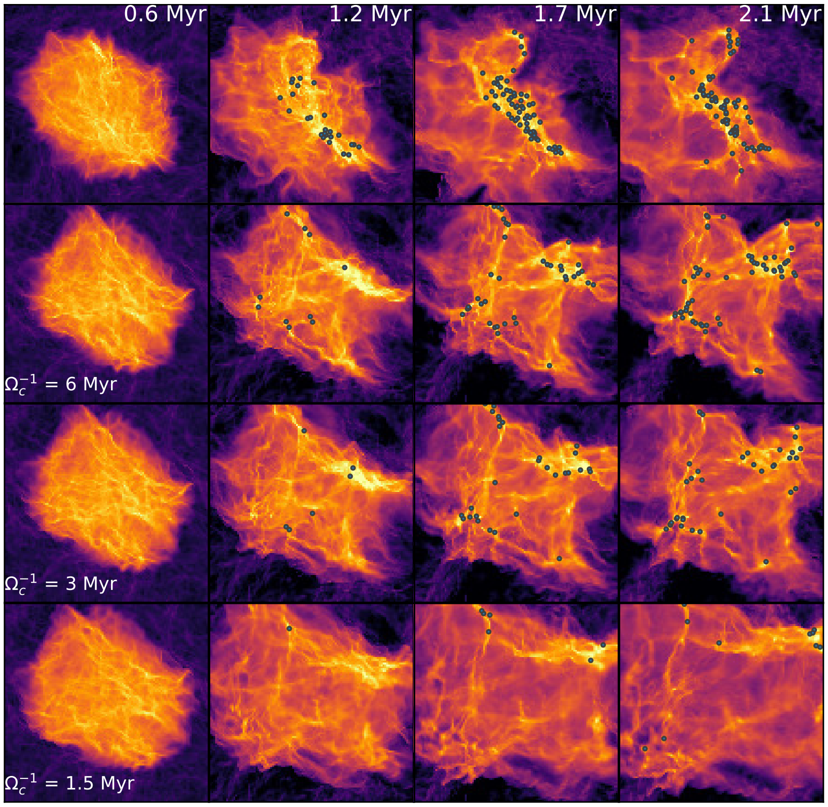

Figure 6.5: Column density projections of the runs with differing initial global rotation input zoomed in on the central 12 pc of the simulation box. Each row shows a run at 512^3 resolution with a different amount of initial global cloud rotation, Ω_c, where the first row has no initial additional bulk rotation, shown at four different times; 0.6, 1.2, 1.7, and 2.1 Myr. The column densities are normalized to the same value, with sink positions overplotted as gray dots.

Initial angular momentum input in the form of an initial constant cloud angular velocity will spread filaments creating more diffuse areas of star formation (Figure 6.5). This will have less of an effect on random seeds that already produce distributed star forming filaments. For the intermediate resolution runs shown, increasing angular rotation means that fewer sink particles are formed at larger mean separations, producing less populated, more diffuse clusters. The median masses of the sinks and patches do not vary significantly for increased angular speeds. At the highest resolutions, rotation has a less pronounced effect on the numbers of stars formed (see

Table 6.1), but the stars are still farther apart than for non initially rotating cases.

6.4.2 Spin Alignment

The initial global rotation of the cloud actually leads to modest decreases in average protostellar core angular momentum compared to its total budget on account of decreasing the stellar density of the star forming environment; the consequences for the direction of the angular momentum vector are less clear. Throughout the accretion process, the orientation of the angular momentum axes of individual patches are highly variable. As such, we look at orientations of the entire patch ensemble as a collection of inclinations to determine if the direction of initial angular momentum input could get imprinted on the cluster. In Figure 6.6a we show the cumulative probability distribution functions (CPDF) for $\cos i$ of 9 selected high resolution runs near the end of their simulation times, where i is the inclination of the patch angular momentum axis relative to the axis of the initial angular momentum input for rotation frequencies of $\Omega_c^{-1} = 6$, 3, 1.5 Myr and a few non-rotating runs for comparison. The non-rotating clouds have modest initial angular momentum from the injection of turbulent energy at the start, which would correspond to an eddy turnover time of $\sim 10\,\mathrm{Myr}$ at cloud scales. Most of the runs, even those with modest amounts of initial global angular momentum input, are fairly consistent with an isotropic distribution of inclinations, uniform in $\cos i$. Using the K-S statistic, we can not reject the null hypothesis at a 95% confidence level for all runs in the sample. Only cases with the largest input of global cloud rotation are marginally consistent at a 90% confidence level, but they are also the runs that produce fewest sinks.

We fit the CPDF to a model which assumes a conical distribution of vectors about a line at an angle α from the assumed line of sight (which we take to be the axis of initial angular momentum input from the rotating runs) with a conical spread of λ, similar to form in Jackson & Jeffries (2010). Thus, if spin axes are randomly oriented, $\alpha = 0, \lambda = 90^\circ$. Using the python package emcee (Foreman-Mackey et al., 2013), we fit the average CPDF over the entire run time of simulations to models of $\cos i$. The models are generated according to the methods in Jackson & Jeffries (2010), where the final model is of the form $\cos i = \sin\alpha \sin(\cos^{-1}(1 - R(1 - \cos\lambda))\cos\phi + \cos\alpha(1 -$

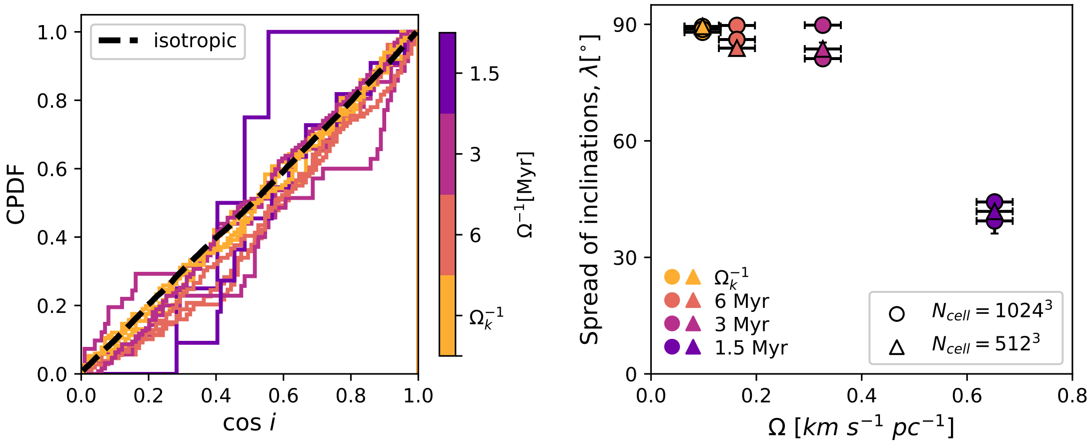

(a) (b)

Figure 6.6: Comparison of runs with varying amounts of initial global angular momentum. a) The cumulative probability distribution of cos i for 9 selected high resolution runs compared to the expected CPDF (black dashed line) for a completely random isotropic distribution of inclinations show that most rotating clouds still appear very isotropic. The lines are color-coded according to the initial amount of angular momentum input, where the orange lines correspond to those clouds that just have the base amount of turbulent input designated Ω_k^{-1}. b) The resultant fit of the spread of mutual inclinations for the different rotation inputs (color-coded to match the left panel) plotted against the initial angular speed including contributions from the turbulence at cloud scales, Ω_k, error bars show expected level of variation from different turbulent seeds. Fitting the average CPDF across all time for the spread in mutual inclination, λ, shows that all but the fastest rotating clouds are consistent with a cone angle of 90°, such that most are isotropically oriented with no mutual inclination. In summary, significant alignment of patch inclinations only occurs for the case with the fastest global initial rotation.

$R(1-cos\lambda))$ where R and ϕ are drawn from random distributions within $[0,1]$ and $[0,2\pi)$, respectively.

In Figure 6.6b, we show the results of the fits for the λ parameter for both the high and intermediate resolutions runs from which it is evident that for all but the most rapidly rotating clouds, the spread in distribution, λ is consistent with 90° and favors no mutual alignment among the cores. The fastest rotating cloud's speed is near break-up, where $1.5\,\mathrm{Myr}^{-1} \sim 0.65\,\mathrm{km\,s^{-1}\,pc^{-1}}$, which is considerably larger than typical values $\sim 0.05-0.2\,\mathrm{km\,s^{-1}\,pc^{-1}}$ for Milky Way giant molecular clouds (Imara & Blitz, 2011). While the $\cos i$ distributions remain nearly uniform for most clouds, the amount of retrograde orbits decreases with added rotation, where retrograde in this case refers to a core's rotation axis being opposite that of the initial rotation axis of the global cloud. This is consistent with a slight favoring of alignment with the global rotation axis, but would not be obvious from observations of just the inclinations.

6.5 Discussion

In the following we use our patches as proxies for protostellar cloud cores. While our patches are defined by fixed grid sizes rather than some density criterion, these sizes are comparable to those of cores in low-mass star-forming regions, and we showed in Kuznetsova et al. (2018) that patch masses are reasonable approximations for the self-gravitating mass surrounding sinks.

The median values of the specific angular momenta are consistent with those derived from measurements of velocity gradients in protostellar core observations at similar size scales, where at radii 0.05-0.1 pc the specific angular momentum from Goodman et al. (1993) would be on the order of 0.002-0.015 km s^{-1} pc or $0.6-4.6\times10^{21}$ cm^2 s^{-1}, compared to $j \sim 3.2-5\times10^{21}\mathrm{cm}^2\mathrm{s}^{-1}$ at the patch edge in our fiducial and intermediate resolution run. These comparisons yield a good agreement, with varying uncertainties in the observations likely due to projection effects (Zhang et al., 2018).

With reference to the distribution of angular momentum directions, there are numerous ways to infer the spin axis orientation of stars e. g. the orientation of outflows/jets (Stephens et al., 2017) or measuring both the period P and line of sight $v \sin i$ of magnetically active late-type stars (Jackson & Jeffries, 2010). Jackson & Jeffries (2010) posit that observations of mutual alignment of inclinations could yield information about the initial rotation of the star forming region. Yet, our results in Figure 6.6 show that unless the initial rotation is incredibly high, we would not expect to see obvious trends in the alignment of specific angular momentum axes. These results are fairly consistent with findings from Corsaro et al. (2017) and with the mostly random distribution of inclinations found in many star cluster and star forming regions (Jackson & Jeffries, 2010; Ménard & Duchêne, 2004).

Using the spin parameter, we find that core angular momenta in our simulations are on average $25-40\%$ of the maximum possible, and thus are dynamically important. With the core masses, radii, and specific angular momenta from Figures 1 and 5 in Offner et al. (2008) and performing the same procedure to compute the spin parameter for their cores, we find that the median value of the spin parameter at all scales for the undriven (as is the case in our study) turbulent case is 0.28, consistent with the low end of our simulations. The driven turbulent case creates cores that have far less of their angular momentum budget at small scales, with a median spin parameter of 0.07 across all scales. At our intermediate patch scale (~ 0.1 pc), the values of the spin parameter and angular momenta of both the undriven and driven cases in Offner et al. (2008) are both consistent with our distributions. However, at higher resolution for patch sizes of 0.05 pc, the driven turbulence case has a median $\lambda_s \sim 0.1$, diverging from our results, the effects of driven turbulence start becoming significant at core scales $r_p \lesssim 10^4$ AU.

6.5.1 Local Generation of Angular Momentum

We suggest that the best explanation of where cores get their angular momentum that explains the results of the parameter study is one in which gravitational interactions between gas overdensities, including dense cores designated by the sink+patch construction, impart the initial angular momentum to the core. Our argument in favor of local generation of angular momentum rests on two observations that make inheritance of initial angular momentum unlikely: one, that the directions of core angular momenta are not correlated with any specific direction, including that of the initial global angular momentum of the cloud (Figure 6.6); and two, that the specific angular momenta increase with increasing density of sinks (and thus closer separations) (Figure 6.4) , as one might qualitatively expect for local torquing. There is more than enough force in gravitational interactions for small scale overdensities to create torques; and if the overall spatial density of sinks decreases and density fluctuations were smeared out, one could expect lower values of angular momentum as gravitational interactions must act over a greater distance.

The results of varying the initial cloud rotation (Figure 6.5), show that effect of varying the initial global cloud angular velocity Ω_c is the total number and spatial density of the gas and sinks, where the global cloud rotation tends to shear out a portion of the gaseous overdensities, producing more diffuse, less embedded clusters. The angular momentum content of the sinks depends on the star forming environment rather than the initial angular momentum content of the cloud. Increasing the global angular momentum content of the cloud does not pass down to the sinks; in fact, the average angular momentum content decreases with increased initial cloud rotation. In Figure 6.4 for example, the intermediate resolution runs with $N_{cell} = 512^3$ are arranged in the order of their initial cloud angular momentum, with the lowest $\langle n_s \rangle$ corresponding to the highest initial rotation speed.

As a caveat, similar amounts of rotation input will affect the stellar densities of clusters differently depending on the resolution and geometries generated by the random seed for the turbulence. Higher resolution runs produce more sinks as the amount of resolved overdensities will increase in an isothermal simulation such as ours. However, increased initial global rotation will still produce more diffuse clusters and filaments as it slows the collapse of the cloud. The local filamentary environment seems to play an important role in the properties of protostar populations, particularly when it comes to the starting ingredients of protostellar disks.

Our construction of the spin parameter is based on the metric used for characterizing the angular momentum content of cold dark matter haloes in cosmological simulations, where the spin parameter is the ratio of the angular momentum to the maximum amount possible at the virial radius of the halo. On the side in favor of local angular momentum generation, we make an analogy with dark matter simulations (Bullock et al., 2001, e.g.) which argue that a combination of tidal torques and mergers produce the halo spin parameter distributions, which are log normal just as ours are.

The (initial) injection of turbulence at small scales could be thought to be responsible for imparting the initial angular momentum to the cores. However, the nature of the turbulent power law power spectrum, such as the $P(k) \propto k^{-4} dk$ used here, means that there will inherently be less energy and angular momentum at smaller scales. A conservative order of magnitude calculation of the angular momentum of an eddy on the patch scale $\sim 0.05 - 0.1$ pc, assuming that the eddy frequency $\Omega_k \propto k^{-1/2}$, where the largest scale fluctuation frequency matches that of an eddy with a speed of Mach 8, $\Omega_k^{-1} \sim 10$ Myr, results in an angular momentum $j = 2/5 R^2 \Omega \sim 10^{20} - 10^{21}$

cm^{2}s^{-1}, which is roughly an order of magnitude below the minimum angular momentum seen in the fiducial run, thereby not enough to generate the typical values of the core angular momentum in the simulation. In addition, runs across the parameter space all have the same turbulent energy initially injected, thus, the angular momentum across the runs of varying global cloud rotation speed should, at the very least, remain fairly constant if angular momentum were directly inherited from the turbulent eddies.

In contrast, Burkert & Bodenheimer (2000) and Chen & Ostriker (2018) argue that the core angular momenta are inherited from turbulence. In the former case, the absence of self-gravity (A. Burkert, personal communication) means that the imposed turbulent velocity field is the only possible source of angular momentum. In the latter case, the small scale (1 pc) of the simulation requires the imposition of prescribed inflows and turbulent motions (see Chen & Ostriker, 2015) which in our case arise naturally from gravitational collapse from larger scales, seeded by overdensities created by the rapidly-decaying initial turbulence. Our simulations may also exhibit stronger gravitational driving because Chen & Ostriker (2015); Chen & Ostriker (2018) evaluate core properties at the onset of collapse of the most evolved core, whereas we can follow the evolution through sink formation and accretion.

6.5.2 Implications for Disk Formation

Angular momentum is a requirement for disk formation and many models of disk formation and evolution will assume an accretion of angular momentum by the protostar from the surrounding cloud like in Terebey et al. (1984), where rotating collapse grows a disk by depositing material at the centrifugal radius, $r_c = j^2/GM$. For simplicity, these models assume a constant angular velocity cloud from which angular momentum is inherited as the accretion radius of the protostar grows and material falls in from farther away. The angular momentum then depends directly upon the angular velocity of the cloud. Using the TSC model as an example framework, these assumptions will lead the specific angular momentum to grow like $j \propto t^2$, or the spin parameter $\lambda_s \propto t^{3/2}$. However, seen in Figure 6.3, the mean of the sink specific angular momenta does not significantly change with time. The lack of change in sink angular momentum content suggests that mass infall to disks will weight outer regions more heavily than in the TSC model. Previous studies show that infall to larger disk radii may also help trigger gravitational instabilities (e.g., Zhu et al., 2012).

The accretion of angular momentum in our simulations is not a smooth monotonic process. This already challenges the standard ideas of what the initial conditions for disk formation and evolution should look like. We conduct a case study by looking in detail at the dynamics of the gas entering and leaving one particular sink-patch system. In Figure 6.7, we show the mass flux entering the patch through the individual faces of the patch and compare it to the total inward mass flux across the patch. At times, there is no net mass flux into the patch at all and the accretion has an episodic quality, where several different epochs of mass flux inward can be identified in Figure 6.7, annotated with arrows marking the timestamps of the snapshots plotted in Figure 6.8.

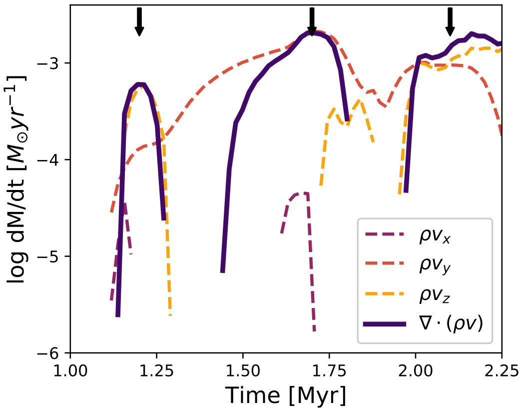

Figure 6.7: Net mass flux into the patch in three orthogonal directions (dashed lines) and the total mass flux into the patch (violet line). The magnitude of the mass flux plotted is normalized such that the integrated amount under the curve matches the patch mass at the end of the simulation in order to account for material that does not become bound to the sink and leaves the patch. The arrows annotate specific times of high inward mass flux at 1.2, 1.7, and 2.1 Myr that are shown as column snapshots in Figure 6.8. Note that material at each high flux event primarily comes in from different directions.

In this example, it is possible to connect the interactions of the sink-patch system with its environment to specific accretion epochs. In the first epoch, at 1.2 Myr into the simulation, the sink accretes from a flow of gas falling into a filament, however, by 1.7 Myr, the sink and filament have come together and the sink is embedded while gas flows along the filament, onto the sink.

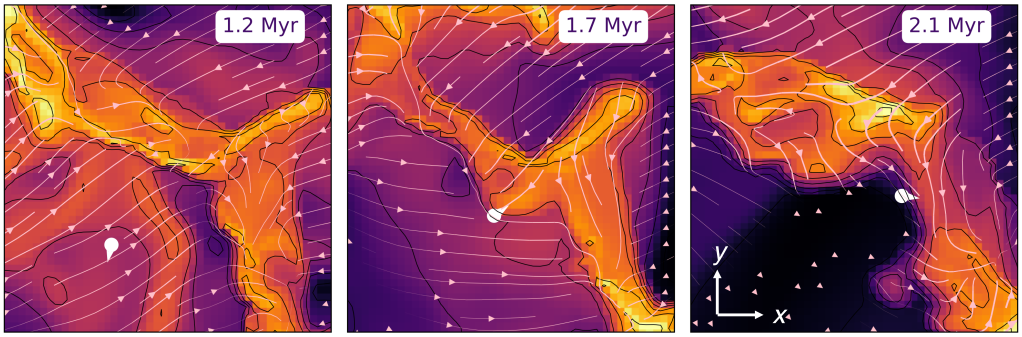

Figure 6.8: Column densities summed over 0.5 pc of the same 2 pc × 2 pc region taken at the times corresponding to the high mass flux events of the sink-patch system annotated in Figure 6.7; 1.2, 1.7, and 2.1 Myr. The sink-patch system is shown as a white marker with an arrow indicating its motion in the plane of the image, the background streamlines show the flow of material within the region. During the three frames, the sink's accretion events are at first dominated by flow into the filament, then flow along the filament as the sink becomes embedded within, and finally the flow directed toward the sink as the sink becomes large enough to deplete some of the filament gas. The surrounding environment is heterogeneous – lumpy, and accretion is dominated by these irregularities.

The filament itself is not a smooth object, but quite lumpy. At 2.1 Myr, the sink has quickly accreted a large clump from the filament and is accreting the next nearby overdensity. This example demonstrates how a dynamic clump-filled environment in which gravity dominates the dynamics naturally lends itself to episodic core accretion, in which infall onto the core is not isotropic, but dominated by the direction of flows in the environment.

In our case, non-isotropic infall can explain why the specific angular momentum of sinks does not evolve over time. In Figure 6.9, we plot the relative changes in the magnitude and direction of the specific angular momentum, as well as the relative changes in the total mass enclosed in the patch for sinks between outputs taken every 0.02 Myr as probability density functions. Looking at the changes in angular momentum for the cores, it is easy to see why the total angular momentum of the cores does not show smooth growth over time – cores are about just as likely to gain angular momentum as they are to lose it. This type of behavior is a natural consequence of episodic filamentary, non-isotropic accretion we show in Figure 6.7, most commonly when material is accreted from many different directions such that the mass of the patch grows, the direction of the angular momentum vector for the sink changes, but the total sink angular momentum will fluctuate about a value.

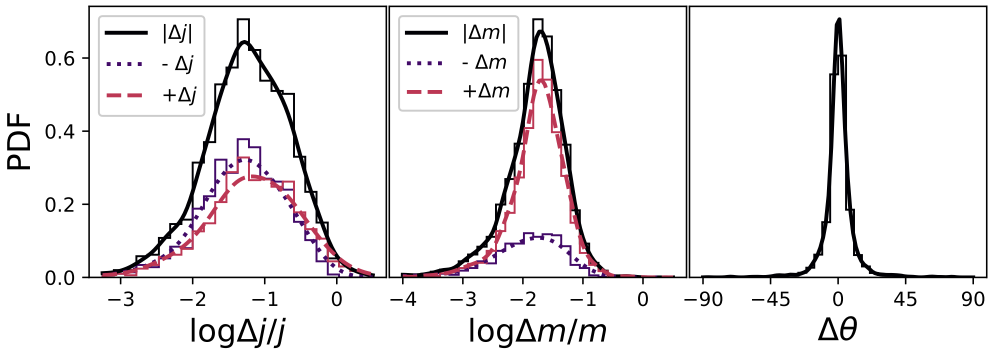

Figure 6.9: From left to right: Probability density functions of relative changes in patch specific angular momentum, mass, and direction of angular momentum between data outputs for the intermediate resolution run shown in Figures 6.7 and 6.8, at a cadence of 0.02 Myr between outputs. Left: The magnitude of the relative change in angular momentum (black solid line) is a skewed Gaussian centered at $\lesssim$ 10 % of the previous angular momentum. The pink dashed line represents increases in the angular momentum while the violet dashed line represents total decreases in the angular momentum. Center: The magnitude of the change in mass peaks at $\sim$ 0.02 %, but most changes are accretion events rather than material flowing out of the patch. Right: Change in total angular momentum direction is centered at 0, as changes in direction require large relative changes in specific angular momentum.

The simple picture in which smooth spherical infall of rotating material builds up a disk may require revision. A more time-dependent, filamentary-type of infall may have implications for making disks more susceptible to gravitational instability from episodes of mass-loading.

6.6 Summary

Our simulations of protostellar core formation in a globally-collapsing molecular cloud show that the angular momenta of individual cores are not strongly affected by global cloud rotation. Instead, the angular momenta appear to be generated by local torques from other cores and density concentrations. Unlike often-used models for protostellar collapse, the external medium that can be accreted is generally not in solid body rotation around the central sink, resulting in nearly constant specific angular momenta as the protostellar core (sink-patch in our calculation) grows. As seen in other simulations such as those of Bate (2018), we find considerable time variability in the accretion of the angular momenta and mass, which is the product of a lumpy episodic non-isotropic accretion of material onto the protostellar cores.

The results presented in this paper constitute the first stage of our program, which next will consider the effects of magnetic fields, with the ultimate goal of developing more physically-realistic angular momentum distributions that can be used as inputs to models of protostellar and protoplanetary disk formation and evolution.

6.7 Acknowledgements

This work was supported by NASA grant NNX16AB46G and by the University of Michigan, and used computational resources and services provided by Advanced Research Computing at the University of Michigan, Ann Arbor and the University of North Carolina at Chapel Hill Research Computing group.

CHAPTER 7

Angular Momenta, Magnetization, and Accretion of Protostellar Cores

This chapter has been accepted for publication in the Astrophysical Journal (Kuznetsova et al., 2020). This work was co-authored with Lee Hartmann and Fabian Heitsch. The paper is reproduced here with minor stylistic revisions.

7.1 Abstract

Building on our previous hydrodynamic study of the angular momenta of cloud cores formed during gravitational collapse of star-forming molecular gas in Kuznetsova et al. (2019), we now examine core properties assuming ideal magnetohydrodynamics (MHD). Using the same sink-patch implementation for the *Athena* MHD code, we characterize the statistical properties of cores, including the mass accretion rates, specific angular momenta, and alignments between the magnetic field and the spin axis of the core on the 0.1 pc scale. Our simulations, which reproduce the observed relation between magnetic field strength and gas density, show that magnetic fields can help collimate low density flows and help seed the locations of filamentary structures. Consistent with our previous purely hydrodynamic simulations, stars (sinks) form within the heterogeneous environments of filaments, such that accretion onto cores is highly episodic leading to short-term variability but no long-term monotonic growth of the specific angular momenta. With statistical

characterization of protostellar cores properties and behaviors, we aim to provide a starting point for building more realistic and self-consistent disk formation models, helping to address whether magnetic fields can prevent the development of (large) circumstellar disks in the ideal MHD limit.

7.2 Introduction

While magnetic fields in the interstellar medium are clearly dynamically important at low densities (see review by Crutcher, 2012), their importance in high-density regions of molecular clouds, and thus on the formation of stars and circumstellar disks, is less clear. Observations on scales of $\sim 0.1-10$ pc (e.g., Crutcher, 2012; Palmeirim et al., 2013; Planck Collaboration et al., 2016) show that magnetic fields are important in forming filaments, as suggested by preferential orientation of filaments perpendicular to fields.

In addition, recent calculations of protostellar core collapse have proposed that magnetic fields could restrain or even prevent protoplanetary disk formation by transporting large amounts of angular momentum outward- the so-called "magnetic braking catastrophe" (Mellon & Li, 2008).

Exactly how effective magnetic fields are in suppressing disk formation depends upon a variety of parameters, in addition to the possible importance of non-ideal magnetohydrodynamic (MHD) effects. The simulations suggest that the amount of magnetization μ - the mass-to-flux ratio (M/Φ) over the critical value, $(M/\Phi)_{crit} = 1/2\pi\sqrt{G}$ (for a sheet; Nakano & Nakamura, 1978) - and the geometry of the magnetic field, especially relative to the angular momentum vector, determine the frequency, shape, and size of protoplanetary disks that can form (Joos et al., 2012; Li et al., 2013; Krumholz et al., 2013). It seems that without the dissipation of magnetic flux, whether through ambipolar diffusion (Mellon & Li, 2008; Vaytet et al., 2018), or other non-ideal effects such as the Hall effect (Wurster et al., 2018), a protostellar core with an initially strong magnetic field that is aligned with the primary rotation axis may not be able to form disks having sizes large enough to explain observations (e.g., Tobin et al., 2012; Ohashi et al., 2014). Turbulence in the protostellar core as a cause of misalignment (Joos et al., 2013; Gray et al., 2017), reconnection diffusion of the magnetic field (Santos-Lima et al., 2013), or as a method to halt the production of large toroidal components responsible for braking (Seifried et al., 2012) has also been previously suggested as a means of reconciling magnetized disk formation.

The median magnetization parameter of cores derived from Zeeman effect measurements in the interstellar medium is estimated to be $\mu \sim 2$ (Crutcher, 2012), indicating that fields are dynamically important. Observational constraints on the relative directions of magnetic fields and angular momenta, assuming that the latter are given by the positions of bipolar outflows, suggest random alignment, at least on 1000 AU scales (see review by Hull & Zhang, 2019).However, Krumholz et al. (2013) contended that at that magnetization even with a random distribution of angles between the magnetic field and angular momentum vector, the disk frequency would still be limited to 10-15%, much lower than the observed Class II disk fraction.

Top-down cluster formation simulations, starting with the progenitor molecular cloud down to protostellar core and disk scales, can connect the conditions of star forming environments to disk formation scenarios (Kuffmeier et al., 2017; Bate, 2018) and produce statistical descriptions of protostellar properties and behaviors (Kuznetsova et al., 2018; Kuznetsova et al., 2019). Top-down simulations can also characterize the multi-scale behavior of magnetic fields during star formation. Connecting large scale behavior with properties on the core scale can provide realistic initial conditions for core collapse and disk formation studies (e.g. Bhandare et al., 2018) , given the inherent ambiguities between scattering effects and the magnetic field geometry seen in disk scale polarization studies (Kataoka et al., 2015; Yang et al., 2016).

In this chapter, we present results of ideal magnetohydrodynamic (MHD) simulations performed with the grid code *Athena*. Large scale magnetic field behavior follows the weak-field model in which magnetic fields play a role in assembling material on large scales and statistical analysis of filament and magnetic field orientation is in agreement with findings from observed young star forming regions (Planck Collaboration et al., 2016). We find that the presence of magnetic fields slows star formation compared to the purely hydrodynamic case, but given the weak initial field, gravity remains the primary driver of star formation leading to the formation of supercritical cores. On core scales, we find similar mass and angular momentum accretion behavior to our hydrodynamic simulations in Kuznetsova et al. (2018); Kuznetsova et al. (2019). As in Kuznetsova et al. (2019) (KHH19), we find that the accretion of angular momentum is episodic and highly variable over short time scales, but appears constant when time averaged. The addition of magnetic fields in this work was found to dampen the amplitude of variability in the specific angular momentum.

Our simulations provide an important comparison to newly released work (Wurster et al., 2019), in that we use a completely different numerical method (fixed grid in our case vs. SPH in (Wurster et al., 2019)), and the larger number of cores in our work provide a more complete statistical characterization of core angular momenta and magnetizations for use by simulations of protostellar core collapse on smaller scales.

7.3 Method

We use a version of the Eulerian grid code *Athena* (Stone et al., 2008), modified with a sink-patch implementation described in Kuznetsova et al. (2019) and an RK3 integrator (Gottlieb & Shu, 1998), to simulate star cluster formation from the progenitor molecular cloud. The basic numerical setup and details of the sink-patch implementation are described in (Kuznetsova et al., 2018; Kuznetsova et al., 2019), so we provide only a short summary here.

We solve the system of equations

$$\begin{aligned}
\frac{\partial\rho}{\partial t}+\nabla\cdot(\rho\mathbf{v}) &= 0 && (7.1)\\
\frac{\partial\rho\mathbf{v}}{\partial t}+\nabla\cdot(\rho\mathbf{v}\mathbf{v}-\mathbf{B}\mathbf{B}+P+\frac{\mathbf{B}\cdot\mathbf{B}}{2}) &= -\rho\nabla\Phi && (7.2)\\
\frac{\partial\mathbf{B}}{\partial t}-\nabla\times(\mathbf{v}\times\mathbf{B}) &= 0 && (7.3)\\
\nabla\Phi &= 4\pi G\rho && (7.4)
\end{aligned}$$

in the ideal MHD limit. The equation of state is isothermal such that $P = c_s^2\rho$. The Poisson equation (eq. 7.4) is solved every RK3 substep, using the FFT solver that comes with version 4.2

of *Athena*.

The sink-patch, which acts as the accretion reservoir for the sink particle, is defined by its accretion radius r_{acc} such that it contains $(2r_{acc}+1)^3$ cells, centered on the location of the sink particle, redrawn at every timestep. Derived quantities are calculated on the boundary of the sink-patch.

Conserved variables were output for the patch cells and an additional boundary cell. Angular momentum is calculated as a cumulative sum over the patch cells, $\mathbf{L} = \Sigma_i m_i \mathbf{v}_i \times \mathbf{r}_i$, where the velocity $\mathbf{v}_i$ and radius $\mathbf{r}_i$ are taken with respect to the sink's velocity and position, respectively. Specific angular momentum is then defined as $\mathbf{j} = \mathbf{L}/\Sigma_i m_i$. Fluxes of quantities into the sink-patch system were measured across the inner faces of the boundary cells, with information separable into orthogonal components such that the directional information of accretion onto the patch could be tracked. Sinks that have entered one another's patches and merged, or those liable to fragment under the conditions outlined in KHH19 are removed from the analysis.

The initial conditions are that of a 4 pc radius spherical cloud in a 20 pc box at an isothermal temperature of $T = 14$ K, the same as those used in Kuznetsova et al. (2018) and Kuznetsova et al. (2019), with the addition of a 5 μG uniform field. The exception to these conditions is run IR_b0, which is purely hydrodynamic for comparison. We adopt an intermediate resolution (as designated in KHH19) of $N_{cell} = 512^3$ where $\Delta x = 0.04$pc, such that all of the runs in this chapter have a patch radius of $r_p = (r_{acc} + 1/2)\Delta x = 0.1\,\text{pc}$. As the simulation has an isothermal equation of state, results can be rescaled to another family of solutions, preserving the sound and Alfven speed, by scaling temperature, distance, time, magnetic field strength, and mass by the same factor.

Table 7.1: List of run properties for the cores used in this study.

Run	Seed	Ω_k [km s^{-1} pc^{-1}]	$\mathbf{B_0}$ [μG]	N_{sink}
IR_b0	0	0.07	$\langle 0,0,0 \rangle$	108
IR_bx5	3	0.03	$\langle 5,0,0 \rangle$	45
IR_bx5_s1	1	0.13	$\langle 5,0,0 \rangle$	17
IR_bx5_s2	2	0.03	$\langle 5,0,0 \rangle$	9
IR_by5_s1	1	0.13	$\langle 0,5,0 \rangle$	15
IR_by5_s2	2	0.03	$\langle 0,5,0 \rangle$	35

The ambient density exterior to the initial spherical cloud is $\rho_0 = 1.5 \times 10^{-23}$ g cm^{-3}, where $\rho_c = 100 \times \rho_0$, such that the initial cloud free-fall time is $t_{\rm ff} = 1.7$ Myr and initial cloud mass is ~ 5900 M$_\odot$. Turbulence is seeded at the start with a Mach 8 velocity spectrum $P(k) \propto k^{-4} dk$ which introduces both overdensities and a base level of cloud scale angular momentum, $\Omega_k = 0.07 \pm 0.05$ km s^{-1} pc^{-1} or $j = 1.58 \times 10^{23}$ cm^2 s^{-1} on average. Several turbulent realizations are used for the purpose of generating better core statistics. Details of all the runs are listed in Table 7.1.

7.4 Results

The initial perturbed cloud conditions are such that the virial parameter $\alpha_{vir} \lesssim 1$ on the cloud ($r \sim 4$ pc) scale. As collapse proceeds, the onset of sheet/filament formation creates dense structures that become the sites of later sink formation (Figure 7.1). The simulations are evolved for up to one initial free-fall time ($t_{\rm ff}$ = 1.7 Myr). Run IR_by5_s2 was evolved the furthest in time and produced the most sinks; we use it as the fiducial run for all cloud and filament scale analysis, unless otherwise stated. Statistical properties cores in subsection 7.4.2.1 come from the full series of runs, and datasets are stacked where indicated.

In Figure 7.1, we show the progression of cluster formation in run IR_by5_s2 as a series of snapshots in time of column densities and sink locations, in three orthogonal projections. The first two columns in Figure 7.1 show the filament's long axis, while the line of sight of the $x-y$ plane projection in the third column is preferentially along the elongated axis of the filament, that is, viewed more or less 'down the barrel'. Thus, elongated features in the $z-y$ and $x-z$ planes are indicative of filament formation, but the appearance of non-spherical features and groupings in the last projection are more likely to be the result of projection effects, rather than co-spatiality.

7.4.1 Global Magnetic Field Behavior

An important test of our magnetic simulations is whether they are consistent with the observed variation of magnetic field strength with gas density. Figure 7.2 shows the results from the sim-

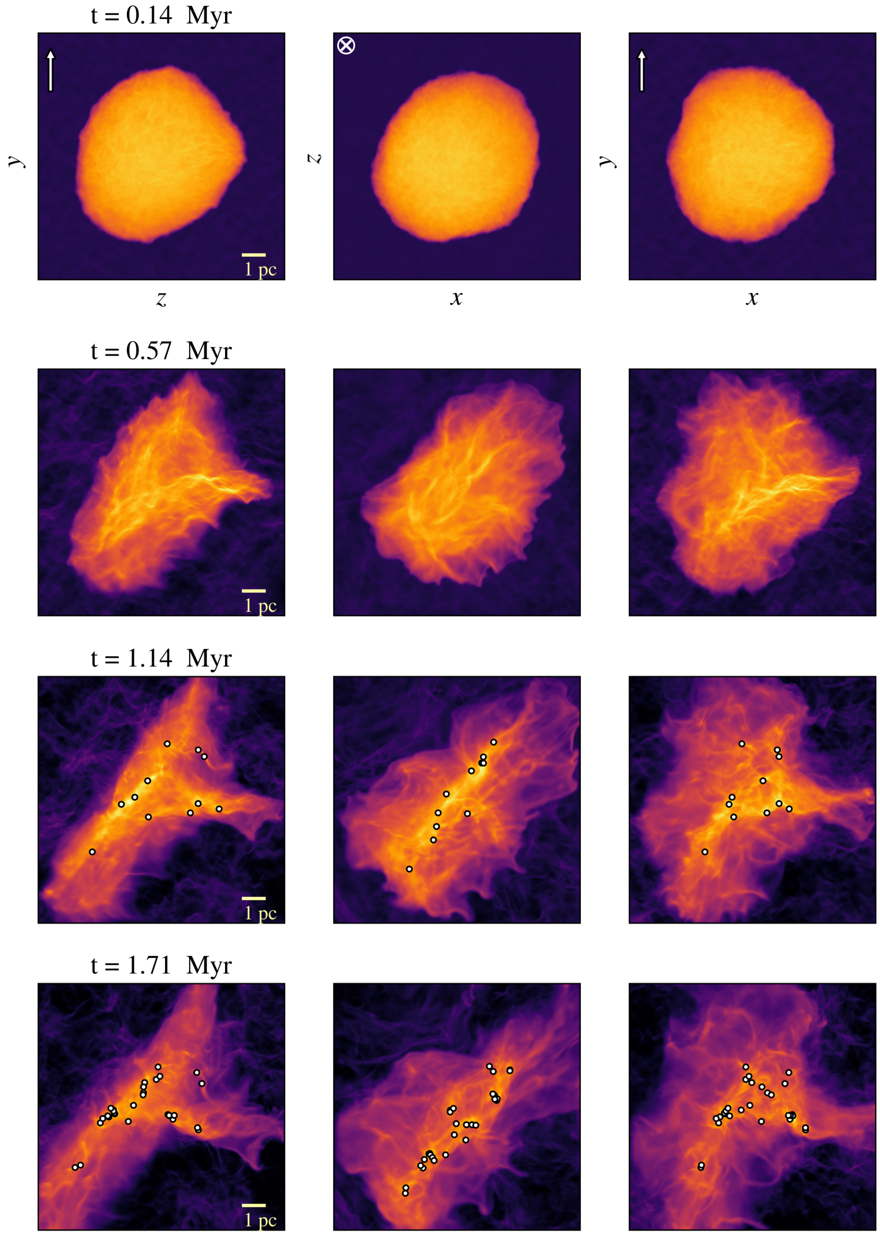

Figure 7.1: Evolution of column density of run IR_by5_s2 through to one free-fall time, shown at t = 0.14, 0.57, 1.14, and 1.71 Myr at three orthogonal directions, labeled in the top-most row. Arrows and ⊗ shapes in the top-most row show the initial uniform magnetic field direction for each projection. Locations of sink particles are shown as white markers. Box shown is the inner 6pc × 6pc of the domain, centered on the cloud; scale bar denotes 1 pc.

ulations, with number densities smoothed over 0.1 pc (consistent with our effective numerical resolution), along with the median total magnetic field in each density bin. The total magnetic field strength is largely independent of number density n_H, consistent with the initial magnitude of

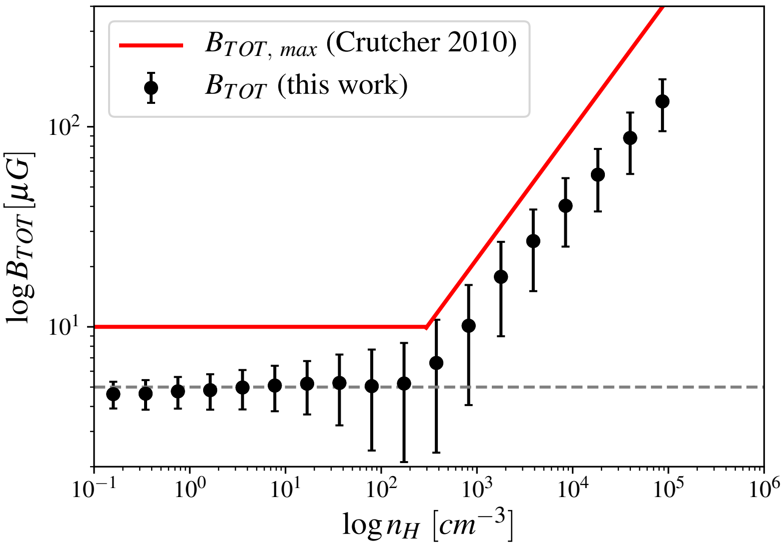

Figure 7.2: Median total magnetic field strength, B_{TOT} within the respective binned number densities n_H. Binned cell averages are shown as black markers with error bars representing the standard deviation within the bin. The upper limit for the magnetic field, $B_{TOT,max}$, from Crutcher et al. (2010) is shown in red. The gray dashed line is the initial magnitude of the magnetic field $B_0 = 5\ \mu G$.

the magnetic field $B_0 = 5\ \mu G$, until densities of $n_H \sim 300 - 400\ \mathrm{cm}^{-3}$, beyond which the median total magnetic field increases rapidly with increasing density. The results are consistent with the maximum total magnetic field values as a function of density found by Crutcher et al. (2010) from a Bayesian analysis of Zeeman observations of nearby clouds. The simulations are also consistent with the observational inference of a wide spread in magnetic field strengths at a given density (see discussion in Crutcher, 2012). We find a slope of median field strengths $B \sim n_H^{0.56}$ which is slightly flatter than the observationally estimated slope 0.65 ± 0.05 for the maximum field strength Crutcher (2012), but this may be affected by limited resolution at the highest densities.

During global cloud collapse, magnetic fields aid in the collection of material into dense structures (filaments). When filaments become massive enough, they begin to influence the magnetic field geometry; U-shaped bends around filaments as field lines get dragged in toward high density regions are particularly visible in the $y - z$ and $z - x$ projections at 1.71 Myr in Figure 7.3. Smaller striation-like features tend to lie preferentially along the field lines, perpendicular to the main filament axis.

We computed histograms of relative orientation (HROs) between the iso-column density con-

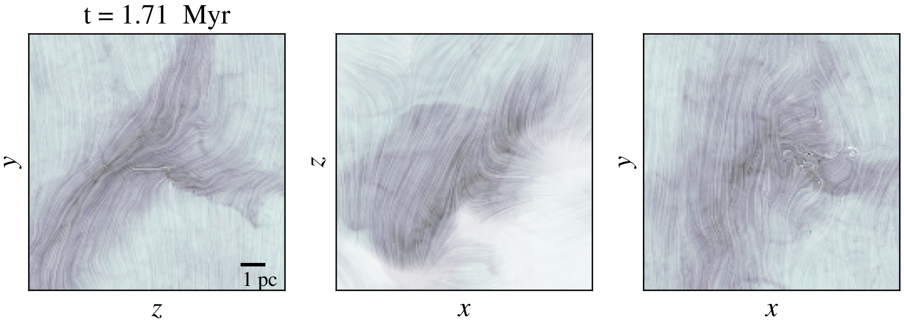

(a)

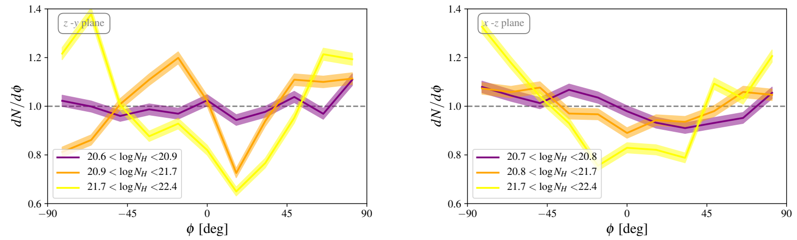

(b) (a)

(c) (b)

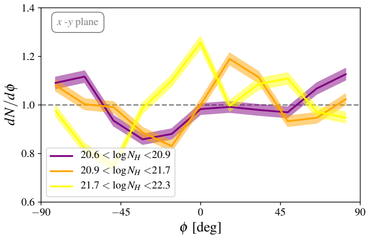

(d) (c)

Figure 7.3: Magnetic field geometry computed as (Top row) a line integral convolution (LIC), computed with the `LicPy` package, of the magnetic field shown on top of the column density in three projections at 1.71 Myr for run IR_by5_s2. Low-magnitude small scale noise in the LIC is smoothed and masked to appear as opaque regions in the map. The box sizes are 6 pc × 6 pc of the simulation domain centered on the cloud. The initial magnetic field is uniform in the y-direction for this run. (Bottom row) Histograms of relative orientation (HRO) between the magnetic field direction and lines of isodensity computed using three different column density projections (smoothed to a resolution limit of ~ 0.4 pc) in the (a) $z-y$ plane (b) $x-z$ plane (c) $x-y$ plane. Each line corresponds to the range of column densities at the 68th (purple), 90th (orange), and 98th (yellow) percentile level for each projection, with the same number of samples (~ 20000), binned in increments of 15°. The error due to binning σ_h is represented by the shaded contours for each line. The value of $dN/d\phi$ is normalized with respect to the expected amount of samples in each bin if the distribution of relative orientations were uniform.

tours and the plane of sky magnetic field in three different orthogonal projections (Figure 7.3a-c). (Details for the calculation of the HROs based on the methods outlined in Planck Collaboration et al. (2016) are given in Appendix B.1. The HROs show that the highest density structures (filaments) are preferentially perpendicular to large scale magnetic fields, consistent with *Planck* observations (Planck Collaboration et al., 2016, see Figures 3, 5, and 8 in). This suggests that regions in which there is no preferential anti-alignment detected in the HRO diagram could have a viewing geometry that misrepresents the degree of elongation or filamentary structure seen in column density maps. Thus, filaments are formed roughly perpendicular to the magnetic field, the original field orientation helping to seed the morphology of the final structure. In our simulations, this process works likely in combination with the initial turbulent field's largest scale fluctuations, which played a role in setting the filamentary morphology of the purely hydrodynamic runs (Kuznetsova et al., 2019).

7.4.2 Properties on the Core Scale

Individual sink-patch systems also exhibit the density and magnetic field scaling law seen in Figure 7.2. In Figure 7.4a we show the relationship between the line of sight column density N_{H_2} and the total magnetic field B_{TOT} for a sample projection of the simulation cube, with colored circles denoting values taken at the locations of the sink-patches ("star-forming cells"); the star-forming cell values are computed as averages across the projected line of sight sink-patch cells and B_{TOT} is a mass weighted average across the patch cells. (We use the patches as equivalent to molecular cloud cores– see discussion in Kuznetsova et al. (2019)). Each sink-patch system has a volumetrically- determined magnetization, μ_{3D}, using the enclosed mass within the patch cells M_p and the average flux through the patch surface as the dot product of the three averaged components of the patch with their areas $\Phi = \mathbf{B} \cdot dA$, indicated by their color. For comparison we also compute an "observational estimate" of the critical ratio, using the relation $\mu_{2D} = N_{H_2}(7.6 \times 10^{-21})/B_{TOT}/M/\Phi_{crit}$ (Crutcher, 2004), where the column density is in cm^{-2} and inferred total magnetic field is in μG.

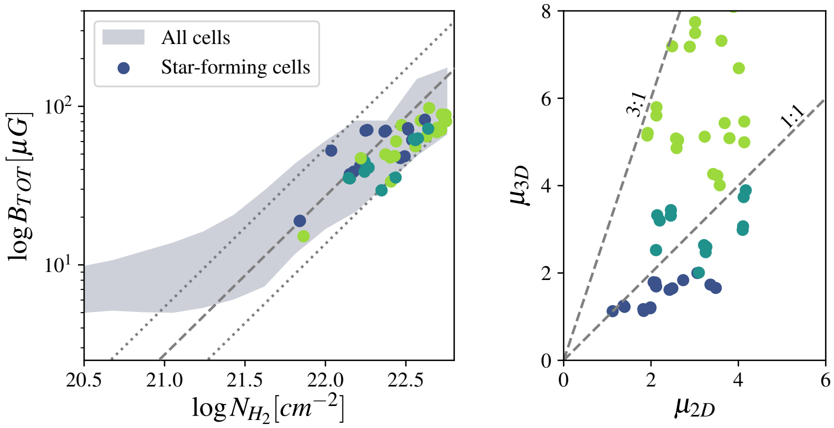

Figure 7.4: (Left) Total magnetic field strength, $\log B_{TOT}$ vs column densities, $\log N_{H_2}$ of all cells in the cloud (gray region) and just the star forming cells – those averaged across the sink-patch system (colored circular markers). Lines of constant magnetization $\mu_{2D} = 1, 4$ are the upper and lower bounds indicated by the dotted line, with the $\mu_{2D} = 2$ dashed line in between, computed from Crutcher (2012). Star-forming cells are binned by their true mass to flux ratios over the critical value μ_{3D}, computed with the mass contained within the patch and the flux through the patch surface; colors correspond to values in the right plot: light green - $\mu_{3D} > 4$, teal - $2 < \mu_{3D} < 4$, dark blue - $1 < \mu_{3D} < 2$, and purple - $\mu_{3D} < 1$. Right: Comparison of the observed magnetization from a projection, μ_{2D}, using relation from Crutcher (2012) vs the volumetrically derived magnetization, μ_{3D}.

All sink patches are magnetically supercritical, spanning a range $1 \lesssim \mu_{3D} \lesssim 8$, and lie in the region of magnetic supercriticality for $\log N_{H_2} \gtrsim 21.5$. In contrast, the“observationally” determined magnetizations are $1 < \mu_{2D} < 4$ (Figure 7.4b). Thus, μ_{2D} can underpredict the values of μ_{3D} in our sample cloud cores by factors of $2-3$. A small part of the discrepancy may come from the inferred cloud geometry (taken from Mouschovias & Spitzer, 1976); the rest probably lies in underestimates of the mass of the patch from the average line of sight column density, or in the differences between using the average total magnetic field B_{TOT} and decomposing directional components to calculate the flux Φ.

7.4.2.1 Core Angular Momenta and Magnetic Fields

To statistically characterize core properties at the 0.1 pc scale, we construct a sample of sink-patch systems from every MHD run, all taken at the same respective core ‘age’ of 50,000 years, the time elapsed since each sink’s respective formation time. All quantities, unless otherwise

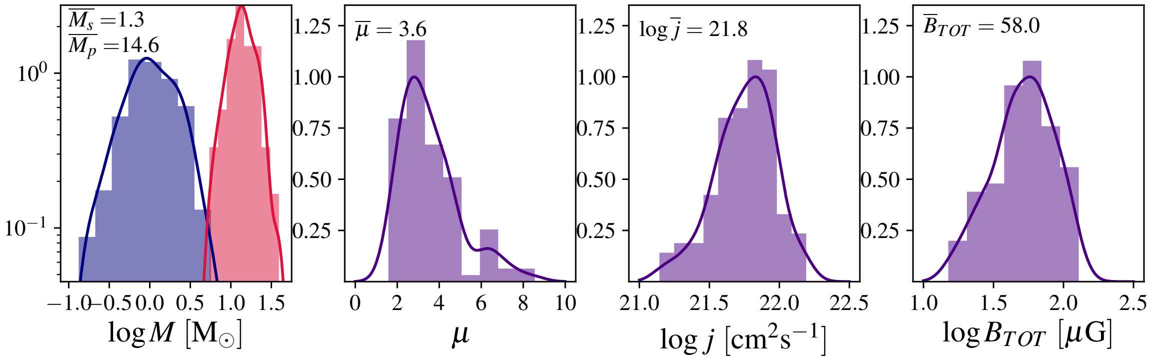

Figure 7.5: Distributions of core properties from left to right: mass functions for the sink mass, M_s, (blue) and patch gas mass M_p (red), mass to flux ratio relative to critical, μ, specific angular momenta, $\log j$, and total average magnetic field $\log B_{TOT}$. A total of 112 cores stacked from all the MHD runs 50,000 years after their sink formation time in the simulation were used in the sample.

stated, are integrated across the entire sink-patch.We show the distributions of sink and patch gas masses, their magnetizations, the specific angular momenta, average total magnetic fields, and their probability distribution functions computed from Gaussian kernel-density estimates in Figure 7.5. The kernel-density estimates are calculated using the `scipy.stats` Gaussian kde method and the resulting probability density functions are available in the supporting data.

Average core angular momenta are $j = 6.3 \pm 1.0 \times 10^{21}$ cm^{2}s^{-1} for the magnetic runs vs $j = 5.3 \pm 0.8 \times 10^{21}$ cm^{2}s^{-1} in the hydrodynamic case. As in the hydrodynamic case, the time evolution of average core specific angular momenta is flat and spin axis distributions are consistent with an isotropic distribution. The directions of core magnetic fields do not appear isotropic, and tend to be perpendicular to the filament orientation, as is the case for the larger scale fields (Figure 7.3). This alignment suggests that the core fields inherit much of their orientation from larger scales.

As in the purely hydrodynamic (HD) case, cores are just as likely to be spun up or down after accretion events, leading to a flat specific angular momentum over time (see Figure 3 in Kuznetsova et al. (2019) for more details). The magnitude of the specific angular momentum over time is highly variable over short time scales in the purely HD case; this variability is slightly dampened in the MHD case. Short-term variability in the magnitude of the specific angular momentum is correlated with changes in the direction of the angular momentum vector, which peak around

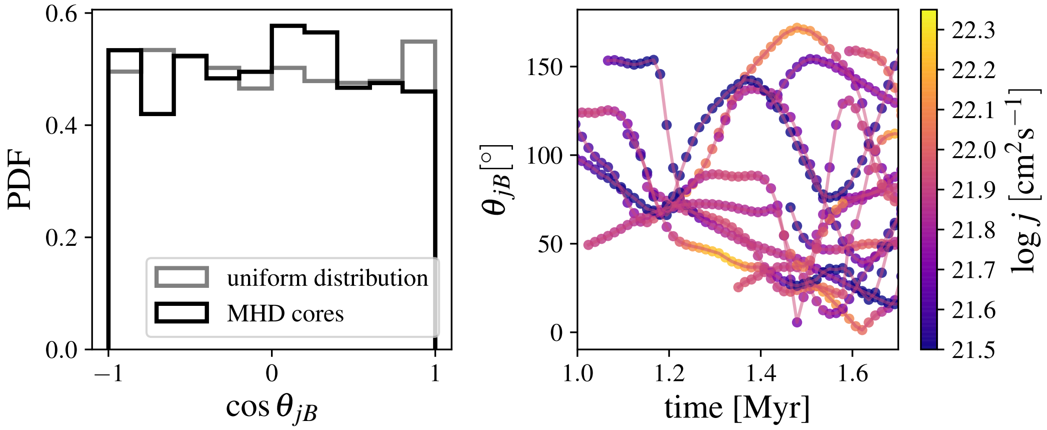

Figure 7.6: Behavior of the relative angle between the specific angular momentum vector and magnetic field direction θ_{jB}. (Top) Distribution of $\cos\theta_{jB}$ for all cores throughout the simulations compared to a random uniform distribution. (Bottom) Sample subset θ_{jB} tracks over time from run IR_by5_s2, where variations are due to the changing direction of the j vector, thereby also changing the magnitude of the specific angular momentum.

$d\theta_j/dt \sim 5-10^{\circ}/10^4$ yr. In the MHD runs, large directional changes ($d\theta_j/dt > 15^{\circ}/10^4$ yr) occur at a rate of 6%, compared to an occurrence rate of 9% for the hydrodynamic case.

In comparison, fluctuations in the total magnetic field direction averaged across the sink-patch system, B_{TOT}, are small, on the order of $d\theta_B/dt \sim 1-2^{\circ}/10^4$ yr, and rarely exceeding $15^{\circ}/10^4$yr. Changes in the magnitude of the total magnetic field occur over longer timescales, but rarely exceed variation by more than a factor of 2 over the lifetime of the sink-patch systems.

As such, the changes in the angle between the spin axis of the core and that of the magnetic field, θ_{jB} are due to the variations in the direction of the core angular momentum. Misalignment between the spin axes and magnetic field direction is a natural consequence of the rapidly varying direction of angular momentum flux, leading even originally aligned cores to become misaligned over time. In Figure 7.6, we show the distribution of θ_{jB} across all the MHD runs, the relative angle between the direction of the core magnetic field and angular momentum vectors, compared to a random uniform distribution of the same sample size. A K-S test comparison confirms that the null hypothesis can not be rejected for θ_{jB} being drawn from a random uniform distribution at 99.5% confidence.

7.4.2.2 Accretion onto Cores

Variability in the flux of material accreted onto the sink-patch system plays a large role in dictating the changes in the direction of j and increases the likelihood of misalignment between j and $\mathbf{B}$. Due to the heterogeneous nature of the sink-patch environment, accretion onto the core occurs episodically and non-isotropically, quite similarly to the behavior seen in the hydrodynamic case; see Figure 7 in Kuznetsova et al. (2019). Using the sample of core accretion histories and the information within the core's boundary cells we calculate the flux of quantities into the patch across the faces of patch walls. Analyzing the accretion over time, we statistically characterize patch accretion episodes by their length, peak flux, and effect on the specific angular momentum.

For each core in the sample of MHD runs, we identify accretion episodes first by finding the roots of a polynomial fit to the total net accretion onto the patch over time, $\dot{M}_p$; the start and end times for each episode are then given by the location of the polynomial's zeroes. For each episode we calculate a peak flux amount, an episode length, and a variation in the specific angular momentum, σ_j. The peak flux amount $\dot{M}_{p,peak}$ is the maximum of the total net flux into the patch over the duration of the episode Δt_{ep}. The standard deviation of the angular momentum on the boundary during the episode is then σ_j, compared to the mean episode angular momentum $\overline{j}_{ep}$.

In Figure 7.7, we show the accretion properties across episodes for every core that had more than one accretion episode, as identified by the behavior of the total flux into the patch. The total net flux into the patch leads to a fairly conservative classification scheme that excludes the cores that appear to experience continuous accretion. However, even when the total net flux appears continuous, decomposing the total flux into orthogonal components yields many smaller overlapping sub-episodes as the cores switch between spatially distinct accretion reservoirs (see Appendix B.2 for details). The overlap between directional components in time makes it difficult to accurately assign properties to individual sub-episodes, thus we only consider the total net flux when discussing properties of the episodes. This means that the episode lengths in Figure 7.7c are upper limits; component sub-episodes tend to be a factor of 2-3 shorter in duration.

Normalized by the patch flux, and centered on when the patch flux is at a maximum, the

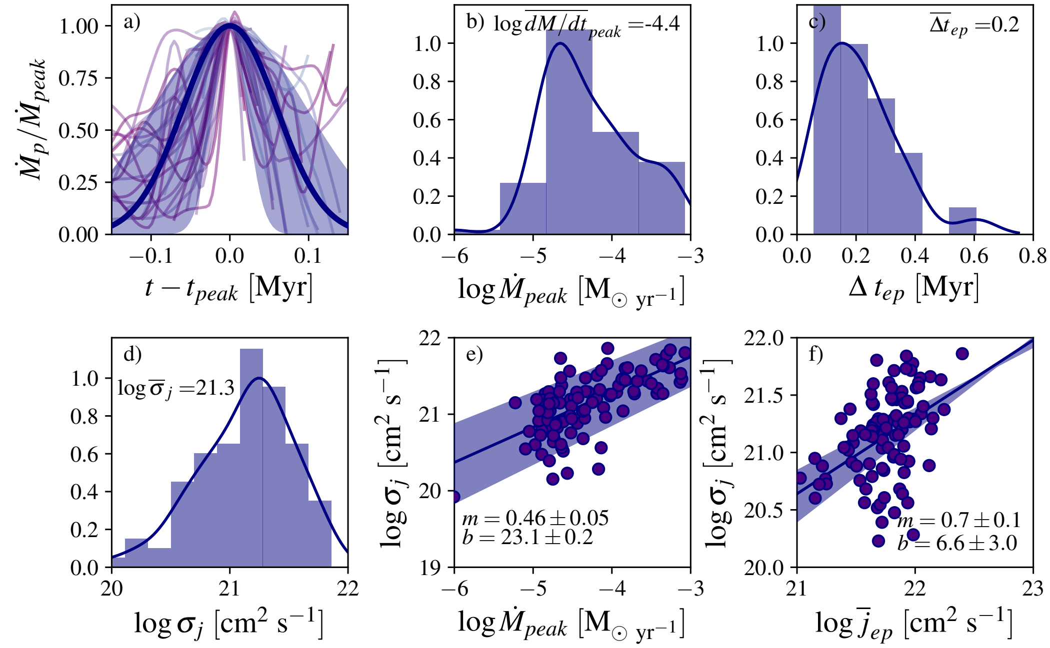

Figure 7.7: Episode properties for cores that had more than one episode as classified by their total net patch flux into the patch. a) Episode shapes overplotted with a Gaussian with a FWHM of 0.14 Myr. Shaded regions reflect the standard deviation in the FWHM (0.09 Myr) for all episodes b) Distribution of peak fluxes $\dot{M}_{peak}$. c) Distribution of upper limits on the total length of the episode Δt_{ep} d) Distribution of variation of the episode angular momentum σ_j e) Direct correlation between the variation in the angular momentum over the course of the episode and the net peak flux, with fits to $\log \sigma_j = m(\log \dot{M}_{peak}) + b$ shown f) Correlation between the variation in the angular momentum and the mean angular momentum for the episode with fits to $\log \sigma_j = m(\log \overline{j}_{ep}) + b$.

average episode shape can be modeled by a Gaussian centered on the time of the episode's peak accretion with $\sigma = 0.06$, for a FWHM of 0.14Myr. A typical peak mass flux into the patch is 3.6×10^{-5} $\mathrm{M_\odot yr^{-1}}$ at 0.1 pc. As shown in Figure 7.7e-f, the peak mass flux into the patch and the mean specific angular momentum for an episode are correlated with the magnitude of the variation in the angular momentum during the episode. For a typical core accretion episode, the expected variation in the specific angular momentum is on the order of $\log \sigma_j = 0.2 \log \bar{j}_{ep}$.

Integrating the mass accreted in an episode, and comparing contributions from each orthogonal direction, we can place a lower limit on the frequency of anisotropic accretion. We find that at least $\sim 60\%$ of episodes as we've characterized them above have accreted primarily along only one or two directions. This means that for the majority of episodes, accretion occurs in a filament or sheet-like flow.

7.5 Discussion

7.5.1 Global Magnetic Field Behavior

It is important to test whether our simulations are in reasonable agreement with observations of magnetic field strengths and structures on scales larger than cores. As discussed in §7.4.1, the variation of magnetic field strength with density is consistent with the observational results of Crutcher et al. (2010) (Figure 7.2). As discussed in Crutcher et al. (2010); Crutcher (2012), this behavior is consistent with flow along field lines at low densities, and the scaling law predicted from spherical gravitational contraction during flux freezing, $B \propto \rho^{2/3}$, at high densities. Based on Figure 7.2, flux-freezing is maintained up to the highest densities in the simulation, constituting an important check of our simulations with observational results. The orientations of the plane of sky magnetic fields relative to filamentary structure are also consistent with observational results from (Planck Collaboration et al., 2016) (Figure 7.3). In the Appendix, we show maps of the angle ϕ between the magnetic field $\mathbf{B}$ and the iso-column density contours, which at least qualitatively show the same jumbled structure seen in Figure 9 of Planck Collaboration et al. (2016).

7.5.2 Magnetic Flux, Misalignment, and the Magnetic Braking Catastrophe

Investigations of the effects of misalignment between the magnetic field and spin axis on disk formation, found that both misalignment on the order of 20° and magnetic supercriticality of at least $\mu \geq 4$ are required to bypass or reduce the effects of the magnetic braking catastrophe without invoking non-ideal MHD effects (Mellon & Li, 2008). In this study we find initial mass to flux ratios with a mean around $\mu = 3.6$, in a distribution with fairly long tail that extends out to values of $\mu \sim 10$ (Figure 7.5b). In this context it is important that our volumetrically-derived magnetizations μ_{3D} are systematically larger than the μ_{2D} calculated using the Crutcher (2004) relation (Figure 7.4a).

We note also that the value of μ increases over time as cores accrete mass more readily than their magnetic field values increase - a result which follows from accretion along field lines. Misalignment between the magnetic field and the spin axis of the core is common; at the core scale ($r \sim 0.1$ pc), we find a random uniform distribution of angles between the magnetic field vector and the spin axis of the core (Figure 7.6)a.Krumholz et al. (2013) concluded that the observed protostellar disk fraction can not be reproduced with a random uniform distribution of θ_{jB} and a median mass to flux ratio of 2, based on the observed mass to flux from the surveys of molecular cloud cores by Crutcher (2012). This problem could be at least partially addressed with the larger mass to flux ratios we've calculated for the cores in this study. However, even if we were to discount the difference between μ_{2D} and μ_{3D}, their analysis does not account for a time variable θ_{jB} in which any core's spin axis has a chance of becoming misaligned relative to the magnetic field at some point in its evolution, a process we show to be quite common in our simulations in Figure 7.6b.

Due to the time variability in the direction of the angular momentum, alignment at any one time does not guarantee alignment at later times, such that any core can become misaligned from the magnetic field after an accretion episode. Whereas, Joos et al. (2013) produces misalignments by imposing a turbulent velocity within the core, we find that misalignment can be externally imposed by episodic highly directional accretion flows from a local heterogeneous environment.

Recent simulations from (Wurster et al., 2019) of star formation in turbulent magnetized clumps find that protostellar disk formation occurs independent of the presence of non-ideal MHD effects and conclude that turbulent gas motions of the protostellar core environment play a larger role than magnetic effects in the formation of disks.

As a caveat, due to the resolution of the sink-patch, θ_{jB} is effectively a measurement on the 0.1 pc scale, while disk formation simulations induce misalignment extending down to the protostar. It is possible that significant angular momentum transport on sub-core scales could dampen the effects seen at our resolution limit.

7.5.3 Hallmarks of a Heterogeneous Star Forming Environment

On large scales, filaments in the simulation are in good agreement with observed star forming regions when smoothed to similar resolutions, but it is clear that the inter-filament medium is highly substructured. The episodic nature of accretion captured at the core scale implies a heterogeneous star-forming environment, a fact also noted in other numerical studies of cluster formation (Kuffmeier et al., 2017, 2018). The time dependent directionality of accretion onto cores creates the variation in the direction of the angular momentum vector and suggests the existence of spatially distinct accretion reservoirs. That is, there must be a finite number of overdensities in the form of directional accretion flows or streams in order to explain the amount of variation in the direction of the angular momentum vector.

Filament 'fibers' have been identified by the presence of velocity coherent substructures within observations of star-forming regions (e.g. Hacar et al., 2013; Hacar et al., 2018). While there are many proposed explanations for this sub-structuring, including fragmentation, it is possible that these sub-filamentary structures are observational signatures of the type of dense structures that fall in to produce episodic core accretion and changes in the direction of the angular momentum vector. To support this conjecture, a fiber of length ~ 0.1 pc, characteristic of structures seen in our simulations and onsistent with the peak of the ISF fiber lengths in Hacar et al. (2018), next to a core of mass $10-15$ $\mathrm{M}_{\odot}$ would exhibit an infall velocity of $0.7-0.8$ km s^{-1}, resulting in an accretion episode lasting ~ 0.14 Myr, consistent with the simulations (upper right panel of Figure 7.7). Note that for typical magnetic field values of 60 μG at densities of at least $n_H \sim 10^5 \mathrm{cm}^{-3}$, the Alfven velocity is at most 0.3 km s^{-1}, and so the inflow is at least marginally super-Alfvenic.

7.5.4 Considerations for Modeling Realistic Disk Formation

We find that the ideal MHD model used here decreases the efficiency of star formation compared to our hydrodynamic runs, while the cores that do form are supercritical such that their formation and evolution is dominated by gravitational infall. The statistical relationship between the patch masses and sink accretion rates such that $\dot{M}_s = (M_s + M_p)^2$ investigated in (Kuznetsova et al., 2018) remains true for the cores in this sample. The presence of magnetic fields does not impact the growth of the upper-mass power law by accretion; gravitational infall drives accretion onto the sink-patch system.

The dynamics of the cores are primarily dominated by the influx of multidirectional flows, as in (Kuznetsova et al., 2019). The shapes of the distributions and behavior of the specific angular momenta between the HD and MHD runs are also consistent. We do find that the MHD runs exhibit lower amplitude variability in the magnitude of the specific angular momentum and experience fewer intense directional flips than the HD case. This suggests that the magnetic field may have some influence on the direction of the angular momentum vector, but not enough to enforce alignment, at least on the core scale.

The specific angular momentum remains nearly constant over time for all cases, showing essentially the same behavior as in the hydrodynamic case (see Figure 3 in Kuznetsova et al. (2019)). This behavior suggests that growing the core through accretion from a realistic heterogeneous environment has marked departures from the disks predicted by the smooth isotropic disk formation models which predict growth of specific angular momentum with time as angular momentum is inherited from a uniformly rotating cloud (Terebey et al., 1984).

Protostellar collapse models have become increasingly more sophisticated as they include additional physics such as non-ideal MHD or radiation effects (e.g. Wurster et al., 2018; Bhandare et al., 2018), but the initial conditions adopted in these studies are commonly smooth and spherically symmetric. Other top-down numerical studies which simulate the dynamics of the molecular cloud as well as zoom in to the formation of individual protostars and disks also find that accretion is very much non-isotropic, commonly occurring in filaments or sheets and time variable in nature (Kuffmeier et al., 2017). While additional transport processes occur on scales that are non-resolvable in our simulations, the statistical assemblages presented here offer a range and distribution of initial and boundary conditions for future work with more detailed disk simulations.

We provide the probability density functions and of both core and infall properties and requisite code tools as a supplementary archive [1].

7.6 Summary

We modeled the formation of star clusters with the grid code *Athena* including ideal MHD effects in order to understand how magnetic fields affect star formation on both the cloud and core scales. Our main findings were:

1. Globally, simulations were in agreement with observed magnetic field structures measured on the same scales.

2. A comparison of 'observed' and actual core magnetizations yields that is possible to underpredict μ from projected data, with a factor of ~ 2 difference in the median μ, compared to reported values from Zeeman measurements of molecular clouds.

3. The mass inflows into protostellar cores have specific angular momenta j that are randomly oriented with respect to the overall magnetic field direction. The inflows often occur in distinct episodes lasting $\gtrsim 0.1$ Myr, with each individual episode exhibiting very different orientations of j. There is little time evolution of the magnitude of j.

Our findings indicate that protostellar accretion is likely not characterized by slowly varying, isotropic infall often assumed. The distributions of core properties, as well as characterisation of

---

[1] https://github.com/akuznetsova/proto-props

discrete episodes of accretion onto the cores presented in this chapter, can provide more realistic initial and boundary conditions for studies of protostar and disk formation in higher resolution simulations.

7.7 Acknowledgements

This work was supported by NASA grant NNX16AB46G and by the University of Michigan, and used computational resources and services provided by Advanced Research Computing at the University of Michigan, Ann Arbor and the University of North Carolina at Chapel Hill Research Computing group.

CHAPTER 8

Conclusion

Since James Jeans original 1902 work, the physics of star formation has been well studied on the individual protostellar core scale. However, the impact of the star forming environment has long been an open question, where the relative roles of turbulence, magnetic fields, feedback, and gravity in the interstellar medium have been the subject of debate. As most stars form in cluster environments, this thesis work has focused on disentangling the relative contributions of physical effects on the cluster scale in order to understand how they affect properties on the core scale. The eventual aim of this set of projects has been to extract core statistics from large scale cluster formation simulations for use as initial and boundary conditions in disk formation models. Self-consistent modeling from the top-down, cluster to core scales, provides physically motivated initial conditions such that disk formation can be simulated as close to *ab initio* as possible.

8.1 Summary of Findings

This research has used a variety of code types selected based on their applicability to a specific problem or scale, including smoothed-particle hydrodynamics (SPH), N-body, and MHD grid models. The design of the approach depends on a series of numerical experiments in order to answer specific questions rather than computationally extensive 'kitchen-sink' style simulations that include all the possible physics.

8.1.1 Investigating Gravitational Focusing During Assembly of Star Forming Materials

A consequence of gravitational focusing (where $dM/dt \propto M^2$) is that the asymptotic limit of a distribution of accreting masses is a power law slope, $d\log N/d\log M \propto M^{-1}$ (Zinnecker, 1982). In Chapter 2, we applied this concept at GMC scales to investigate the assembly of star forming material and its role in building the star cluster initial mass function (scIMF). Using a cluster finding algorithm on N-body simulations, thus bypassing explicitly prescribed accretion schemes, gravitational focusing readily produces the observed empirical power law scIMF relation, assembling self-gravitating material hierarchically, suggesting that star formation could occur rapidly once material is assembled.

In Chapter 5, with a new sink-patch implementation that was designed to track accretion within the star's immediate environment for the *Athena* code, we demonstrated that gravitational infall dominated the growth of the core initial mass function. This was made possible by tracking the entire self-gravitating mass of the protostellar core through the sink-patch construction, bolstering the arguments from Ballesteros-Paredes et al. (2015), and emphasized the importance of analyzing the statistical behavior of protostellar cores.

8.1.2 Motivating the Cold Collapse Paradigm for Star Cluster Formation

Much of the past work on star cluster formation operates with the starting assumptions that turbulent motions support the molecular cloud against collapse and, thus, regulate the rate of star formation. The alternative scenario in which star cluster formation occurs by global gravitational collapse of the progenitor molecular cloud has been relatively unexplored. In Chapter 3, I investigated the viability of this mode of cluster formation by comparing the morphological and kinematic properties of the resulting simulated cluster to a nearby test case - the Orion Nebula Cluster (ONC). We found that gravitational collapse of an ellipsoidal cloud can readily produce the canonical hub-spoke morphology of embedded clusters (Myers, 2009) and, in some cases, the large scale velocity gradients seen across the filament of the ONC (Fűrész et al., 2008; Tobin et al., 2009).

When radial velocity surveys of the ONC identified kinematic and spatial substructure within the Orion filament filament (Da Rio et al., 2017; Hacar et al., 2017), we conducted a complementary analysis (Chapter 4) and found that velocity coherent kinematic substructure of stellar groups is a hallmark of the hierarchical assembly of sub-clusters within the gravitational potential of the gaseous filament.

8.1.3 Determining the Conditions for Disk Formation

With the goal of constraining the initial conditions for disk formation, I leveraged the functionality of the sink-patch implementation for *Athena* to track the accretion of both mass and angular momentum in the sink's environment. At the scales of the cluster simulations, the sink and the patch represent the protostellar core and the envelope - the outer boundary of patch corresponding to a core of $\sim 0.05 - 0.1$ pc in size.

In Chapter 6, I present the results of a numerical experiment in which we varied the initial angular momentum content of the global cloud and measured specific angular momenta on core scales over time. We found that the distribution of core specific angular momentum does not change over time and has no dependence on global angular momentum, thus angular momentum is imparted early on in a local process, possibly through gravitational torques between gaseous pre-stellar clumps. Later accretion of material is anisotropic and episodic as cores accrete material through short-lived filamentary and sheet-like streams. The direction of specific angular momentum for the core varies which does not allow for the monotonic growth of specific angular momentum over time that is predicted by simple models of uniformly rotating collapse (Terebey et al., 1984; Cassen & Moosman, 1981).

In Chapter 7, I tested the effects of magnetic fields on this model by adding in an initially uniform global magnetic field and determined that gravitational accretion still dominates the dynamics of the cores which form magnetically supercritical. We found good agreement between the large scale magnetic field behavior in the simulations with observational diagnostics of magnetic fields. On the core scale, I determined that the anisotropy of accretion leads to a uniform distribution of angles between the angular momentum vector and the magnetic field, with strong implications for disk formation that is uninhibited by the magnetic braking catastrophe.

Stacking the core populations across several simulations for statistical power, I was able to quantify the range and relative distribution of protostellar core properties. For each accretion episode, I measured the angular momentum and mass flux into the core, the duration of the episode, and isolated the direction of the flux. Combining accretion statistics for all the cores, I was able to characterize accretion behavior and generate probability distribution functions for episode parameters. These products will be released to the community for use in modeling disk formation.

8.2 Future Directions

The inherent heterogeneity in star-forming environments naturally produces the multi-directional episodic accretion seen in large scale simulations and hinted at in observations (Tobin et al., 2015). This suggests that modeling protostellar envelopes, simulating disk formation, and our picture of the physical processes involved in early phase embedded protostellar sources needs to move past the smooth symmetric analytic models that have been employed thus far (Figure 8.1).

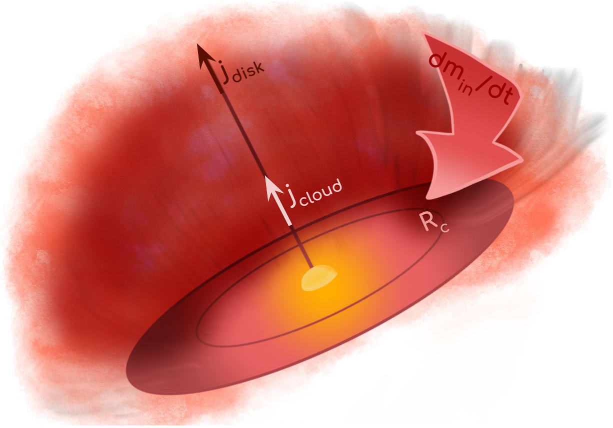

Figure 8.1: Classical picture of protostellar disk infall adapted from Cassen & Moosman (1981). Material from a rotating cloud enters on parabolic orbits, landing in a zone near the centrifugal radius, $R_c = j_{cloud}^2/GM_*$, dictated by its specific angular momentum, j_{cloud}. During collapse (Terebey et al., 1984), angular momentum is inherited from the uniformly rotating cloud material such that $j_{cloud} \propto t^2$ and $R_c \propto t^3$.

Protostellar infall represents a bridge between star formation and the evolution of the protoplanetary environment. The collapse of protostellar clouds with finite angular momenta naturally produces planet-forming disks, whose properties are thought to be inherited from their parent clouds. Investigating the role of infall onto the nascent disk during early phases is essential for understanding these objects. Subsequent planet formation is inextricably linked to and mediated by processes within the circumstellar disk.

This thesis work found accretion behavior onto protostellar objects that implies more radially concentrated episodic infall onto the disk, likely to result in larger density perturbations than in classical models of smoothly varying and isotropic infall (Figure 8.2).

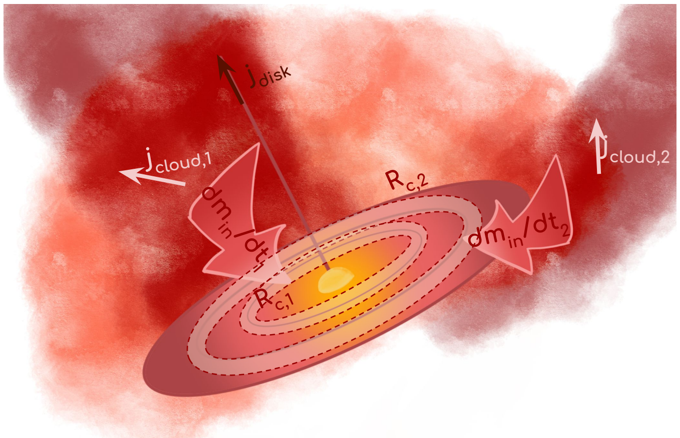

Figure 8.2: The directional nature of infall leads to a constant magnitude of specific angular momentum over time leading to a fundamentally different picture of disk formation and evolution. Concentrated episodic infall in discrete episodes can be modeled with annular deposition of material onto the disk, potentially leading to a build up of material in the outer disk and increased transport in others.

Such perturbations in the pressure profile of disks have been shown to facilitate the concentration of planet building materials needed for effective planet formation (Pinilla et al., 2012). In addition to pressure bumps, infalling material can induce velocity shear capable of opening gaps in the disk. Gap opening by planets has already has been proposed as a mechanism to filter and concentrate dust grains, creating zones of increased and decreased grain growth (Zhu et al., 2012). While planets have long been the primary suspects for opening gaps in disks (e.g. Alexander & Armitage, 2007; Zhu et al., 2011), infalling material also has the capacity to open large gaps early on in formation, without requiring the presence of one or multiple planets. Future investigation of how anisotropic infall forms and structures protoplanetary disks is necessary in order to develop this qualitatively new picture of the initial conditions of planet formation.

Numerical simulations (Lesur et al., 2015) have shown that smooth infall alone can produce an accretion shock and drives spiral density waves that transport mass and angular momentum. Using *FARGO* simulations, I show that radially concentrated infall can readily produce spirals, rings, and gaps (Figure 8.3), suggesting the existence of regimes where planet formation is efficient at early disk ages.

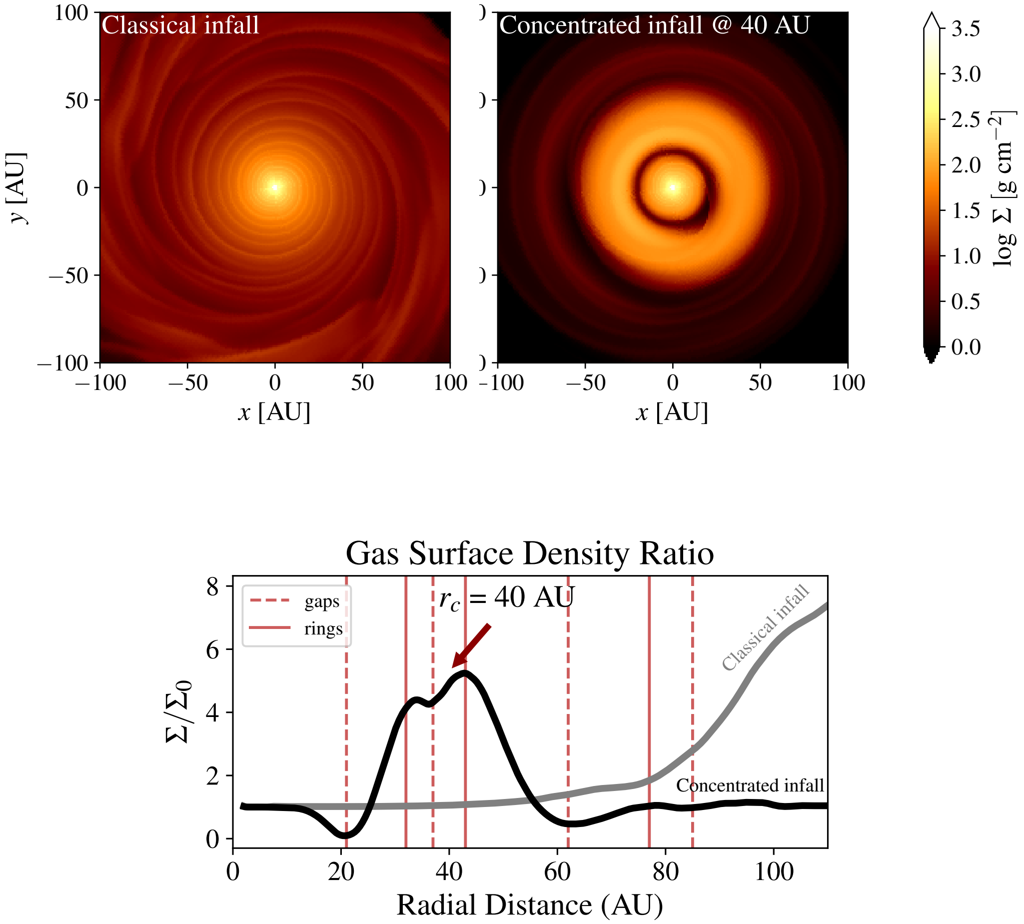

Figure 8.3: The inner 100 AU of preliminary *FARGO* simulations (at t = 30 kyr) comparing two infall models (left) smoothly varying accretion, material is injected into the disk at large radii, as in Lesur et al. (2015) and can produce spiral waves that propagate inward (center) an episode of concentrated annular infall around 40 AU drives spiral features and creates rings and gaps, best seen in (right) density ratios relative to the initial surface density profile; the concentrated model in black and the smooth injection model in gray, rings and gaps are solid and dashed vertical lines.

Recent observations have yielded that many protoplanetary disks are rife with substructure in the form of spirals, rings, and gaps (Andrews et al., 2018), many of which are likely due to the perturbations of forming planetary bodies, but have fairly low dust and gas masses for objects that are supposed to be reservoirs of planet forming materials (Ansdell et al., 2016). This further suggests that planet formation could be occurring at much earlier phases than previously thought.

Future work can use the results of my thesis to create an infall model designed to investigate the role of infall-mediated disk processes in the transport and concentration of planet building materials, understand the role of planets in the evolution of substructure, and thus aid in the interpretation of observations of rings and gaps in protoplanetary disks. Directly connected to the star formation process, future work will be able to examine the impact of star forming environments on disk conditions and planet formation, which ultimately leads us closer to understanding the probability of forming habitable systems in the Universe.

APPENDICES

APPENDIX A

Resolution Comparison

The following comparison refers to the results in Chapter 5 and discusses the differences in the mass accretion rate and initial mass function due to an increase in dynamic range.

The main results of are largely unchanged by a factor of 2 increase in resolution (dynamic range). Here we show figures corresponding to Figures 5.1 and 5.2 but at a resolution of 1024^3, such that the patch is now at a scale of 0.05 pc instead of 0.1 pc. The primary differences between the two runs is that at 1024^3 more sinks are created and the power law of the mass function tends to better developed within 2.2 Myr for the higher resolution runs.

There is less mass in the patch gas as the physical size of the patch is now reduced, however, as the scale of structures tends to decrease while the density increases in an isothermal simulation, this difference does not appear to be very large when comparing the last panels of Figure 5.2 and Figure A.2, both shown at t = 2.2 Myr ($\sim 1.3\ t_{\rm ff}$).

The reduction in physical accretion radius does not have an appreciable effect on the accretion rates and only a small effect on patch masses, still yielding the $dM/dt \propto M^2$ behavior seen in the fiducial run.

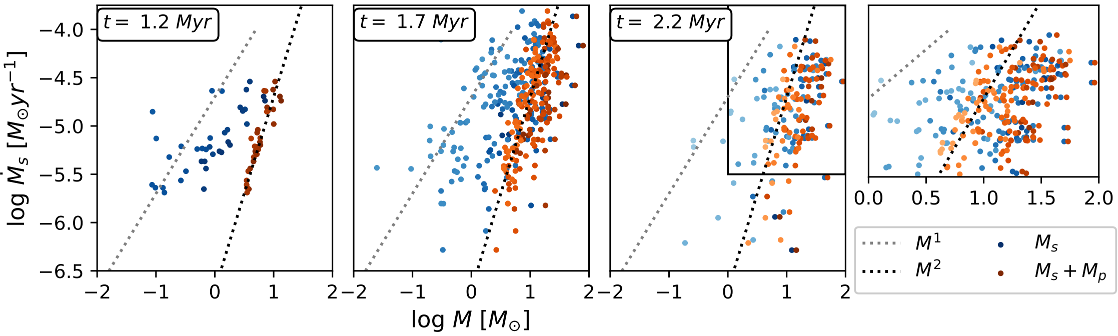

Figure A.1: Sink accretion rate vs sink mass, M_s, and total enclosed patch mass, $M_s + M_p$ shown for t = 1.2, 1.7, and 2.2 Myr for the high resolution run. The gray and black dotted lines have slopes of 1 and 2, respectively.The $\dot{M}_s^2 \propto (M_s + M_p)^2$ relationship still holds for $N_{cell} = 1024^3$, even when patch sizes are smaller.

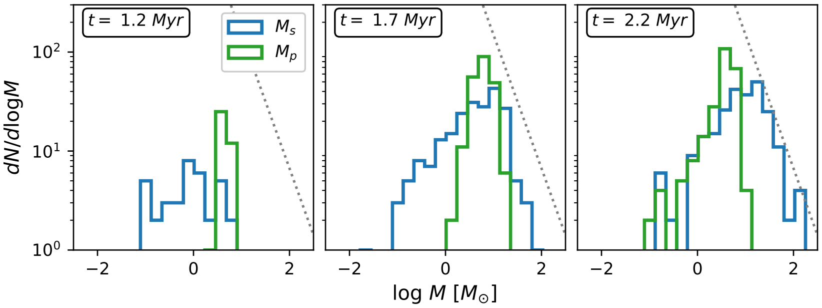

Figure A.2: Mass function for the sink mass M_s (blue) and the patch mass M_p (green) at 1.2, 1.7, and 2.2 Myr, for a resolution of 1024^3. The gray dotted line is the $\Gamma = 1.35$ Salpeter slope. The patch gas masses are somewhat smaller due to the decreased patch size.

APPENDIX B

Details of MHD Simulation Analysis

The following sections refer to details of the analysis of MHD runs in Chapter 7. In §B.1, we discuss the method of computation of the histograms of relative orientation (HRO) from the simulation data. In §B.2, we discuss the caveats of how accretion episodes of sink-patches were calculated and the resulting limitations of the analysis.

B.1 Calculating relative orientations

The relative orientation is computed as the angle ϕ, the angle between the magnetic field **B** and the iso-column contours, is represented by the direction of the gradient in column density N_H. The gradient is calculated by convolving the column density map with a symmetric two-dimensional Gaussian derivative kernel, G_x and G_y are calculated using the x- and y- derivatives, respectively:

$$\nabla N_H = (G_x \otimes N_H)\hat{\mathbf{i}} + (G_y \otimes N_H)\hat{\mathbf{j}} = g_x\hat{\mathbf{i}} + g_y\hat{\mathbf{j}} \tag{B.1}$$

The orientation of the gradient is then $\theta_{N_H} = \arctan(-g_x, g_y)$. We show the maps of ϕ for all three projections in Figure B.1. The results show reasonable agreement with observations (see Figure 9 in Planck Collaboration et al., 2016).

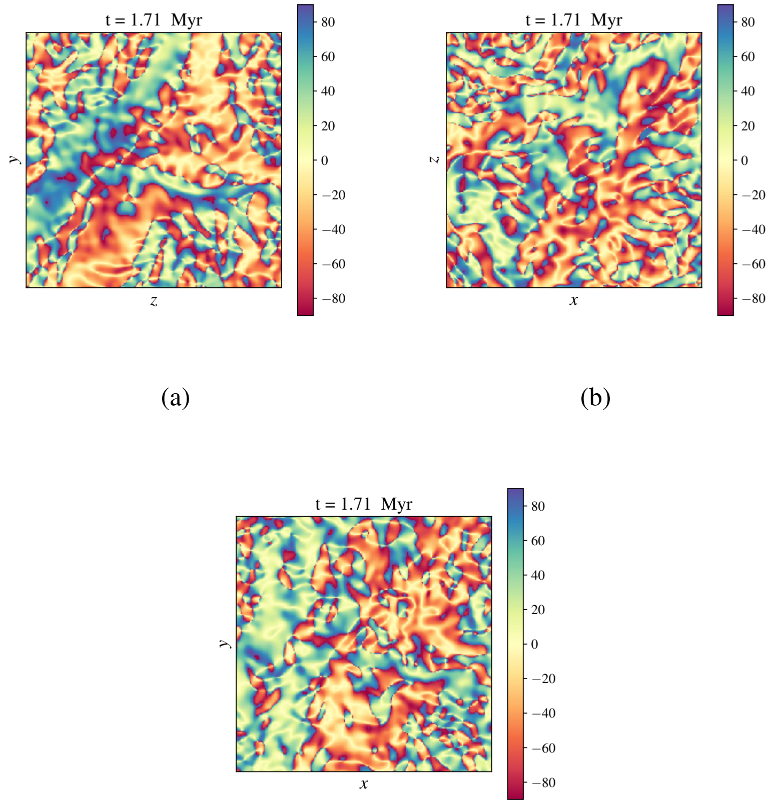

(a) (b)

(c)

Figure B.1: Maps of the angle between the the magnetic field direction and the iso-density contour, ϕ, for column density projections of run IR_by5_s2 across the inner 12 pc of the simulation domain, centered on the cloud.

Based on the methods outlined in Planck Collaboration et al. (2016), we construct a histogram of relative orientation (HRO) between the derived filament and the magnetic field directions. Relative orientations are measured as the angle between the magnetic field in each cell and the gradient across the column density for each projection of run IR_by5_s2. Both the magnetic field and column densities are smoothed with a Gaussian kernel of $\sigma = 4$ cells, to limit to resolved structures on the 0.4pc scale. This chosen smoothing corresponds to the smoothed Planck map resolution of 10' at a distance of 140pc, similar to the Taurus region.

Results are evenly sampled from column density ranges at the 68th, 90th, and 98th percentile level, each corresponding to a line in Figure 7.3. At the chosen 90th percentile level, $\log N_H/cm^{-2} =$

21.7, the HRO becomes very clearly in favor of a perpendicular orientation between the magnetic field and the iso-density contour; this value is consistent with the turnover density determined from the Planck polarisation measurements. The errors due to binning shown as a shaded region and calculated from $\sigma_h^2 = N_i(1 - N_i/N_{tot})$, where N_i and N_{tot} are the number of samples in the bin and the the number of total samples, respectively.

In Figure 7.3a-b, the magnetic fields are preferentially oriented perpendicularly to the highest density filaments, with some parallel alignment in the lower density regime. The parallel alignment of the lowest density contours is difficult to discern by eye in the HRO, but the relative integrated contributions from the center of the HRO are greater compared to those from the outer edges. In the case of the projection in the $x-y$ plane, where the line of sight is preferentially along the filament axis, the orientation is marginally in favor of parallel orientations, rather than perpendicular ones.

B.2 Episodes and Sub-episodes

The sample of core episodes only includes cores that have more than one episode as classified by the total net flux into the patch. This classification removes cores that appear to be accreting continuously. However, cores with continuous total patch accretion over time are not necessarily isotropically and smoothly accreting from their surrounding medium (see core 4 in Figure B.2). When the total net flux is decomposed into its orthogonal components, it is evident that the larger continuous episode is comprised of multiple periods of time when different flows dominate, suggesting accretion from discrete spatial sources.

The fact that episodes in total patch flux are actually comprised of many sub-episodes also applies to the sample of cores used in the study, those with $N_{episode} > 1$, such as core 8's last episode seen in Figure B.2 in which a transition from one direction to another happens halfway through. This overlap makes it difficult to constrain a sub-episode's contribution to the mass accreted, for example, as some directions are also flows out of the patch, which is why we have opted to use the total net flux in our analysis. However, we note that this means that the distributions of episode lengths are then upper limits.

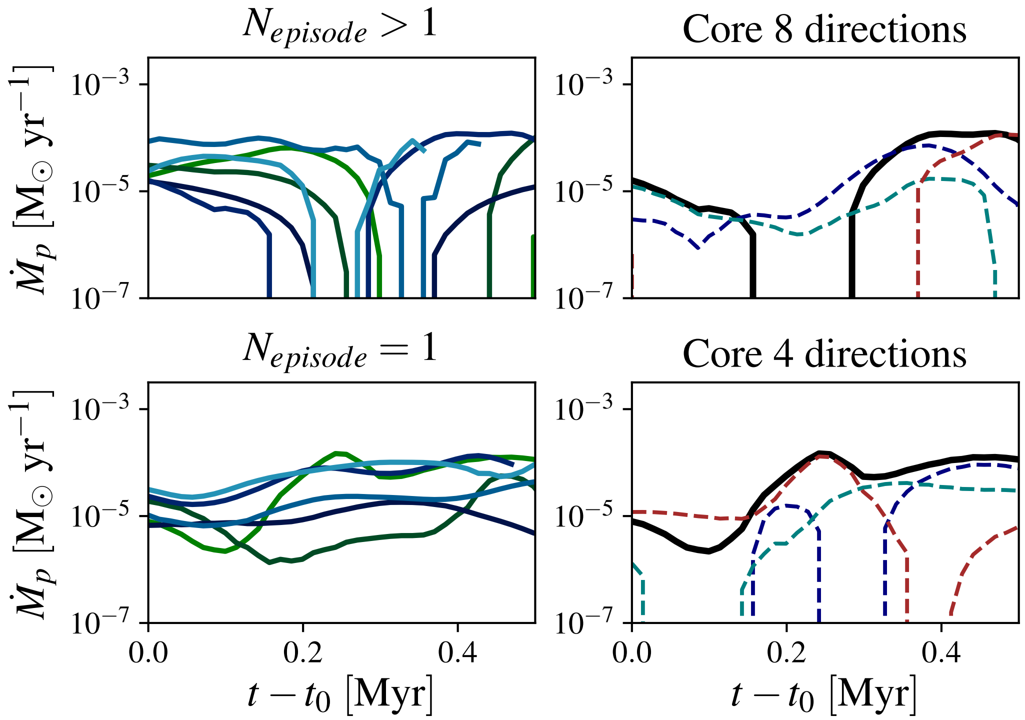

Figure B.2: Top row: Patch fluxes for cores with more than one episode (left) sample of cores with more than one episode (right) core 8's patch flux (solid black line) decomposed into its orthogonal components (dashed lines). Bottom row: Patch fluxes whose total flux is continuous (left) sample of cores with continuous total patch flux (right) continuous patch flux for core 4 (solid black line) with its component parts, decomposed into orthogonal directions (dashed lines).

BIBLIOGRAPHY

BIBLIOGRAPHY

Adams, F. C. 2010, *ARA&A*, 48, 47

Adams, F. C., Lada, C. J., & Shu, F. H. 1987, *ApJ*, 312, 788

Alexander, R. D., & Armitage, P. 2007, *MNRAS*, 375, 500

Allison, R. J., & Goodwin, S. P. 2011, *MNRAS*, 415, 1967

Allison, R. J., Goodwin, S. P., Parker, R. J., et al. 2009, *ApJ*, 700, L99

Allison, R. J., Goodwin, S. P., Parker, R. J., Portegies Zwart, S. F., & de Grijs, R. 2010, *MNRAS*, 407, 1098

ALMA Partnership et al.,. 2015, *ApJ*, 808, L3

André, P., Men'shchikov, A., Bontemps, S., et al. 2010, *A&A*, 518, L102

Andrews, S. M., Huang, J., Pérez, L. M., et al. 2018, *ApJ*, 869, L41

Ansdell, M., Williams, J. P., van der Marel, N., et al. 2016, *ApJ*, 828, 46

Bae, J., Hartmann, L., & Zhu, Z. 2015, *ApJ*, 805, 15

Bae, J., Hartmann, L., Zhu, Z., & Nelson, R. P. 2014, *ApJ*, 795, 61

Bai, X.-N. 2016, *ApJ*, 821, 80

Balfour, S. K., Whitworth, A. P., Hubber, D. A., & Jaffa, S. E. 2015, *MNRAS*, 453, 2471

Ballesteros-Paredes, J., Hartmann, L. W., Pérez-Goytia, N., & Kuznetsova, A. 2015, *MNRAS*, 452, 566

Ballesteros-Paredes, J., Hartmann, L. W., Vázquez-Semadeni, E., Heitsch, F., & Zamora-Avilés, M. A. 2011, *MNRAS*, 411, 65

Ballesteros-Paredes, J., Vázquez-Semadeni, E., Palau, A., & Klessen, R. S. 2018, *MNRAS*

Bally, J. 2008, Overview of the Orion Complex, ed. B. Reipurth, 459

Bally, J., Langer, W. D., Stark, A. A., & Wilson, R. W. 1987, *ApJ*, 312, L45

Banerjee, R., Klessen, R. S., & Fendt, C. 2007, *ApJ*, 668, 1028

Bastian, N. 2008, *MNRAS*, 390, 759

Bastian, N., Gieles, M., Ercolano, B., & Gutermuth, R. 2009, in IAU Symposium, Vol. 256, The Magellanic System: Stars, Gas, and Galaxies, ed. J. T. Van Loon & J. M. Oliveira, 45–50

Bate, M. R. 1998, *ApJ*, 508, L95

Bate, M. R. 2012, *MNRAS*, 419, 3115

—. 2018, *MNRAS*, 475, 5618

Bate, M. R., Bonnell, I. A., & Bromm, V. 2003, *MNRAS*, 339, 577

Bate, M. R., & Burkert, A. 1997, *MNRAS*, 288, 1060

Battisti, A. J., & Heyer, M. H. 2014, *ApJ*, 780, 173

Beichman, C., Myers, P., Emerson, J., et al. 1986, *ApJ*, 307, 337

Bhandare, A., Kuiper, R., Henning, T., et al. 2018, *A&A*, 618, A95

Bleuler, A., & Teyssier, R. 2014, *MNRAS*, 445, 4015

Blitz, L. 1993, in Protostars and Planets III, 125–161

Bonnell, I. A., & Bate, M. R. 2006, *MNRAS*, 370, 488

Bonnell, I. A., Bate, M. R., Clarke, C. J., & Pringle, J. E. 2001a, *MNRAS*, 323, 785

Bonnell, I. A., Clark, P., & Bate, M. R. 2008, *MNRAS*, 389, 1556

Bonnell, I. A., Clarke, C. J., Bate, M. R., & Pringle, J. E. 2001b, *MNRAS*, 324, 573

Borges, J. L. 1998, Collected fictions

Boss, A. P., & Bodenheimer, P. 1979, *ApJ*, 234, 289

Bullock, J. S., Dekel, A., Kolatt, T. S., et al. 2001, *ApJ*, 555, 240

Burkert, A., & Bodenheimer, P. 2000, *ApJ*, 543, 822

Burkert, A., & Hartmann, L. 2004, *ApJ*, 616, 288

—. 2013, *ApJ*, 773, 48

Cartwright, A., & Whitworth, A. P. 2004, *MNRAS*, 348, 589

Cassen, P., & Moosman, A. 1981, *Icarus*, 48, 353

Chabrier, G. 2003, *PASP*, 115, 763

Chabrier, G. 2005, in Astrophysics and Space Science Library, Vol. 327, The Initial Mass Function 50 Years Later, ed. E. Corbelli, F. Palla, & H. Zinnecker, 41

Chen, C.-Y., & Ostriker, E. C. 2015, *ApJ*, 810, 126

Chen, C.-Y., & Ostriker, E. C. 2018, *ApJ*, 865, 34

Churchwell, E., Babler, B. L., Meade, M. R., et al. 2009, *PASP*, 121, 213

Corsaro, E., Lee, Y.-N., García, R. A., et al. 2017, *Nature Astronomy*, 1, 0064

Cottaar, M., Covey, K. R., Foster, J. B., et al. 2015, *ApJ*, 807, 27

Crutcher, R. M. 2004, *Ap&SS*, 292, 225

Crutcher, R. M. 2012, *ARA&A*, 50, 29

Crutcher, R. M., Wandelt, B., Heiles, C., Falgarone, E., & Troland, T. H. 2010, *ApJ*, 725, 466

Da Rio, N., Robberto, M., Soderblom, D. R., et al. 2010, *ApJ*, 722, 1092

Da Rio, N., Tan, J. C., & Jaehnig, K. 2014, *ApJ*, 795, 55

Da Rio, N., Tan, J. C., Covey, K. R., et al. 2016, *ApJ*, 818, 59

Da Rio, N., Tan, J. C., Covey, K. R., et al. 2017, *ApJ*, 845, 105

Dale, J., Ercolano, B., & Bonnell, I. 2012, *MNRAS*, 424, 377

de Grijs, R., Anders, P., Bastian, N., et al. 2003, *MNRAS*, 343, 1285

Dehnen, W. 2001, *MNRAS*, 324, 273

Edgar, R. 2004, *NewAR*, 48, 843

Elmegreen, B. G. 2007, *ApJ*, 668, 1064

Elmegreen, B. G., & Efremov, Y. N. 1997, *ApJ*, 480, 235

Elmegreen, B. G., & Elmegreen, D. 1978, *ApJ*, 220, 1051

Elmegreen, B. G., & Scalo, J. 2004, *ARA&A*, 42, 211

Evans, C. R., & Hawley, J. F. 1988, *ApJ*, 332, 659

Fall, S. M., & Chandar, R. 2012, *ApJ*, 752, 96

Fall, S. M., Krumholz, M. R., & Matzner, C. D. 2010, *ApJ*, 710, L142

Federrath, C. 2016, *MNRAS*, 457, 375

Federrath, C., Banerjee, R., Clark, P. C., & Klessen, R. S. 2010, *ApJ*, 713, 269

Flaherty, K. M., Hughes, A. M., Teague, R., et al. 2018, *ApJ*, 856, 117

Flaherty, K. M., Hughes, A. M., Rose, S. C., et al. 2017, *ApJ*, 843, 150

Foreman-Mackey, D., Hogg, D. W., Lang, D., & Goodman, J. 2013, *PASP*, 125, 306

Foster, J. B., Cottaar, M., Covey, K. R., et al. 2015, *ApJ*, 799, 136

Foster, P. N., & Chevalier, R. A. 1993, *ApJ*, 416, 303

Fűrész, G., Hartmann, L. W., Megeath, S. T., Szentgyorgyi, A. H., & Hamden, E. T. 2008, *ApJ*, 676, 1109

Gardiner, T. A., & Stone, J. M. 2008, *Journal of Computational Physics*, 227, 4123

Geyer, M. P., & Burkert, A. 2001, *MNRAS*, 323, 988

Gieles, M., Larsen, S. S., Bastian, N., & Stein, I. T. 2006, *A&A*, 450, 129

Goldreich, P., & Kwan, J. 1974, *ApJ*, 189, 441

Gong, H., & Ostriker, E. C. 2013, *ApJS*, 204, 8

Goodman, A., Benson, P., Fuller, G., & Myers, P. 1993, *ApJ*, 406, 528

Gottlieb, S., & Shu, C. W. 1998, *Mathematics of Computation*, 67, 73

Gray, W. J., McKee, C. F., & Klein, R. I. 2017, *MNRAS*, 473, 2124

Grenier, I. A., Black, J. H., & Strong, A. W. 2015, *ARA&A*, 53

Hacar, A., Alves, J., Forbrich, J., et al. 2016, *A&A*, 589, A80

Hacar, A., Alves, J., Tafalla, M., & Goicoechea, J. R. 2017, *A&A*, 602, L2

Hacar, A., Tafalla, M., Forbrich, J., et al. 2018, *A&A*, 610, A77

Hacar, A., Tafalla, M., Kauffmann, J., & Kovács, A. 2013, *A&A*, 554, A55

Hartmann, L. 2002, *ApJ*, 578, 914

Hartmann, L., & Bae, J. 2018, *MNRAS*, 474, 88

Hartmann, L., Ballesteros-Paredes, J., & Bergin, E. A. 2001, *ApJ*, 562, 852

Hartmann, L., & Burkert, A. 2007, *ApJ*, 654, 988

Haugbølle, T., Padoan, P., & Nordlund, Å. 2018, *ApJ*, 854, 35

Heitsch, F., & Hartmann, L. 2008, *ApJ*, 689, 290

Heitsch, F., Slyz, A. D., Devriendt, J. E., Hartmann, L. W., & Burkert, A. 2006, *ApJ*, 648, 1052

Hennebelle, P. 2012, *A&A*, 545, A147

Henriksen, R., Andre, P., & Bontemps, S. 1997, *A&A*, 323, 549

Heyer, M., Krawczyk, C., Duval, J., & Jackson, J. M. 2009, *ApJ*, 699, 1092

Hillenbrand, L. A., & Hartmann, L. W. 1998, *ApJ*, 492, 540

Hills, J. G. 1980, *ApJ*, 235, 986

Hockney, R. W., & Eastwood, J. W. 1981, Computer Simulation Using Particles (McGraw-Hill)

Hsu, W.-H., Hartmann, L., Heitsch, F., & Gómez, G. C. 2010, *ApJ*, 721, 1531

Huchra, J. P., & Geller, M. J. 1982, *ApJ*, 257, 423

Hull, C. L. H., & Zhang, Q. 2019, *Frontiers in Astronomy and Space Sciences*, 6, 3

Imara, N., & Blitz, L. 2011, *ApJ*, 732, 78

Jackson, R. J., & Jeffries, R. D. 2010, *MNRAS*, 402, 1380

Jappsen, A.-K., Klessen, R. S., Larson, R. B., Li, Y., & Low, M.-M. M. 2005, *A&A*, 435, 611

Jeans, J. H. 1902, *Philosophical Transactions of the Royal Society of London. Series A, Containing Papers of a Mathematical or Physical Character*, 199, 1

Jessop, N., & Ward-Thompson, D. 2000, *MNRAS*, 311, 63

Jetley, P., Gioachin, F., Mendes, C., Kale, L. V., & Quinn, T. 2008, in 2008 IEEE International Symposium on Parallel and Distributed Processing, IEEE, 1–12

Jones, B. F., & Walker, M. F. 1988, *AJ*, 95, 1755

Joos, M., Hennebelle, P., & Ciardi, A. 2012, *A&A*, 543, A128

Joos, M., Hennebelle, P., Ciardi, A., & Fromang, S. 2013, *A&A*, 554, A17

Kataoka, A., Muto, T., Momose, M., et al. 2015, *ApJ*, 809, 78

Knebe, A., Knollmann, S. R., Muldrew, S. I., et al. 2011, *MNRAS*, 415, 2293

Kolmogorov, A. N. 1941, *Cr Acad. Sci. URSS*, 30, 301

Kong, S., Arce, H. G., Maureira, M. J., et al. 2019, *ApJ*, 874, 104

Kounkel, M., Hartmann, L., Tobin, J. J., et al. 2016, *ApJ*, 821, 8

Kroupa, P. 2000, *New A*, 4, 615

Kroupa, P., Aarseth, S., & Hurley, J. 2001, *MNRAS*, 321, 699

Kruijssen, J. M. D., Maschberger, T., Moeckel, N., et al. 2012, *MNRAS*, 419, 841

Krumholz, M. R., Crutcher, R. M., & Hull, C. L. 2013, *ApJ*, 767, L11

Krumholz, M. R., Klein, R. I., & McKee, C. F. 2012, *ApJ*, 754, 71

Krumholz, M. R., McKee, C. F., & Klein, R. I. 2004, *ApJ*, 611, 399

Krumholz, M. R., & Tan, J. C. 2007, *ApJ*, 654, 304

Kuffmeier, M., Frimann, S., Jensen, S. S., & Haugbølle, T. 2018, *MNRAS*, 475, 2642

Kuffmeier, M., Haugbølle, T., & Nordlund, Å. 2017, *ApJ*, 846, 7

Kuznetsova, A. 2018, BHL: Model using the BHL accretion prescription, doi:10.5281/zenodo.1404871

Kuznetsova, A., Hartmann, L., & Ballesteros-Paredes, J. 2015, *ApJ*, 815, 27

—. 2018, *MNRAS*, 473, 2372

Kuznetsova, A., Hartmann, L., & Burkert, A. 2017, *ApJ*, 836, 190

Kuznetsova, A., Hartmann, L., & Heitsch, F. 2019, *ApJ*, 876, 33

Kuznetsova, A., Hartmann, L., & Heitsch, F. 2020, arXiv e-prints, arXiv:2003.13697

Kuznetsova, A., Hartmann, L., Heitsch, F., & Ballesteros-Paredes, J. 2018, *ApJ*, 868, 50

Lada, C. J., & Lada, E. A. 2003, *ARA&A*, 41, 57

Lada, C. J., Lombardi, M., & Alves, J. F. 2010, *ApJ*, 724, 687

Lada, C. J., Margulis, M., & Dearborn, D. 1984, *ApJ*, 285, 141

Larson, R. B. 1969, *MNRAS*, 145, 271

—. 1981, *MNRAS*, 194, 809

—. 1995, *MNRAS*, 272, 213

Lee, Y.-N., & Hennebelle, P. 2018, *A&A*, 611, A89

Lesur, G., Hennebelle, P., & Fromang, S. 2015, *A&A*, 582, L9

LeVeque, R. J. 1992, Numerical methods for conservation laws, Vol. 3 (Springer)

Li, Z.-Y., Krasnopolsky, R., & Shang, H. 2013, *ApJ*, 774, 82

Mac Low, M.-M. 1999, *ApJ*, 524, 169

Mac Low, M.-M., & Klessen, R. S. 2004, *Rev. Mod. Phys.*, 76, 125

Mairs, S., Johnstone, D., Kirk, H., et al. 2016, *MNRAS*, 461, 4022

Maschberger, T., Bonnell, I. A., Clarke, C. J., & Moraux, E. 2014, *MNRAS*, 439, 234

Mathieu, R. D. 1983, *ApJ*, 267, L97

McCrady, N., & Graham, J. R. 2007, *ApJ*, 663, 844

McKee, C. F., & Ostriker, E. C. 2007, *ARA&A*, 45, 565

McKee, C. F., & Tan, J. C. 2003, *ApJ*, 585, 850

Mellon, R. R., & Li, Z.-Y. 2008, *ApJ*, 681, 1356

Ménard, F., & Duchêne, G. 2004, *A&A*, 425, 973

Menon, H., Wesolowski, L., Zheng, G., et al. 2015, *Computational Astrophysics and Cosmology*, 2, 1

Mestel, L., & Spitzer Jr, L. 1956, *MNRAS*, 116, 503

Moeckel, N., Holland, C., Clarke, C. J., & Bonnell, I. A. 2012, *MNRAS*, 425, 450

Mouschovias, T. C., & Psaltis, D. 1995, *ApJ*, 444, L105

Mouschovias, T. C., & Spitzer, L., J. 1976, *ApJ*, 210, 326

Myers, A. T., Klein, R. I., Krumholz, M. R., & McKee, C. F. 2014, *MNRAS*, 439, 3420

Myers, P. C. 2009, *ApJ*, 700, 1609

Nakano, T., & Nakamura, T. 1978, *PASJ*, 30, 671

Ng, C., & Bhattacharjee, A. 1997, *Physics of Plasmas*, 4, 605

Offner, S. S., Klein, R. I., & McKee, C. F. 2008, *ApJ*, 686, 1174

Offner, S. S. R., Clark, P. C., Hennebelle, P., et al. 2014, Protostars and Planets VI, 53

Ohashi, N., Saigo, K., Aso, Y., et al. 2014, *ApJ*, 796, 131

Padoan, P., & Nordlund, Å. 2002, *ApJ*, 576, 870

Palmeirim, P., André, P., Kirk, J., et al. 2013, *A&A*, 550, A38

Parker, R. J., Dale, J. E., & Ercolano, B. 2015, *MNRAS*, 446, 4278

Parker, R. J., & Meyer, M. R. 2012, *MNRAS*, 427, 637

Parker, R. J., Wright, N. J., Goodwin, S. P., & Meyer, M. R. 2014, *MNRAS*, 438, 620

Peretto, N., Fuller, G. A., André, P., et al. 2014, *A&A*, 561, A83

Pinilla, P., Birnstiel, T., Ricci, L., et al. 2012, *A&A*, 538, A114

Planck Collaboration, Ade, P. A. R., Aghanim, N., et al. 2016, *A&A*, 586, A138

Price, D. J., & Bate, M. R. 2008, *MNRAS*, 385, 1820

Price, D. J., Wurster, J., Tricco, T. S., et al. 2018, *PASA*, 35

Proszkow, E.-M., Adams, F. C., Hartmann, L. W., & Tobin, J. J. 2009, *ApJ*, 697, 1020

Rosolowsky, E. 2005, *PASP*, 117, 1403

Santos-Lima, R., de Gouveia Dal Pino, E., & Lazarian, A. 2013, *MNRAS*, 429, 3371

Scally, A., & Clarke, C. 2002, *MNRAS*, 334, 156

Scally, A., Clarke, C., & McCaughrean, M. J. 2005, *MNRAS*, 358, 742

Seifried, D., Banerjee, R., Pudritz, R. E., & Klessen, R. S. 2012, *MNRAS*, 423, L40

Seifried, D., Walch, S., Haid, S., Girichidis, P., & Naab, T. 2018, *ApJ*, 855, 81

Shu, F. H. 1977, *ApJ*, 214, 488

Smith, R. J., Glover, S. C. O., Bonnell, I. A., Clark, P. C., & Klessen, R. S. 2011, *MNRAS*, 411, 1354

Solomon, P., Rivolo, A., Barrett, J., & Yahil, A. 1987, *ApJ*, 319, 730

Springel, V. 2005, *MNRAS*, 364, 1105

—. 2010, *Proceedings of the International Astronomical Union*, 6, 203

Stephens, I. W., Dunham, M. M., Myers, P. C., et al. 2017, *ApJ*, 846, 16

Sterzik, M. F., Durisen, R. H., & Zinnecker, H. 2003, *A&A*, 411, 91

Stone, J. M., Gardiner, T. A., Teuben, P., Hawley, J. F., & Simon, J. B. 2008, *ApJS*, 178, 137

Stone, J. M., Ostriker, E. C., & Gammie, C. F. 1998, *ApJ*, 508, L99

Tan, J. C., Krumholz, M. R., & McKee, C. F. 2006, *ApJ*, 641, L121

Teixeira, P. S., Lada, C. J., Young, E. T., et al. 2006, *ApJ*, 636, L45

Terebey, S., Shu, F. H., & Cassen, P. 1984, *ApJ*, 286, 529

Tobin, J. J., Hartmann, L., Chiang, H.-F., et al. 2012, *Nature*, 492, 83

Tobin, J. J., Hartmann, L., Fűrész, G., Hsu, W.-H., & Mateo, M. 2015, *AJ*, 149, 119

Tobin, J. J., Hartmann, L., Furesz, G., Mateo, M., & Megeath, S. T. 2009, *ApJ*, 697, 1103

Truelove, J. K., Klein, R. I., McKee, C. F., et al. 1997, *ApJ*, 489, L179

Turner, N. J., Fromang, S., Gammie, C., et al. 2014, Protostars and Planets VI, 411

Vaytet, N., Commerçon, B., Masson, J., González, M., & Chabrier, G. 2018, *A&A*, 615, A5

Vázquez-Semadeni, E., Palau, A., Ballesteros-Paredes, J., Gómez, G. C., & Zamora-Avilés, M. 2019, *MNRAS*, 490, 3061

Walch, S., & Naab, T. 2015, *MNRAS*, 451, 2757

Wei, L. H., Keto, E., & Ho, L. C. 2012, *ApJ*, 750, 136

Williams, J. P., & McKee, C. F. 1997, *ApJ*, 476, 166

Wilson, C. D., Scoville, N., Madden, S. C., & Charmandaris, V. 2003, *ApJ*, 599, 1049

Wiseman, J. J., & Ho, P. T. P. 1998, *ApJ*, 502, 676

Wurster, J., Bate, M. R., & Price, D. J. 2018, *MNRAS*, 480, 4434

—. 2019, *MNRAS*, 489, 1719

Yang, H., Li, Z.-Y., Looney, L., & Stephens, I. 2016, *MNRAS*, 456, 2794

Zhang, Q., & Fall, S. M. 1999, *ApJ*, 527, L81

Zhang, S., Hartmann, L., Zamora-Avilés, M., & Kuznetsova, A. 2018, *MNRAS*, 480, 5495

Zhu, Z., Hartmann, L., & Gammie, C. 2010, *ApJ*, 713, 1143

Zhu, Z., Hartmann, L., Nelson, R. P., & Gammie, C. F. 2012, *ApJ*, 746, 110

Zhu, Z., Nelson, R. P., Dong, R., Espaillat, C., & Hartmann, L. 2012, *ApJ*, 755, 6

Zhu, Z., Nelson, R. P., Hartmann, L., Espaillat, C., & Calvet, N. 2011, *ApJ*, 729, 47

Zinnecker, H. 1982, *Annals of the New York Academy of Sciences*, 395, 226

Zuckerman, B., & Evans, N. J., I. 1974, *ApJ*, 192, L149